University of Nevada, Reno

Improvements to the Measurement of Atmospheric Reactive Mercury, and Contributions to the Investigation of Reactive Mercury at Six Sampling Sites

A thesis submitted in partial fulfillment
of the requirements for the degree of
Master of Science in Environmental Sciences and Health

by

Natalie R. Allen

Mae S. Gustin/Thesis Advisor

May, 2023

THE GRADUATE SCHOOL

We recommend that the thesis
prepared under our supervision by

NATALIE R. ALLEN

entitled

Improvements to the Measurement of Atmospheric Reactive Mercury, and Contributions to the Investigation of Reactive Mercury at Six Sampling Sites

be accepted in partial fulfillment of the
requirements for the degree of

MASTER OF SCIENCE

Mae S. Gustin, Ph.D.
Advisor

Sarrah Dunham-Cheatham, Ph.D.
Committee Member

Patrick Arnott, Ph.D.
Graduate School Representative

Markus Kemmelmeier, Ph.D., Dean
Graduate School

May, 2023

Abstract

Mercury (Hg) is a globally transported hazardous pollutant. In the atmosphere, reactive mercury (RM), composed of gaseous oxidized and particulate-bound Hg, comprises the minority of Hg fractions, but contributes significantly to wet and dry deposition. Unfortunately, the standard instrument used for the past twenty years has been shown to inaccurately measure atmospheric RM. Therefore, the University of Nevada, Reno – Reactive Mercury Active System (RMAS) was developed to improve measurements of RM concentrations, in addition to identification of the chemistry of RM compounds, which was previously impossible. The work presented in this thesis focused on investigating the impact of flow rates on RMAS RM collection and whether the RMAS cartridge that holds membranes collected RM. In addition, alternate surfaces for RM collection were tested. The results of this work are presented in Chapter 2. Chapter 3 summarizes contributions made to a multi-year field campaign aimed at collecting RM using the RMAS at: Amsterdam Island, Indian Ocean; Atlanta, GA; the Great Salt Lake, UT; Guadalupe Mountains National Park, TX; and Reno, NV and the adjacent Peavine Peak. Chapter 3 was focused on understanding the chemistry and concentrations of RM at locations with different ambient air chemistry. Lastly, in Chapter 4, the thesis work was summarized, and the direction of future work discussed.

Acknowledgments

This work was funded by NSF Grant 2043042 from the Atmospheric Chemistry Program. I would like to thank my primary mentors throughout the course of this project, Dr. Mae Gustin and Dr. Sarrah M. Dunham-Cheatham, University of Nevada, Reno (UNR), who were always there to answer questions and dedicated their time to the development of this project and my personal, professional development; their inputs have greatly improved this work and their advice has led to immense academic growth. I also thank collaborators: Dr. Patrick Arnott, University of Nevada, Reno, for serving as a thesis committee member, Dr. Seth Lyman, Utah State University, for project assistance; Jordin Jacobs, UNR M.S. graduate, for assistance with laboratory analyses; the many co-authors and collaborators listed and not listed here; and UNR graduate and undergraduate students: Bianca Martinez; Mitchell Aikin; Nicole Choma; Gabriela Fernandez; Chris Ford; and Morgan Yeager for help with field work, laboratory analyses, and maintenance of trace-clean glassware. I would also like to thank my parents and brother, Aiden.

Table of Contents

List of Abbreviations

Hg	Mercury
Hg(0)	Elemental mercury
Hg(II)	Oxidized mercury
$CH3Hg^{+}$ or MeHg	Methylmercury
GEM or Hg(0)	Gaseous elemental mercury
GOM or Hg(II)	Gaseous oxidized mercury
PBM	Particulate-bound mercury
RM	Reactive mercury
University of Nevada, Reno	UNR
Reactive Mercury Active System	RMAS
National Atmospheric Deposition Network	NADP
Tekran 1130/1135/2537 system	Tekran
Potassium chloride	KCl
Cold vapor atomic fluorescence spectrometry	CVAFS
Reno Atmospheric Mercury Intercomparison Experiment	RAMIX
Cation exchange membranes	CEM
Polytetrafluoroethylene membranes	PTFE
Dual-channel system	DCS
Total gaseous mercury	TGM
Polyethersulfone	PES

Chapter 1 - Introduction

Overview of Mercury

Mercury (Hg) is unique because it is the only metallic element that is liquid at room temperature. Hg is non-essential for all living things and can cause deleterious health effects, but has been used as a product, predominately in medicine, and for mining since ancient times (Wujastyk, 2015). For example, until the development of penicillin to treat syphilis, a Hg salt, specifically calomel or mercurous chloride (Hg_2Cl_2), was used to treat the disease (O'Shea, 1990). Over time, humans have become more aware of Hg health concerns and have limited its direct use. Today, Hg can be found in batteries, fluorescent lightbulbs, dental amalgams, imported skin-lightening cosmetics, and as a pharmaceutical preservative (i.e., vaccines) (U.S. EPA, 2023). Although many countries have worked to reduce Hg use and release over the past few decades, anthropogenic Hg emissions rose 20% from 2010 to 2015; predominately in developing nations. In 2015, the highest Hg emissions were generated by Asian, South American, and Sub-Saharan African countries due to coal combustion and/or artisanal and small-scale gold mining (UNEP, 2019). The control of anthropogenic Hg releases in the environment remains a major concern, because the pollutant has a long environmental lifespan, and is globally transported.

The Minamata Convention, an environmental treaty established with the goal of controlling the Hg supply and trade, and to reduce the use, emission, and release of Hg to the environment, was adopted by the United Nations in 2013, and has been in effect since 2017 with, as of today, 140, legally bound parties. Ratification of the Minamata

Convention tasks nations with recognizing the risks of Hg, and eliminating or reducing all anthropogenic inputs of Hg to the Earth system (UNEP, 2019).

The Health Effects of Mercury

Hg naturally exists in three chemical forms: 1) elemental Hg (Hg(0)); 2) inorganic Hg; and 3) organic Hg. Human exposure to Hg(0) can occur via inhalation and once inhaled, Hg(0) easily crosses the blood-brain barrier and can be oxidized to Hg(II), also known as oxidized Hg, and retained by brain cells for years (Bjørklund et al., 2017). Hg(0) exposure can occur through dental amalgams (Park and Zheng, 2012). Short-term, high Hg(0) exposure, is less common than chronic exposure, but may cause cough, chills, fever, and potential development into lung injury and kidney failure (Kao and Rusyniak, 2020). Inorganic Hg salts accumulate in the liver and kidneys, and humans may be exposed by dermal absorption (Langford and Ferner, 1999). Chronic exposure to inorganic Hg can manifest as tremors, mouth and gum infections, and neurological changes (i.e., fatigue, insomnia, depression) as Hg is a neurotoxin (Kao and Rusyniak, 2020).

One of the most common human exposures to Hg is organic Hg, as methylmercury ($CH3Hg^{+}$ or MeHg), through seafood and rice consumption (Ravichandran, 2004). In ecosystems, MeHg is bioaccumulated and biomagnified, because organic Hg binds to thiol functional groups in proteins (Ravichandran, 2004). If MeHg is consumed, MeHg-thiol complexes are formed and readily transported throughout an organism and across cell membranes as a mimicked amino acid (i.e., cysteine mimicking methionine) before being deposited in the body, within about three days (Clarkson et al., 2007). Absorption of MeHg by human blood was estimated to be

approximately 90% and the half-life of MeHg in the body, between one to two months (Wexler, 2014).

A notorious case of MeHg poisoning occurred in Minamata, Japan, in 1956 when a chemical company adjacent to Minamata Bay disposed of acetaldehyde waste containing MeHg into the bay. Over time, the MeHg bioaccumulated and biomagnified, and became concentrated in the bay's fish and the people of Minamata, who regularly consumed the fish, were severely poisoned. Characteristic symptoms of Minamata disease are a result of damage to the central nervous system and include spastic movement of the body, difficulty speaking and hearing, and altered vision; more mild symptoms can include body aches, tingling sensations, and decreased memory (Yorifuji and Tsuda, 2014; Hachiya, 2006).

Hg exposure in animals has been associated with damage to the nervous, excretory, and reproductive systems (Wolfe et al., 1998). Hg health effects in other terrestrial biota includes inhibiting the activity of soil microbes and plant growth, possibly through Hg inducing oxidative stress (Mahbub et al., 2017).

Mercury Sources and Biogeochemical Cycle

Hg is found concentrated in cinnabar mineral deposits, composed of Hg sulfide (HgS), primarily found in mercuriferous belts that are located along tectonic plate boundaries in western North America, central Europe, and southern China (Selin, 2009). Natural sources of Hg include volatilization from soils and rock that are enriched in Hg due to hydrothermal activity, inactive and active volcanoes, geothermal sources (i.e., hot springs), and erosion (Selin, 2009). The Outridge et al. (2018) reported that anthropogenic activities have increased natural atmospheric concentrations of Hg by

450%, and in 2015, anthropogenic emissions were primarily from artisanal and small-scale gold mining (38%), fossil fuel and biomass burning (24%), cement production (11%), and ferrous metal production (2%) (UNEP, 2019). The global mercury budget in 2015 is shown in Figure 1.

In general, the Hg biogeochemical cycle describes natural and anthropogenic emissions of Hg to the atmosphere, where Hg can be globally transported, oxidized, and deposited to land or water surfaces. The surface exchange of Hg contributes to its environmental persistence, because once deposited to a surface, Hg is readily re-emitted, and less Hg ends up entering the aquatic food chain, or becomes stored in the aquatic or land pools (UNEP, 2019).

More specifically, atmospheric Hg primarily enters aquatic systems via wet or dry deposition as Hg(II) (Selin, 2009). Deposition rates of Hg are dependent on its chemical form, as discussed in Section 1.4. The atmosphere and aquatic Hg pools are in constant exchange of Hg at the surface, Hg(II) is deposited, and will commonly, immediately re-volatilize to the atmosphere as Hg(0), which has been estimated to be up to 70% in the ocean system (Mason et al., 2012). The rate of Hg(0) evasion or deposition, from any surface, is dependent on local weather conditions (i.e., high precipitation, solar radiation, etc.) (Mason et al., 2017). The dominant source of Hg to the ocean is not definitively understood, and based on recent measurements is dependent on location; for example, the largest Hg sources to oceans have been estimated to be atmospheric deposition to open ocean waters, and riverine sources for coastal waters (Liu et al., 2021). Generally, Hg in the ocean is not uniformly distributed and concentrations are elevated in ocean surface waters (100 m depth), where gas exchange and mixing occur (Mason et al., 2012). The

lifespan of Hg in near-surface waters has been estimated to be ~1 year, which increases with ocean depth, and MeHg in the ocean ~10 years (Mason et al., 2012). Hg is important within the aquatic pool because microbes may convert Hg to MeHg which can bioaccumulate and -magnify up the aquatic food chain, threatening human health.

When Hg(0) deposits to land, Hg may volatilize back to the atmosphere due to its high vapor pressure (for a metal) or become incorporated in the soil Hg pool (Gworek et al., 2020; Selin, 2009). Plants can uptake gaseous Hg via their stomata, with vegetation uptake accounting for 60 to 90% of atmospheric Hg deposition (Zhou et al., 2021). Plant Hg reaches the terrestrial pool predominately via litterfall, but also by throughfall and/or plant die-off (Zhou et al., 2021; Gworek et al., 2020). The final sink of Hg is incorporation into aquatic bottom-sediments and sub-surface soils, which can take centuries or longer (UNEP, 2019).

Atmospheric Mercury

Hg in the atmosphere exists in 3 forms: 1) gaseous elemental mercury (GEM); 2) gaseous oxidized mercury (GOM); and 3) particulate-bound mercury (PBM). Together, GOM and PBM are defined as reactive mercury (RM = GOM + PBM), because the two fractions are difficult to differentiate between for measurements. Atmospheric oxidized Hg exhibits gas to particle phase partitioning that is dependent on temperature, this behavior is not completely understood, but under warmer conditions, less particles persist (Amos et al., 2012). RM is more reactive, water-soluble, readily deposited, and hazardous than GEM. RM may be deposited on a local or regional scale, while GEM is transported on a global scale due to its longer atmospheric lifespan (Lyman et al., 2020a). The

atmospheric lifespan of RM is on the scale of days versus up to one-to-two years for GEM (Lyman et al., 2020a).

Gaseous Elemental Mercury

GEM is the dominant form of atmospheric Hg, and background concentrations range from ~ 1 to 2 ng m^{-3} (Sprovieri et al., 2016). GEM concentrations have been observed to decrease with altitude; slightly lower GEM concentrations were observed in the free troposphere during an aircraft measurement campaign in Europe in 2013, where concentrations in the boundary layer ranged from 1.4 and 1.6 ng m^{-3} and decreased to 1.3 ng m^{-3} in the free troposphere (Weigelt et al., 2016). In the stratosphere, GEM concentrations are lower than in the troposphere; hundreds of transcontinental flight measurements of stratospheric GEM from 2005 to 2007 ranged from 0.25 to 0.7 ng m^{-3} (Slemr et al., 2009). In general, atmospheric GEM concentrations are higher in the Northern Hemisphere (~1.5 ng m^{-3}) compared to the Southern Hemisphere (~1 ng m^{-3}), and in an urban versus rural setting, because there are more Hg emissions sources (i.e., industrial activity) (Lyman et al., 2020a; Sprovieri et al., 2016).

Particulate-Bound Mercury

In general, fine PBM (< 2.5 μm in diameter) is formed by Hg(II) sorption onto combustion products and other aerosol types. Coarse PBM (> 2.5 μm) forms by sorption of Hg(II) onto naturally generated particles (i.e., salt spray, dust) and in response to mechanical processes generated by anthropogenic sources (Lyman et al., 2020a). A summary of historical fine PBM measurements revealed that in the Northern Hemisphere (~110 pg m^{-3} (mean)), PBM concentrations are higher than in the Southern Hemisphere (~50 pg m^{-3}) (Zhang et al., 2019), which is due to the greater amount of Hg emissions in

the Northern Hemisphere. The same is true for PBM in urban settings, PBM concentrations are higher (~225 pg m^{-3}) than in rural settings (~25 pg m^{-3}), due to increased Hg emissions present in the urban environment (Zhang et al., 2019). All PBM concentrations must be interpreted with caution, because the relationship between PBM and GOM in the atmosphere is not well understood and the gold standard instrument used for many measurements does not accurately measure PBM.

Gaseous Oxidized Mercury

GOM is primarily in the +II oxidation state. Oxidized Hg also exists as Hg(I), but Hg(I) is assumed to be unstable and will rapidly either convert back to Hg(0) or be further oxidized to Hg(II) (Lyman et al., 2020a). GOM is either emitted directly from anthropogenic point sources or is converted from GEM to GOM by atmospheric oxidants in the troposphere (Gustin et al., 2021a). Since the ability to measure ambient GOM is limited by current instrumentation (discussed below), historical concentrations of GOM are unreliable. More recently, reliable measurement methods report GOM concentrations on the scale of 10 to 100s of pg m^{-3}, depending on the time of year and location (Chapter 3; Luippold et al., 2020a). During the spring and summer, GOM concentrations increase due to increases in ambient temperature and sunlight, ideal conditions to produce atmospheric oxidants that convert GEM to GOM; the opposite occurs during the fall and winter (Luippold et al., 2020a). Concentrations of GOM may be higher in urban environments (i.e., higher anthropogenic Hg emissions); for example, measured concentrations of GOM in Chinese cities report concentrations of hundreds of pg GOM m^{-3} (Bu et al., 2018; Fu et al., 2015).

Atmospheric oxidation of GEM occurs by halogenated compounds (e.g., bromine (Br) and chlorine (Cl)) and other oxidants (e.g., hydrogen peroxide (H_2O_2), ozone (O_3), hydroxyl radical ($OH^{\cdot}$), and nitrate radical ($NO3^{\cdot}$)) (Lyman et al., 2020a; Si and Ariya, 2018). The actual reactions and resulting RM chemistry is uncertain due to unknown kinetics, discrepancies between models and field observations, and an inability to readily determine the chemical identity of GOM (Castro et al., 2022; Gustin et al., 2020; Lyman et al., 2020a; Saiz-Lopez et al., 2020). The atmospheric reduction-oxidation chemistry of Hg is almost exclusively understood through computational studies. In general, it is thought that Br converts Hg(0) to Hg(I) and then an ambient oxidant, primarily O_3 due to its abundance, converts Hg(I) to Hg(II) (Castro et al., 2022; Shah et al., 2021). A recent study suggested that $OH^{\cdot}$ and O_3 together (step-wise) can covert Hg(0) to Hg(II) (Castro et al., 2022). Unique oxidation reactions occur in atmospheric water droplets, and may involve O_3, $OH^{\cdot}$, and halogens (Si and Ariya, 2018). Atmospheric surface reduction of Hg(II) to Hg(0) has been show to occur through heterogeneous surface reactions using fly ash, as well as iron and sodium chloride aerosols (Si and Ariya, 2018).

The chemical properties of a GOM compound depend on the bound ligand; therefore, it is important to understand GOM chemistry (Lin et al., 2006). The University of Nevada, Reno - Reactive Mercury Active System (UNR - RMAS) qualitatively identifies RM compounds in ambient air; specifically, nylon membranes are thermally desorbed to determine the potential chemistry of RM or GOM compounds when compared to thermal desorption profiles of pure, standard GOM compounds (Luippold et al., 2020b; Huang et al., 2013). The GOM compounds used for the thermal desorption profiles included gaseous: Hg(II) bromide ($HgBr_2$); Hg(II) chloride ($HgCl_2$); Hg(II) oxide

(HgO); Hg(II) nitrate ($Hg(NO_3)_2$); Hg(II) sulfate ($HgSO_4$); and liquid MeHg added directly to the membrane (Dunham-Cheatham et al., 2023; Huang et al., 2013). Figure 2 shows the standard thermal desorption profiles of each Hg compound. Studies using the RMAS have shown that the nylon membrane thermal desorption data compares well to ambient chemistry measurements (Gustin et al., 2021b; Luippold et al., 2020a).

The thermal desorption method was initially developed by Huang et al. (2013), and improved by Luippold et al. (2020a), in which the temperature ramp and pyrolyzer temperature was optimized, and by Dunham-Cheatham et al. (2023), where model fit values were made possible and the thermal desorption ranges were refined to better allow for individual identification of RM compounds. An important question that needs to be resolved is whether the chemistry of RM compounds remains the same or changes upon sorption to the nylon membrane surface (Lyman et al. 2020a). Recent laboratory work has shown that GOM sorbed to a membrane surface, like the ones used by the RMAS, was subject to exchange interactions with co-adsorbed GOM and other chemical compounds (Mao and Khalizov et al., 2021). However, it is still unclear how the membranes behave under field conditions as these laboratory results were derived using RM concentrations five orders of magnitude higher than those typically observed in ambient air.

Atmospheric Mercury Monitoring

In 2016, there were twenty-two global, national, and regional networks monitoring Hg in ambient air and in wet deposition (UNEP et al., 2016; Tørseth et al., 2012). Other noteworthy networks include the: Euorpean Monitoring and Evaluation Programme, the oldest network, beginning in 1980; Global Mercury Observation System

(GMOS), with about 30 active monitoring sites dispersed in the Northern and Southern Hemispheres; National Institute for Minamata Disease and the National Institute for Environmental Studies in Japan, with, 281 monitoring sites; and National Atmospheric Deposition Program (NADP) in the United States, with a Hg-specific Mercury Deposition Network that maintains 84 active sites that measure Hg in wet deposition in the United States and Canada (GMOS, 2023; NADP, 2023b; UNEP et al., 2016). All active monitoring locations in 2016 are shown in Figure 3. In 2021, Hg monitoring in litterfall, an important input of Hg to forests, was added to the NADP, with 24 sites in the United States (NADP, 2023a). Unfortunately, the distribution of current global atmospheric Hg monitoring stations is inadequate at generating sufficient data to accurately model the global Hg biogeochemical cycle, especially in southern Asia, Africa, South America, Russia, and Australia (Lyman et al., 2020a; UNEP, 2019; UNEP et al., 2016).

Globally, atmospheric Hg is being monitored, but the measurements are not representative of current atmospheric Hg concentrations as there is not a deployable, accurate, or field calibrated method to measure ambient atmospheric Hg. The gold standard instrument used for global monitoring, the Tekran 1130/1135/2537 system (Tekran), suffers from bias under various ambient sampling conditions that are discussed below (Gustin et al., 2021a).

Tekran 1130/1135/2537 System

The Tekran, introduced in 2002, was thought to measure ambient GOM, PBM, and GEM, respectively, over thirty-minute to three-hour periods; the system is shown in Figure 4 (Tekran Instruments Corporation, 2022; Landis et al., 2002). The operation of

the Tekran is as follows: air is pulled by vacuum pump from ambient air (9 L min^{-1}), and atmospheric particles greater than 2.5 μm in diameter are removed via a heated elutriator (50 °C) at the inlet of the 1130 module. The ambient air sample then moves through a potassium chloride (KCl) coated quartz annular denuder designed to collect GOM, followed by a quartz fiber filter contained in the 1135 module for collecting PBM. As GOM and PBM are collected by the denuder or filter, respectively, the air passing through only contains GEM that is quantified downstream by cold vapor atomic fluorescence spectrometry (CVAFS) in the 2537 module. Following the collection period during which GEM is being measured, GOM and PBM are sequentially removed from the denuder and filter by heating the collection surfaces to 500 °C and 800 °C, respectively, by an oven that surrounds each collection surface. Then, the released oxidized Hg is converted to GEM by a pyrolyzer that heats the sample air to 800 °C. The released GEM is sequentially transported 10 m by a stream of heated (50 °C) Hg-free zero air through a soda lime trap (i.e., to prolong the life of the gold traps by eliminating any present free halogens, water vapor, acid, or volatile organic compounds) and into the 2537 module, where the GEM is collected onto one of two gold-coated sand traps. The collected GEM is desorbed, at 350 °C, every 5 minutes, alternating between the two gold-coated sand traps. Once desorbed from the traps, the GEM is carried by argon to a quartz cell where the GEM is quantified using CVAFS (Tekran Instruments Corporation, 2022; Gustin et al., 2015). Typically, the Tekran is calibrated every twenty-four hours using an internal GEM permeation source, and less frequently by manual injections of GEM (Landis et al., 2002).

In the late 2000s, use of a novel method to measure GOM in dry deposition demonstrated that deposition measurements were significantly higher than those determined using a simultaneously operating Tekran (Lyman et al., 2009, 2007). Another study in Florida found different atmospheric GOM spatial and temporal patterns using passive and dry deposition samplers relative to the Tekran. The different GOM patterns were speculated to be because of the presence of varying ambient GOM compounds or chemistry that influenced collection by either the passive and dry deposition samplers or the Tekran (Peterson et al., 2012; Sexauer Gustin et al., 2012). These studies revealed the potential for the Tekran measurements to have a low bias. As a result, a National Science Foundation proposal was awarded to support the Reno Atmospheric Mercury Intercomparison eXperiment (RAMIX) study that compared multiple instruments, that measure atmospheric Hg in ambient air, at the same location in 2012. The RAMIX study further showed that Tekran RM measurements could be up to 13 times lower than the University of Washington Detector for Oxidized Hg Species (Gustin et al., 2013). The RAMIX project and further studies also demonstrated that GOM accumulated on the Tekran PBM module, GOM sorbed to the Tekran walls during temperature drops in the sample line, and sampling efficiency by the KCl-denuder decreased as ambient relative humidity and O_3 increased, further supporting that the industry standard instrument was an inadequate and inaccurate method for RM measurements (Gustin et al., 2015). The continued use of the Tekran stems from the lack of a readily available and standard method to calibrate atmospheric RM measurements (Lyman et al., 2020b).

The University of Nevada, Reno - Reactive Mercury Active System

Due to the above concerns associated with the Tekran measurements, the RMAS was developed by Dr. Mae Gustin's group at UNR. The RMAS was first discussed and implemented in Huang et al. (2013), and further improved by Luippold et al. (2020b). Major RMAS improvements included: a switch from a plastic to metal weather shield; use of two pumps for three sample lines instead of one pump for one sample line; a switch from glass to plastic tubes for membrane storage; use of multi-staged membrane cartridges rather than multiple single-stage membrane cartridges; improved temporal resolution of measurements by increasing the flow rate was achieved; and flow control was changed from the pumps alone to also include critical flow orifices. Presently, the RMAS has been deployed globally in locations that represent different meteorological and air chemistry conditions (i.e., Nevada; Florida; Maryland; Mauna Loa, Hawaii; Australia; Arctic Circle; Texas; Great Salt Lake, Utah; Georgia; Amsterdam Island (Gustin et al., in progress, 2021b; Miller et al., 2021; Osterwalder et al., 2021; Luippold et al., 2020a; Sexauer Gustin et al., 2016)).

Hardware

The RMAS consists of an anodized aluminum weather shield housing six sample lines, mounted approximately one m from the ground. The six sample lines of the RMAS each hold a perfluoroalkoxy alkane dual- or three-staged membrane cartridge (Savillex; 98 mm length) containing two or three membranes, each 5 mm apart. The membrane cartridges are connected by polyethylene tubing (Bev-a-line; 6.35 mm diameter) to vacuum pumps (Welch, 2534B-01) that are stored inside or in boxes. Ambient air flow through each sample line is controlled by a critical flow orifice at 1 or 2 L min^{-1}

(Teledyne API, 941100 and 941700, respectively) for one- or two-week sampling deployments. A schematic of the RMAS is shown in Figure 5.

Reactive Mercury Collection Surfaces

Membranes have been identified as a material that can capture and retain atmospheric RM and have been used as a collection surface for RM since the late-1990s (Sheu and Mason et al., 2001; Ebinghaus et al., 1999). Membranes are cation exchange membrane that retain Hg(II) compounds However, membranes have limitations and have not been calibrated.

Membranes historically used in the RMAS to measure RM or GOM and PBM include cation exchange membranes (CEM; Pall Corporation, S80570; 0.8 μm (pore size)) and polytetrafluoroethylene membranes (PTFE; Sartorius Stedium Biotech, 1180747N; 0.2 μm), respectively. The CEM membrane is a polyethersulfone material that is proprietarily treated to preferentially sorb cations. Nylon membranes (Sartorius Stedium Biotech, 2500747N; 0.2 μm) have been used for RM chemistry identification, as the membrane does not melt or passivate the Tekran 2537 gold traps, as does the CEM during thermal desorption (Dunham-Cheatham et al., 2020). The CEM has been shown to only collect RM, not GEM (Miller et al., 2019), but has been associated with a positive humidity interaction (Huang and Gustin, 2015). The PTFE membrane can be assumed to collect some GOM under ambient conditions due to GOM interactions with aerosols (Gustin et al., 2015; Rutter and Schauer, 2007). The nylon membrane has been associated with negative ambient humidity and ozone interactions (Huang and Gustin, 2015), and has been observed to have decreased collection efficiency for RM nitrogen compounds (Luippold et al., 2020a).

Within each RMAS membrane cartridge, two nylon or CEM membranes are deployed. The membrane closest to the sampling inlet is the upstream membrane, and the subsequent membrane is the downstream membrane; the downstream membrane is used to calculate breakthrough of Hg from the upstream membrane. A third membrane can be placed upstream of the two membranes to measure PBM (> 0.2 μm); in this configuration the two downstream membranes then measure GOM. Total Hg concentrations are determined on all CEM, PTFE, and downstream nylon membranes by EPA method 1631 Revision E (U.S. EPA, 2002), and upstream nylon membranes are analyzed by thermal desorption (Dunham-Cheatham et al., 2023).

The objectives of the work described in Chapter 2 of this thesis were to perform the following experiments involving the RMAS: 1) application of increasing the RMAS sampling flow rate to determine whether the sampling duration can be decreased; 2) intercomparison of alternate commercial membranes and the historical RMAS membranes; and 3) determination of whether RM sorbs to the cartridge holding the membranes to potentially explain higher RM concentrations than measured by the RMAS, as measured by two co-located dual-channel systems in 2019 and 2020 (Dunham-Cheatham et al., 2023).

Sampling Locations

For Chapter 2, RMAS experiments were performed at the UNR College of Agriculture, Biotechnology & Natural Resources Agricultural Experiment Station Valley Road Greenhouse Complex (Greenhouse; 39.5375, −119.8047, 1367.6 meters above sea level (masl)). This sampling location was the setting for previous RMAS experiments (Dunham-Cheatham et al., 2020; Luippold et al., 2020b). The Greenhouse was impacted

by vehicle emissions, as it was located adjacent (100 m) to Interstate-80, and the long-range transport of pollutants (Gustin et al., 2021b; Luippold et al., 2020a).

For Chapter 3, the RMAS was simultaneously deployed at six sampling locations/sites (5 below + Greenhouse) across the United States. All sampling locations, except for Amsterdam Island, are plotted in Figure 6.

1. The Amsterdam Island sampling site was located on Amsterdam Island, a remote sampling location in the Indian Ocean (-37.796061, 77.551345, 67 masl). An RMAS and three Aerohead samplers, for quantification of GOM dry deposition, were deployed from December 2020 to December 2021 (Lyman et al., 2010, 2009). The intention for this site was to take measurements representing RM in the marine environment.

2. The Atlanta, GA sampling site was located at a Georgia Department of Air Quality sampling station adjacent to Interstate-85, a major fourteen-lane highway (33.778463, -84.391425, 286 masl). The air chemistry at the site was heavily influenced by mobile source emissions. In addition, the site experienced high humidity year-around, allowing for comparison with other sites that experience consistent low humidity. A RMAS and RMAS+P shield were deployed at the site beginning in October 2021 until June 2022.

3. The Great Salt Lake, UT sampling site was located just offshore of the Great Salt Lake, on Antelope Island, in Salt Lake City, Utah (41.060451, -112.238430, 1283 masl). A RMAS and RMAS+P were deployed at the site beginning in October 2021 until March 2022, before restarting again at a new sampling location (41.084985, -112.111791 masl) in September 2022 until January 2023. The high salinity content of the Great Salt

Lake (5 to 27% (Gwynn, 1996)) compared to the ocean (3.5% (U.S. Geological Survey)) makes the sampling site applicable to understanding marine atmospheric RM behavior and that of other brine lakes. In 2005, the Utah Department of Health and the Utah Division of Wildlife Resources set a Hg consumption advisory on waterfowl species that eat the salt brine shrimp in the lake (UDEQ, 2021). The source of methylated Hg to the lake has been debated as there are historical Hg deposits from mining in the region, including from an adjacent copper mine, operating from the late 1800s and into the 1960s (Wurtsbaugh et al., 2020). On the other hand, Peterson and Gustin et al. (2008) showed that atmospheric Hg deposition to the lake was high enough to cause the elevated Hg concentrations in the brine shrimp.

4. The Guadalupe Mountains, TX sampling site was located within Guadalupe Mountains National Park in Texas (31.891128 -104.805378, 1680 masl). There was one RMAS and three Aerohead samplers deployed from June 2021 to March 2022. The site was downwind of the Permian Basin, a large oil and natural gas producing region.

5. The Peavine sampling site was located at the peak of Peavine Mountain in Reno, Nevada (39.589389, -119.928797, 2513 masl). In combination with the Greenhouse site, the Peavine site acted as an adjacent high elevation representation of atmospheric RM. The site was influenced by free tropospheric air. An RMAS and RMAS+P shield were deployed from September 2022 to November 2022.

Chapter Overview

Chapter 2 of this thesis is a component of a manuscript that will be submitted for review in spring 2023. This manuscript discusses experiments performed to the RMAS.

Chapter 3 is a summary of all contributions made to the following manuscripts:

1. Observations of the chemistry and concentrations of reactive Hg at locations with different ambient air chemistry. Mae Sexauer Gustin, Natalie R. Allen, Sarrah M. Dunham-Cheatham, Nicole Choma, Seth Lyman, William Johnson, Sam Lopez, Armistead Russell, Eric Mei, Olivier Magand, Aurelien Dommergue
2. Determining sources of reactive mercury compounds in Reno, Nevada, USA. Mae Sexauer Gustin, Sarrah M. Dunham-Cheatham, Nicole Choma, Kevin Shoemaker, Natalie R. Allen

Chapter 4 provides a summary of the research questions, conclusions, and goals accomplished in this thesis, as well as recommendations and directions for future research.

Chapter 1 Figures

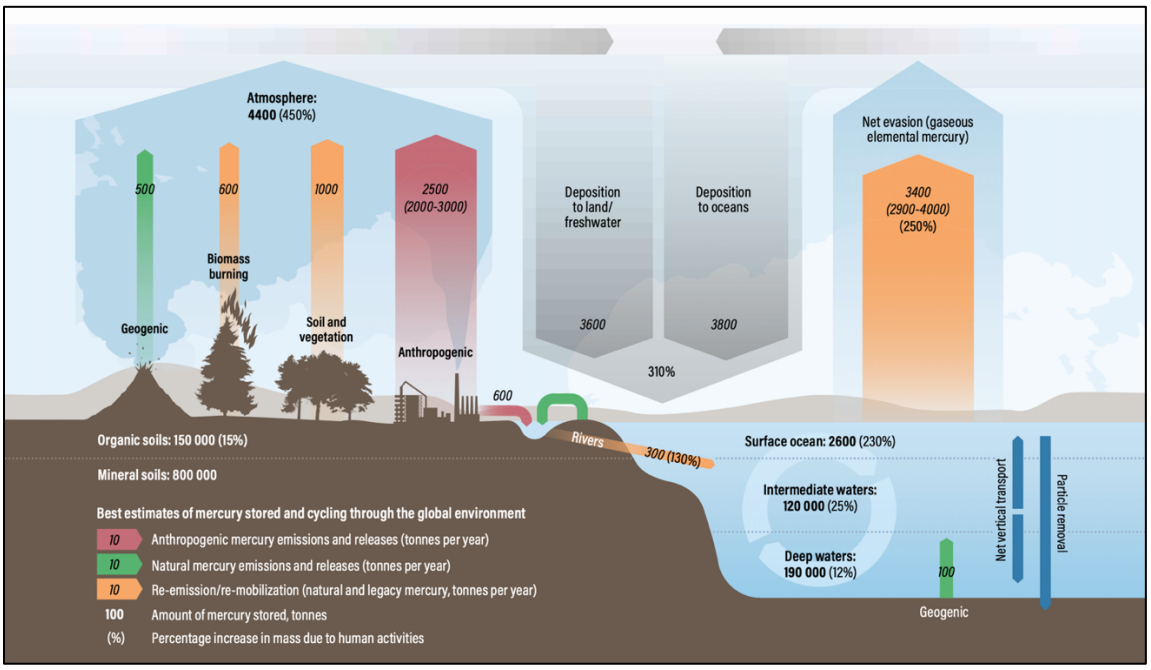

Figure 1. The global mercury budget in 2015.

Note. From "Updated Global and Oceanic Mercury Budgets for the United Nations Global Mercury Assessment 2018," by P. M. Outridge, R. P. Mason, F. Wang, S. Guerrero, & L. E. Heimbürger-Boavida, 2018, Environmental Science & Technology, 52(20), 11466 – 11477, (https://doi.org/10.1021/acs.est.8b01246). Copyright 2018 American Chemical Society. Reprinted with Permission.

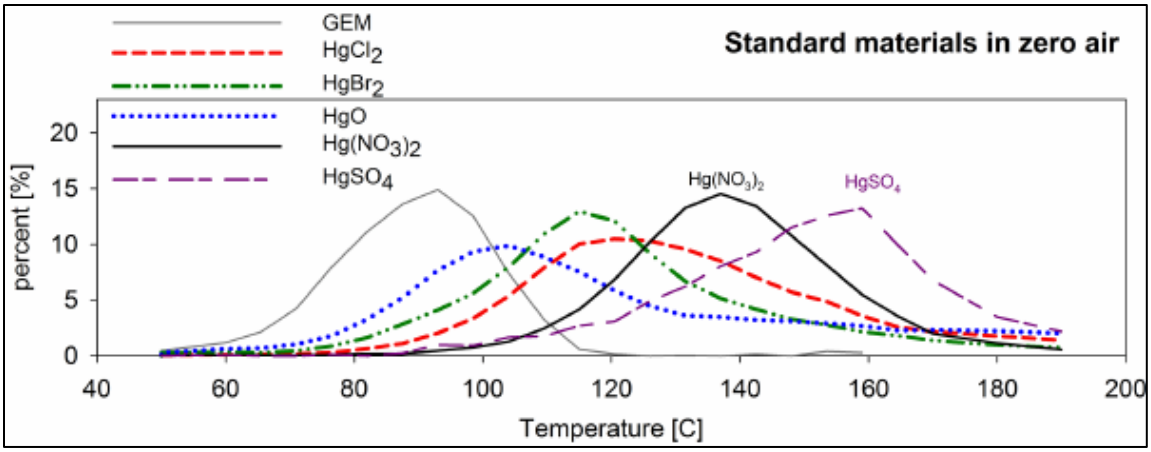

Figure 2. The thermal desorption profiles for standard oxidized mercury compounds. Methylmercury is not shown here.

Note. From "Measuring and modeling mercury in the atmosphere: a critical review," by M. S. Gustin, H. M. Amos, J. Huang, M. B. Miller, K. Heidecorn, 2015, Atmospheric Chemistry and Physics, 15(10), 5697 – 5713, (https://doi.org/10.5194/acp-15-5697-2015). CC BY 3.0. Reprinted with Permission.

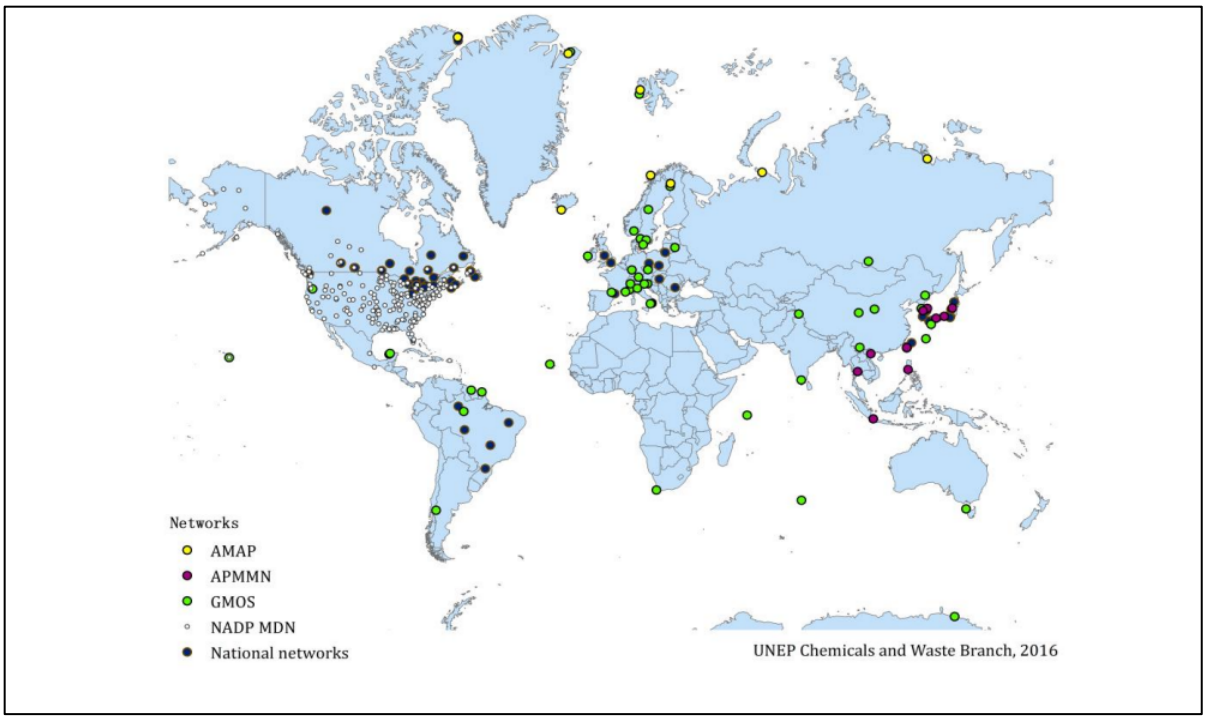

Figure 3. Locations of all atmospheric mercury monitoring sites in 2016. AMAP is the Arctic Monitoring and Assessment Programme, APMMN is the Asia-Pacific Mercury Monitoring Network, GMOS is the Global Mercury Observation System, and NADP MDN is the National Atmospheric Deposition Program Mercury Deposition Network. Note. From "Global Review of Mercury Monitoring Networks," by the United Nations Environment Programme, 2016, (https://wedocs.unep.org/20.500.11822/31268). Figure 3, page 22. Reprinted with Permission.

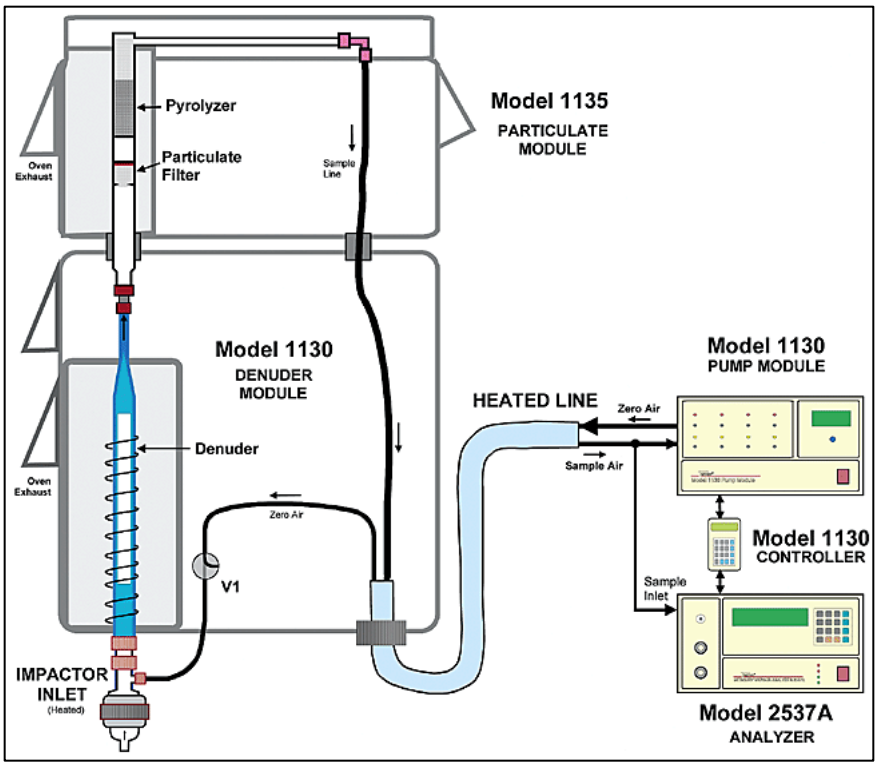

Figure 4. A diagram of the Tekran 1130/1135/2537 system for atmospheric mercury measurements. The ambient sample stream enters the 1130 module at the impactor inlet and follows the sample line to eventually enter the 2537 module for analysis.

Note. From "Development and Characterization of an Annular Denuder Methodology for the Measurement of Divalent Inorganic Reactive Gaseous Mercury in Ambient Air," by M. S. Landis, R. K. Stevens, F. Schaedlich, & E. M. Prestbo, 2002, Environmental Science & Technology, 36(13), 3000 – 3009, (https://doi.org/10.1021/es015887t).

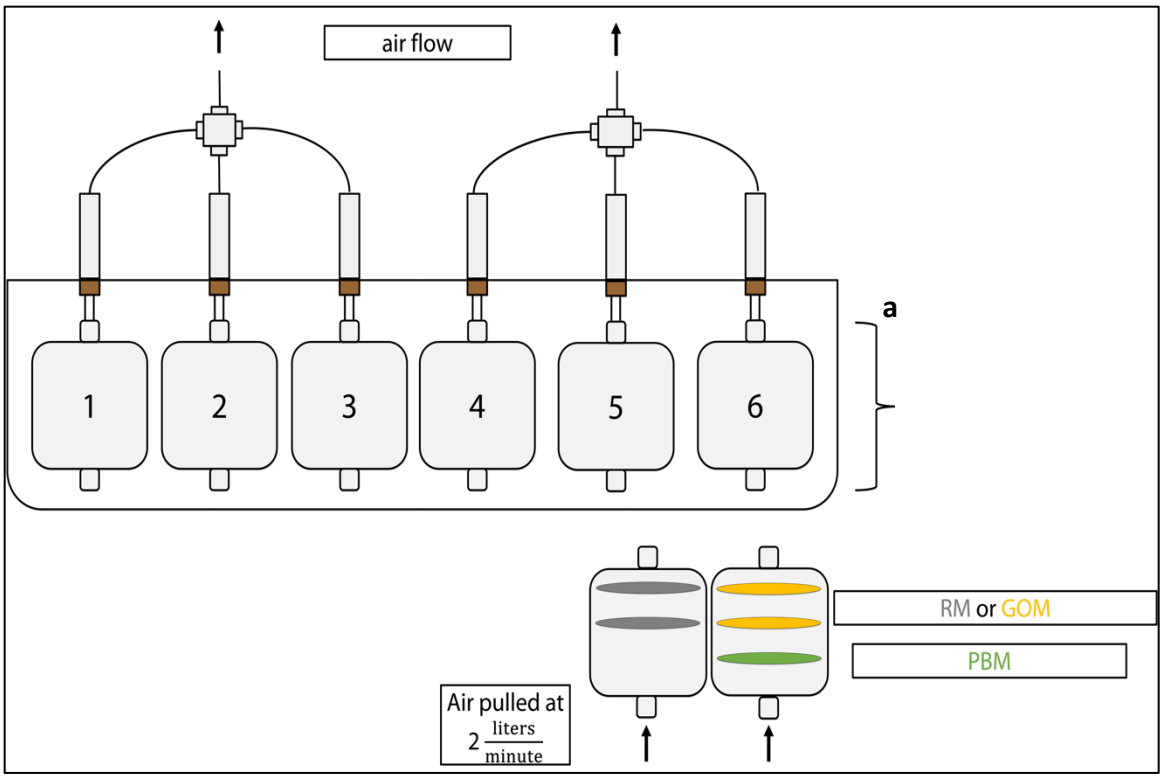

Figure 5. A schematic of the University of Nevada, Reno – Reactive Mercury Active System 2.0 (RMAS). Shown is the RMAS shield drawn around six membrane cartridges with a length **a** of ~ 100 mm. Shown above each membrane cartridge is the connection of 3 cartridges to one vacuum pump that pulls air at 1 or 2 L min^{-1}; air flow is represented by the small arrows. The arrow to the right points to a closer view of the membrane cartridges, which hold polytetrafluoroethylene membranes, colored in green, for particulate-bound mercury (PBM) measurements. Cation-exchange and nylon membranes are shown in gray and yellow which, dependent on the membrane configuration, measure gaseous oxidized mercury (GOM), and reactive mercury (RM; GOM + PBM).

Figure 6. Figure displays a map of all United States sampling sites discussed in Chapter 3. Site acronyms are: PEAV for Peavine Mountain; GH for Greenhouse; AISP for Antelope Island State Park at the Great Salt Lake; GUMO for Guadalupe Mountains National Park; and NRGT for Near-Road Georgia Tech in Atlanta, GA. The two Great Salt Lake sites indicate site relocation from AISP 1 to AISP 2 in September 2022.

Chapter 1 References

Amos, H. M., Jacob, D. J., Holmes, C. D., Fisher, J. A., Wang, Q., Yantosca, R. M., Corbitt, E. S., Galarneau, E., Rutter, A. P., Gustin, M. S., Steffen, A., Schauer, J. J., Graydon, J. A., Louis, V. L. St., Talbot, R. W., Edgerton, E. S., Zhang, Y., & Sunderland, E. M. (2012). Gas-particle partitioning of atmospheric Hg(II) and its effect on global mercury deposition. Atmospheric Chemistry and Physics, 12(1), 591–603. https://doi.org/10.5194/acp-12-591-2012

Bjørklund, G., Dadar, M., Mutter, J., & Aaseth, J. (2017). The toxicology of mercury: Current research and emerging trends. Environmental Research, 159, 545–554. https://doi.org/10.1016/j.envres.2017.08.051

Bu, X., Zhang, H., Lv, G., Lin, H., Chen, L., Yin, X., Shen, G., Yuan, W., Zhang, W., Wang, X., & Tong, Y. (2018). Comparison of reactive gaseous mercury collection by different sampling methods in a laboratory test and field monitoring. Environmental Science & Technology Letters, 5(10), 600–607. https://doi.org/10.1021/acs.estlett.8b00439

Castro, P. J., Kellö, V., Cernušák, I., & Dibble, T. S. (2022). Together, not separately, OH and O_3 oxidize Hg(0) to Hg(II) in the atmosphere. The Journal of Physical Chemistry A, 126(44), 8266–8279. https://doi.org/10.1021/acs.jpca.2c04364

Clarkson, T. W., Vyas, J. B., & Ballatori, N. (2007). Mechanisms of mercury disposition in the body. American Journal of Industrial Medicine, 50(10), 757–764. https://doi.org/10.1002/ajim.20476

Dunham-Cheatham, S. M., Lyman, S., & Gustin, M. S. (2020). Evaluation of sorption surface materials for reactive mercury compounds. Atmospheric Environment, 242, 117836. https://doi.org/10.1016/j.atmosenv.2020.117836

Dunham-Cheatham, S. M., Lyman, S., & Gustin, M. S. (2023). Comparison and calibration of methods for ambient reactive mercury quantification. Science of The Total Environment, 856, 159219. https://doi.org/10.1016/j.scitotenv.2022.159219

Ebinghaus, R., Jennings, S. G., Schroeder, W. H., Berg, T., Donaghy, T., Guentzel, J., Kenny, C., Kock, H. H., Kvietkus, K., Landing, W., Mühleck, T., Munthe, J., Prestbo, E. M., Schneeberger, D., Slemr, F., Sommar, J., Urba, A., Wallschläger, D., & Xiao, Z. (1999). International field intercomparison measurements of atmospheric mercury species at Mace Head, Ireland. Atmospheric Environment, 33(18), 3063–3073. https://doi.org/10.1016/S1352-2310(98)00119-8

Fu, X. W., Zhang, H., Yu, B., Wang, X., Lin, C.-J., & Feng, X. B. (2015). Observations of atmospheric mercury in China: A critical review. Atmospheric Chemistry and Physics, 15(16), 9455–9476. https://doi.org/10.5194/acp-15-9455-2015

Global Mercury Observation System (GMOS). (2023). GMOS Data Services. GMOS; GMOS. https://sdi.iia.cnr.it/gmos/

Gustin, M. S., Amos, H. M., Huang, J., Miller, M. B., & Heidecorn, K. (2015). Measuring and modeling mercury in the atmosphere: A critical review. Atmospheric Chemistry and Physics, 15(10), 5697–5713. https://doi.org/10.5194/acp-15-5697-2015

Gustin, M. S., Bank, M. S., Bishop, K., Bowman, K., Branfireun, B., Chételat, J., Eckley, C. S., Hammerschmidt, C. R., Lamborg, C., Lyman, S., Martínez-Cortizas, A., Sommar, J., Tsui, M. T.-K., & Zhang, T. (2020). Mercury biogeochemical cycling: A synthesis of

recent scientific advances. Science of The Total Environment, 737, 139619. https://doi.org/10.1016/j.scitotenv.2020.139619

Gustin, M. S., Dunham-Cheatham, S. M., Huang, J., Lindberg, S., & Lyman, S. N. (2021a). Development of an understanding of reactive mercury in ambient air: A review. Atmosphere, 12(1), 73. https://doi.org/10.3390/atmos12010073

Gustin, M. S., Dunham-Cheatham, S. M., Zhang, L., Lyman, S., Choma, N., & Castro, M. (2021b). Use of membranes and detailed HYSPLIT analyses to understand atmospheric particulate, gaseous oxidized, and reactive mercury chemistry. Environmental Science & Technology, 55(2), 893–901. https://doi.org/10.1021/acs.est.0c07876

Gustin, M. S., Huang, J., Miller, M. B., Peterson, C., Jaffe, D. A., Ambrose, J., Finley, B. D., Lyman, S. N., Call, K., Talbot, R., Feddersen, D., Mao, H., & Lindberg, S. E. (2013). Do we understand what the mercury speciation instruments are actually measuring? Results of RAMIX. Environmental Science & Technology, 47(13), 7295–7306. https://doi.org/10.1021/es3039104

Gworek, B., Dmuchowski, W., & Baczewska-Dąbrowska, A. H. (2020). Mercury in the terrestrial environment: A review. Environmental Sciences Europe, 32(1), 128. https://doi.org/10.1186/s12302-020-00401-x

Gwynn, J. W. (1996). Commonly asked questions about Utah's Great Salt Lake and ancient Lake Bonneville. Utah Geological Survey. https://books.google.com/books?hl=en&lr=&id=tMLy63t24F8C&oi=fnd&pg=PA1&dq=gwynn+mercury&ots=oSCTtq5ibG&sig=affEMBHHl82v_AfbKtKyL3ooHJw#v=onepage&q=gwynn%20mercury&f=false

Hachiya, N. (2006). The history and the present of Minamata disease - Entering the second half a century. Japan Medical Association Journal , 49(3), 112–118.

Huang, J., & Gustin, M. S. (2015). Uncertainties of gaseous oxidized mercury measurements using KCl-coated denuders, cation-exchange membranes, and nylon membranes: Humidity influences. Environmental Science & Technology, 49(10), 6102–6108. https://doi.org/10.1021/acs.est.5b00098

Huang, J., Miller, M. B., Weiss-Penzias, P., & Gustin, M. S. (2013). Comparison of gaseous oxidized Hg measured by KCl-coated denuders, and nylon and cation exchange membranes. Environmental Science & Technology, 47(13), 7307–7316. https://doi.org/10.1021/es4012349

Kao, L. W., & Rusyniak, D. E. (2019). Chronic poisoning: Trace metals and others. In Goldman-Cecil Medicine (Twenty Sixth Edition). Elsevier. https://www.clinicalkey.com.au/#!/content/book/3-s2.0-B9780323532662000199

Landis, M. S., Stevens, R. K., Schaedlich, F., & Prestbo, E. M. (2002). Development and characterization of an annular denuder methodology for the measurement of divalent inorganic reactive gaseous mercury in ambient air. Environmental Science & Technology, 36(13), 3000–3009. https://doi.org/10.1021/es015887t

Langford, N., & Ferner, R. (1999). Toxicity of mercury. Journal of Human Hypertension, 13(10), 651–656. https://doi.org/10.1038/sj.jhh.1000896

Lin, C.-J., Pongprueksa, P., Lindberg, S. E., Pehkonen, S. O., Byun, D., & Jang, C. (2006). Scientific uncertainties in atmospheric mercury models I: Model science evaluation. Atmospheric Environment, 40(16), 2911–2928. https://doi.org/10.1016/j.atmosenv.2006.01.009

Liu, M., Zhang, Q., Maavara, T., Liu, S., Wang, X., & Raymond, P. A. (2021). Rivers as the largest source of mercury to coastal oceans worldwide. Nature Geoscience, 14(9), 672–677. https://doi.org/10.1038/s41561-021-00793-2

Luippold, A., Gustin, M. S., Dunham-Cheatham, S. M., Castro, M., Luke, W., Lyman, S., & Zhang, L. (2020a). Use of multiple lines of evidence to understand reactive mercury concentrations and chemistry in Hawai'i, Nevada, Maryland, and Utah, USA. Environmental Science & Technology, 54(13), 7922–7931 https://doi.org/10.1021/acs.est.0c02283

Luippold, A., Gustin, M. S., Dunham-Cheatham, S. M., & Zhang, L. (2020b). Improvement of quantification and identification of atmospheric reactive mercury. Atmospheric Environment, 224, 117307. https://doi.org/10.1016/j.atmosenv.2020.117307

Lyman, S. N., Cheng, I., Gratz, L. E., Weiss-Penzias, P., & Zhang, L. (2020a). An updated review of atmospheric mercury. Science of The Total Environment, 707, 135575. https://doi.org/10.1016/j.scitotenv.2019.135575

Lyman, S. N., Gratz, L. E., Dunham-Cheatham, S. M., Gustin, M. S., & Luippold, A. (2020b). Improvements to the accuracy of atmospheric oxidized mercury measurements. Environmental Science & Technology, 54(21), 13379–13388. https://doi.org/10.1021/acs.est.0c02747

Lyman, S. N., Gustin, M. S., & Prestbo, E. M. (2010). A passive sampler for ambient gaseous oxidized mercury concentrations. Atmospheric Environment, 44(2), 246–252. https://doi.org/10.1016/j.atmosenv.2009.10.008

Lyman, S. N., Gustin, M. S., Prestbo, E. M., Kilner, P. I., Edgerton, E., & Hartsell, B. (2009). Testing and application of surrogate surfaces for understanding potential gaseous oxidized mercury dry deposition. Environmental Science & Technology, 43(16), 6235–6241. https://doi.org/10.1021/es901192e

Lyman, S. N., Gustin, M. S., Prestbo, E. M., & Marsik, F. J. (2007). Estimation of dry deposition of atmospheric mercury in Nevada by direct and indirect methods. Environmental Science & Technology, 41(6), 1970–1976. https://doi.org/10.1021/es062323m

Mahbub, K. R., Krishnan, K., Naidu, R., Andrews, S., & Megharaj, M. (2017). Mercury toxicity to terrestrial biota. Ecological Indicators, 74, 451–462. https://doi.org/10.1016/j.ecolind.2016.12.004

Mao, N., & Khalizov, A. (2021). Exchange reactions alter molecular speciation of gaseous oxidized mercury. ACS Earth and Space Chemistry, 5(8), 1842–1853. https://doi.org/10.1021/acsearthspacechem.1c00178

Mason, R. P., Choi, A. L., Fitzgerald, W. F., Hammerschmidt, C. R., Lamborg, C. H., Soerensen, A. L., & Sunderland, E. M. (2012). Mercury biogeochemical cycling in the ocean and policy implications. Environmental Research, 119, 101–117. https://doi.org/10.1016/j.envres.2012.03.013

Mason, R. P., Hammerschmidt, C. R., Lamborg, C. H., Bowman, K. L., Swarr, G. J., & Shelley, R. U. (2017). The air-sea exchange of mercury in the low latitude Pacific and Atlantic Oceans. Deep Sea Research Part I: Oceanographic Research Papers, 122, 17–28. https://doi.org/10.1016/j.dsr.2017.01.015

Miller, M. B., Dunham-Cheatham, S. M., Gustin, M. S., & Edwards, G. C. (2019). Evaluation of cation exchange membrane performance under exposure to high Hg(0) and $HgBr_2$

concentrations. Atmospheric Measurement Techniques, 12(2), 1207–1217. https://doi.org/10.5194/amt-12-1207-2019

Miller, M. B., Howard, D. A., Pierce, A. M., Cook, K. R., Keywood, M., Powell, J., Gustin, M. S., & Edwards, G. C. (2021). Atmospheric reactive mercury concentrations in coastal Australia and the Southern Ocean. Science of The Total Environment, 751, 141681. https://doi.org/10.1016/j.scitotenv.2020.141681

National Atmospheric Deposition Program (NADP) (2023a). Mercury Litterfall Network. NADP; Board of Regents of the University of Wisconsin System. https://nadp.slh.wisc.edu/networks/mercury-litterfall-network/

NADP (2023b). Mercury Deposition Network. NADP; Board of Regents of the University of Wisconsin System. https://nadp.slh.wisc.edu/networks/mercury-deposition-network/

O'Shea, J. G. (1990). 'Two minutes with Venus, two years with mercury'-Mercury as an antisyphilitic chemotherapeutic agent. Journal of the Royal Society of Medicine, 83(6), 392–395. https://doi.org/10.1177/014107689008300619

Osterwalder, S., Dunham-Cheatham, S. M., Ferreira Araujo, B., Magand, O., Thomas, J. L., Baladima, F., Pfaffhuber, K. A., Berg, T., Zhang, L., Huang, J., Dommergue, A., Sonke, J. E., & Gustin, M. S. (2021). Fate of springtime atmospheric reactive mercury: Concentrations and deposition at Zeppelin, Svalbard. ACS Earth and Space Chemistry, 5(11), 3234–3246. https://doi.org/10.1021/acsearthspacechem.1c00299

Outridge, P. M., Mason, R. P., Wang F., Guerrero S., & Heimbürger-Boavida L. E. (2018). Updated Global and Oceanic Mercury Budgets for the United Nations Global Mercury Assessment 2018. Environmental Science and Technology, 52(20), 11466 – 11477. https://doi.org/10.1021/acs.est.8b01246

Park, J.-D., & Zheng, W. (2012). Human exposure and health effects of inorganic and elemental mercury. Journal of Preventive Medicine & Public Health, 45(6), 344–352. https://doi.org/10.3961/jpmph.2012.45.6.344

Peterson, C., Alishahi, M., & Gustin, M. S. (2012). Testing the use of passive sampling systems for understanding air mercury concentrations and dry deposition across Florida, USA. Science of The Total Environment, 424, 297–307. https://doi.org/10.1016/j.scitotenv.2012.02.031

Peterson, C., & Gustin, M. (2008). Mercury in the air, water and biota at the Great Salt Lake (Utah, USA). Science of The Total Environment, 405(1–3), 255–268. https://doi.org/10.1016/j.scitotenv.2008.06.046

Ravichandran, M. (2004). Interactions between mercury and dissolved organic matter - A review. Chemosphere, 55(3), 319–331. https://doi.org/10.1016/j.chemosphere.2003.11.011

Rutter, A. P., & Schauer, J. J. (2007). The impact of aerosol composition on the particle to gas partitioning of reactive mercury. Environmental Science & Technology, 41(11), 3934–3939. https://doi.org/10.1021/es062439i

Saiz-Lopez, A., Travnikov, O., Sonke, J. E., Thackray, C. P., Jacob, D. J., Carmona-García, J., Francés-Monerris, A., Roca-Sanjuán, D., Acuña, A. U., Dávalos, J. Z., Cuevas, C. A., Jiskra, M., Wang, F., Bieser, J., Plane, J. M. C., & Francisco, J. S. (2020). Photochemistry of oxidized Hg(I) and Hg(II) species suggests missing mercury oxidation in the troposphere. Proceedings of the National Academy of Sciences, 117(49), 30949–30956. https://doi.org/10.1073/pnas.1922486117

Selin, N. E. (2009). Global biogeochemical cycling of mercury: A review. Annual Review of Environment and Resources, 34(1), 43–63. https://doi.org/10.1146/annurev.environ.051308.084314

Sexauer Gustin, M., Pierce, A. M., Huang, J., Miller, M. B., Holmes, H. A., & Loria-Salazar, S. M. (2016). Evidence for different reactive Hg sources and chemical compounds at adjacent valley and high elevation locations. Environmental Science & Technology, 50(22), 12225–12231. https://doi.org/10.1021/acs.est.6b03339

Sexauer Gustin, M., Weiss-Penzias, P. S., & Peterson, C. (2012). Investigating sources of gaseous oxidized mercury in dry deposition at three sites across Florida, USA. Atmospheric Chemistry and Physics, 12(19), 9201–9219. https://doi.org/10.5194/acp-12-9201-2012

Shah, V., Jacob, D. J., Thackray, C. P., Wang, X., Sunderland, E. M., Dibble, T. S., Saiz-Lopez, A., Černušák, I., Kellö, V., Castro, P. J., Wu, R., & Wang, C. (2021). Improved mechanistic model of the atmospheric redox chemistry of mercury. Environmental Science & Technology, 55(21), 14445–14456. https://doi.org/10.1021/acs.est.1c03160

Sheu, G.-R., & Mason, R. P. (2001). An examination of methods for the measurements of reactive gaseous mercury in the atmosphere. Environmental Science & Technology, 35(6), 1209–1216. https://doi.org/10.1021/es001183s

Si, L., & Ariya, P. (2018). Recent advances in atmospheric chemistry of mercury. Atmosphere, 9(2), 76. https://doi.org/10.3390/atmos9020076

Slemr, F., Ebinghaus, R., Brenninkmeijer, C. A. M., Hermann, M., Kock, H. H., Martinsson, B. G., Schuck, T., Sprung, D., Van Velthoven, P., Zahn, A., & Ziereis, H. (2009). Gaseous mercury distribution in the upper troposphere and lower stratosphere observed onboard the CARIBIC passenger aircraft. Atmospheric Chemistry and Physics, 9(6), 1957–1969. https://doi.org/10.5194/acp-9-1957-2009

Sprovieri, F., Pirrone, N., Bencardino, M., D'Amore, F., Carbone, F., Cinnirella, S., Mannarino, V., Landis, M., Ebinghaus, R., Weigelt, A., Brunke, E.-G., Labuschagne, C., Martin, L., Munthe, J., Wängberg, I., Artaxo, P., Morais, F., Barbosa, H. D. M. J., Brito, J., … Norstrom, C. (2016). Atmospheric mercury concentrations observed at ground-based monitoring sites globally distributed in the framework of the GMOS network. Atmospheric Chemistry and Physics, 16(18), 11915–11935. https://doi.org/10.5194/acp-16-11915-2016

Tang, Y., Wang, S., Li, G., Han, D., Liu, K., Li, Z., & Wu, Q. (2022). Elevated gaseous oxidized mercury revealed by a newly developed speciated atmospheric mercury monitoring system. Environmental Science & Technology, 56(12), 7707–7715. https://doi.org/10.1021/acs.est.2c01011

Tekran Instruments Corporation. (2022). Model 1135 particulate mercury unit. Tekran Instruments Corporation; Tekran Instruments Corporation. https://www.tekran.com/products/ambient-air/model-1135-particulate-mercury-unit/

Tørseth, K., Aas, W., Breivik, K., Fjæraa, A. M., Fiebig, M., Hjellbrekke, A. G., Lund Myhre, C., Solberg, S., & Yttri, K. E. (2012). Introduction to the European Monitoring and Evaluation Programme (EMEP) and observed atmospheric composition change during 1972–2009. Atmospheric Chemistry and Physics, 12(12), 5447–5481. https://doi.org/10.5194/acp-12-5447-2012

United Nations Environment Programme (UNEP), Chemicals and Health Branch. (2019). Global mercury assessment 2018. UNEP.

UNEP (2016). Global Review of Mercury Monitoring Networks. Figure 3, p. 22. https://wedocs.unep.org/20.500.11822/31268.

United States Environmental Protection Agency (U.S. EPA). (2023, February 21). Mercury in consumer products [Overviews and Factsheets]. U.S. EPA. https://www.epa.gov/mercury/mercury-consumer-products

U.S. EPA. (2002). Method 1631, Revision E: Mercury in water by oxidation, purge and trap, and cold vapor atomic fluorescence spectrometry, p. 45. U.S. EPA Washington, DC.

U.S. Geological Survey. (n.d.). Why Is the Ocean Salty?. U.S. Geological Survey. https://www.usgs.gov/faqs/why-ocean-salty

Utah Department of Environmental Quality (UDEQ). (2021, July 16). Utah waterfowl advisories. Utah Department of Environmental Quality. https://deq.utah.gov/water-quality/utah-waterfowl-advisories

Weigelt, A., Ebinghaus, R., Pirrone, N., Bieser, J., Bödewadt, J., Esposito, G., Slemr, F., Van Velthoven, P. F. J., Zahn, A., & Ziereis, H. (2016). Tropospheric mercury vertical profiles between 500 and 10,000 m in central Europe. Atmospheric Chemistry and Physics, 16(6), 4135–4146. https://doi.org/10.5194/acp-16-4135-2016

Wexler, P. (Ed.). (2014). Encyclopedia of toxicology (Third edition). Academic Press.

Wolfe, M. F., Schwarzbach, S., & Sulaiman, R. A. (1998). Effects of mercury on wildlife: A comprehensive review. Environmental Toxicology and Chemistry, 17(2), 146–160. https://doi.org/10.1002/etc.5620170203

Wujastyk, D. (2015). Histories of mercury in medicine across Asia and beyond. Asiatische Studien - Études Asiatiques, 69(4), 819–830. https://doi.org/10.1515/asia-2015-1051

Wurtsbaugh, W. A., Leavitt, P. R., & Moser, K. A. (2020). Effects of a century of mining and industrial production on metal contamination of a model saline ecosystem, Great Salt Lake, Utah. Environmental Pollution, 266, 115072. https://doi.org/10.1016/j.envpol.2020.115072

Yorifuji, T., & Tsuda, T. (2014). Minamata. In Encyclopedia of Toxicology (pp. 340–344). Elsevier. https://doi.org/10.1016/B978-0-12-386454-3.00038-5

Zhang, H., Fu, X., Wang, X., & Feng, X. (2019). Measurements and distribution of atmospheric particulate-bound mercury: A review. Bulletin of Environmental Contamination and Toxicology, 103(1), 48–54. https://doi.org/10.1007/s00128-019-02663-5

Zhou, J., & Obrist, D. (2021). Global mercury assimilation by vegetation. Environmental Science & Technology, 55(20), 14245–14257. https://doi.org/10.1021/acs.est.1c03530

Chapter 2: Investigation of Factors Impacting Measurement of Atmospheric Reactive Mercury

Abstract

The mercury (Hg) community needs a method to accurately measure concentrations and identify the chemistry of ambient gaseous oxidized and particulate-bound Hg, together referred to as reactive mercury (RM). The University of Nevada, Reno – Reactive Mercury Active System (RMAS) provides a more accurate alternate method to measure atmospheric RM than the industry standard, the Tekran 1130/1135/2537 system. However, RMAS measurements have limitations, including a long sampling time resolution and sampling biases associated with membranes. Also, recently it was demonstrated that RM concentrations measured by the RMAS were 30 to 50% lower than RM measured by two simultaneously operating dual-channel systems. Experiments carried out showed that increasing the RMAS flow rate negatively impacted RM concentrations, but not chemistry, membranes currently being used are better than alternatives with similar composition, and lower RM concentrations measured by the RMAS relative to two dual-channel systems cannot be attributed to RM sorption on the cartridge holding the membranes. Future work should focus on the establishment of a standard method to measure and calibrate RM to be used within the Hg community.

Introduction

Mercury (Hg) is a hazardous pollutant, and atmospheric background concentrations have increased by 450% since the nineteenth century due to anthropogenic activities (Outridge et al., 2018). Hg exists in the atmosphere as gaseous elemental mercury (GEM or Hg(0), the dominant form), gaseous oxidized mercury (GOM or

Hg(II), emitted from anthropogenic sources and formed via chemical reactions), and particulate-bound mercury (PBM, generated by GOM interactions with atmospheric aerosol) (Lyman et al., 2020). Together, GOM and PBM are commonly operationally defined as reactive mercury (RM = GOM + PBM). In the atmosphere, GEM is relatively inert and can be globally transported, while GOM and PBM have a shorter lifespan due to removal by precipitation and higher dry deposition rates (Lyman et al., 2020).

RM measurement methods were largely developed and researched in the late 1990s and early 2000s, during which sorption surfaces were tested (Landis et al., 2002; Ebinghaus et al., 2001; Munthe et al., 2001; Sheu and Mason, 2001). The potassium chloride (KCl) coated denuder, that reportedly selectively sorbs GOM, became the most widely used method to measure atmospheric RM and is a component of the standard instrument used to measure atmospheric Hg, the Tekran 1130/1135/2537 system (Tekran). In the late 2000s and early 2010s researchers began to observe ambient RM concentrations measured by alternate methods (e.g., membrane collection, dual-channel system (DCS), etc.) that were 2- to 3-fold higher than a simultaneously operating Tekran (Gustin et al., 2013). Since these initial developments, the KCl-denuder method has been shown to make inaccurate measurements (Gustin et al., 2021a). Promising alternate methods, including the University of Nevada, Reno – Reactive Mercury Active System (RMAS) and DCS, have been shown to make more accurate measurements, as demonstrated using a custom designed calibrator (Dunham-Cheatham et al., 2023; Lyman et al., 2020). The RMAS is an active sampling system that, through membrane sorption surfaces, allows for the measurement of RM, PBM, and GOM concentrations, and qualitatively identifies RM chemistry. The implementation of different types of

membranes in the RMAS enables measurements of RM or GOM using cation exchange membranes (CEM), identification of RM or GOM chemistry using nylon membranes, and PBM is measured using a polytetrafluoroethylene (PTFE) membrane, located upstream of CEM or nylon membranes (i.e., the RMAS+P). DCSs use the Tekran 2537 to quantify total gaseous mercury (TGM) and GEM using two channels. One channel reduces all sample air to GEM, using a pyrolyzer, and quantifies TGM by the Tekran 2537. The second channel contains a CEM to remove GOM and PBM, allowing just GEM to be quantified, and RM concentrations are calculated by difference (TGM – GEM).

However, the RMAS is not without its own limitations. For example, the RMAS requires a long sampling deployment (e.g., 1 to 2 weeks) to collect detectable Hg on the membranes, while the DCS requires 10 minutes. Also, RMAS membranes have been historically purchased from two vendors, and membrane inefficiencies have been identified: the CEM retains more RM under high humidity (Huang and Gustin, 2015); nylon membranes experience decreased RM retention under increasing ambient humidity and ozone (Huang and Gustin, 2015), and do not retain RM nitrogen compounds well (Luippold et al., 2020a); and PTFE membranes most likely retain some GOM (Gustin et al., 2015). Lastly, a recent RM sampling system intercomparison demonstrated that the Utah State University and UNR DCS measurements of GOM were 50 and 30% higher, respectively, than RM measured by the RMAS (Dunham-Cheatham et al., 2023). Therefore, the RMAS was potentially losing RM during the long deployments and this process needs to be better understood.

Because the required RMAS sampling resolution can be up to two weeks for pristine areas at a flow rate of 1 Lpm, the effect of increasing the flow rate to 2 Lpm on Hg measurements was investigated here. In addition, the limitations of the membranes used in the RMAS indicates new surfaces need to be identified. Thus, several alternate commercial membranes with similar composition were deployed to check their performance relative to the historically used membranes. Lastly, the question as to whether sorption of RM to the RMAS membrane cartridge accounts for the RM concentration discrepancies observed between the RMAS and DCS was addressed.

Methods

1. University of Nevada, Reno – Reactive Mercury Active System (UNR – RMAS)

Three RMAS were used to perform experiments. The RMAS is an active sampling system with pumps that pull ambient air through 47 mm dual- or three-staged perfluoroalkoxy alkane membrane cartridges (Savillex) at 1 to 2 Lpm for one or two-week sampling deployments. Membranes historically used to measure RM and PBM concentrations include CEM (Pall Corporation, S80570; 0.65 μm (i.e., pore size)) and PTFE membranes (Sartorius Stedium Biotech, 1180747N; 0.2 μm), respectively. The CEM membrane is a polyethersulfone (PES) material, proprietarily treated to preferentially sorb cations, and was purchased in sheets that were cut into 47 mm diameter discs using a steel cutting die. Historic RMAS nylon membranes are from Sartorius Stedium Biotech (Sartorius (0.2 μm (i.e., pore size)); 2500747N; 0.2 μm) and were used to determine RM chemistry.

Within each membrane cartridge, two nylon or two CEM membranes were deployed. The membrane closest to the sampling inlet was the upstream membrane, and

the subsequent membrane was the downstream membrane; the downstream membrane was used to calculate breakthrough of Hg from the upstream membrane. In the RMAS+P configuration, a third membrane (i.e., PTFE) was placed upstream of the two membranes to capture PBM (> 0.2 μm), while the two downstream membranes then captured GOM. For all experiments in this study, triplicate blank samples of each membrane type were taken at the beginning of each sampling deployment and the mean of the blank samples was subtracted from the mass of Hg quantified on each sample membrane. Membrane concentrations were calculated as follows:

Equation 1

$$\text{Total PBM or RM and GOM on membrane (pg Hg m}^{-3}) = \frac{\text{pg of Hg on membranes (PTFE} - \text{blank) or (upstream} - \text{blank)} + \text{(downstream} - \text{blank)}}{\text{volume of air in m}^3}$$

where, "blank" represents the mean Hg collected by the triplicate blank samples. Percent breakthrough of RM was calculated as:

Equation 2

$$\%\ \text{breakthrough of Hg (pg Hg m}^{-3}) = \frac{\text{pg Hg on (downstream – blank)}}{\text{pg Hg on (upstream – blank) + (downstream – blank)}}\ \text{x } 100$$

Data were removed when the downstream membrane measured higher RM than the upstream membrane, as this was indicative of an upstream membrane that was not flush with the support stage in the membrane cartridge, this occurred less than 5 times.

2. Sampling Location

All experiments were performed at the UNR College of Agriculture, Biotechnology & Natural Resources Agricultural Experiment Station Valley Road Greenhouse Complex (39.5375, −119.8047, 1367.6 meters above sea level (masl))

(Figure supplemental (S)1). This sampling location was the setting for previous RMAS experiments (Dunham-Cheatham et al., 2020; Luippold et al., 2020b). The site was impacted by vehicle emissions, as it was located adjacent (100 m) to Interstate-80, and the long-range transport of pollutants (Luippold et al., 2020a; Gustin et al., 2021b). Spring and summer deployments were characterized by high temperatures (> 20 °C) and solar radiation (~ 300 W m^{-2}), and low relative humidity (< 35%), conditions favoring GEM oxidation to RM (Lyman and Gustin, 2009; Table S2). Increasingly lower ambient temperatures (< 15 °C) and solar radiation (~ 150 W m^{-2}), and increasing precipitation and relative humidity (~ 50%), were observed through the fall and winter deployments (Lyman and Gustin, 2009; Weiss-Penzias et al., 2009; Table S2). Although Hg sources and chemistry are not the focus of this study, ambient air influences are important to describe as they may help explain results of the RMAS experiments.

3. RMAS Experiments

RMAS experiments were performed for at least five, one-week long deployments (± 1-2 days) and included comparing RMAS data collected at two flow rates, an intercomparison of historical RMAS and alternate membrane measurements, and an experiment to determine whether sorption of RM to the membrane cartridges was occurring. Table 1 presents when each experiment occurred and for how long.

3.1 Flow Rate Variation Experiment

To potentially improve the time resolution of RMAS RM measurements, concentrations were compared when sampling at 1 and 2 Lpm. For each deployment, triplicate dual-staged membrane cartridges with CEM or nylon membranes were installed

on two co-located RMAS shields. Flow rates were controlled by critical flow orifices (Teledyne API, 941100 (1 Lpm) and 941700 (2 Lpm)).

3.2 Alternate Membrane Comparisons

In addition to RMAS membrane limitations, access to membranes may be limited by vendor availability, geographic location, or economic feasibility. Therefore, alternate commercially available membrane materials were identified to assess whether the membranes measure similar RM concentrations and chemistry to the membranes historically used in the RMAS. Dual- and three-staged membrane cartridges with historical and alternate membrane types were installed on, up to three RMAS, all sampling at a flow rate of 2 Lpm. Information on all membranes is listed in Table S1. Available electron microscope images of the membranes tested are included in Figure S2.

3.2.1 Alternate CEM Comparison

Hg researchers have previously deployed CEM and PES membranes to measure RM, because they consist of the same base material, but these membranes have not been extensively compared (cf., Araujo et al., 2022; Gustin et al., 2021b; Marusczak et al., 2017; Sheu and Mason, 2001). For this experiment, alternate PES membranes consisted of Sterlitech (PES0847100; 0.8 μm) and Cole-Parmer (361-3811-CP; 0.45 μm, 90 mm diameter cut to 47 mm).

3.2.2 Alternate Nylon Membrane Comparison

Nylon membranes are the only material identified thus far that is compatible with the RMAS thermal desorption analysis. Yet, apart from the Sartorius nylon membrane, no other nylon membrane has been used for RM chemistry identification, and due to collection inefficiencies, there is a demonstrated need to identify an alternate membrane.

Tested alternate nylon membranes consisted of Sterlitech (Sterlitech (0.2 μm); NY0247100 and Sterlitech (0.8 μm); NY0847100), and Whatman nylon membranes (Whatman (0.2 μm); 7402-004 and Whatman (0.8 μm); 7408-004).

3.2.3 Alternate PTFE Membrane Comparison

Membranes used to measure PBM have included glass, quartz, and cellulose membranes, but no standard PBM method has been identified (Gustin et al., 2015; Lu and Schroeder, 1998). The historical Sartorius PTFE membrane was deployed alongside VWR glass fiber filter (28333-139; 1.2 μm), the membrane deployed to measure PBM in the Tekran 1135 module, and Whatman (3827-047; 1.5 μm) glass microfiber membranes, upstream of two nylon membranes (i.e., RMAS+P). Nylon membranes were selected as the downstream membranes to determine whether the upstream PBM membranes contributed to the alteration of downstream GOM chemistry during the experiment.

3.3 Membrane Cartridge Sorption Experiment

CEM deployed in the RMAS were recently shown to measure 50 and 30% less RM than a simultaneously operating Utah State University and UNR DCS, respectively (Dunham-Cheatham et al., 2023). One explanation could be retention of RM by the RMAS membrane cartridge. To test whether sorption of RM to the membrane cartridge was occurring, dual-staged membrane cartridges with and without CEM were deployed when RM concentrations are highest at the sampling location (i.e., summer).

To quantify RM sorption to the membrane cartridge, the cartridge was separated into its inlet and outlet halves, the outlets included the support stages that hold the membranes (Figure S3). A 5% hydrochloric acid solution (HCl; Fisher Scientific, A466-1; Optima grade) was prepared to rinse each cartridge piece; 1% HCl was used for the

deployment occurring from July 12 to July 19, 2022. For the inlet rinse, 20 mL of acid was pipetted into the inlet, ensuring the acid touched all internal surfaces, and an additional 5 mL was pipetted in to ensure all RM was desorbed. The acid was then poured into a 40 mL glass vial with Teflon-lined septum cap (Cole-Parmer, UX-35206-86). For the outlet rinse, the two membrane cartridge stages were placed into a polystyrene weigh boat (Fisherbrand, 08-732-113) and 20 mL of acid was pipetted into the boat. For approximately one minute, the weigh boat was agitated, and then, the acid was poured into a 40 mL vial. Next, the upper half of the membrane cartridge was rinsed with 5 mL of acid and the acid added to the vial. All acid-rinsed samples were kept in a refrigerator and analyzed within 24 hours. Three, clean and unused, control membrane cartridges were rinsed following the same methods. The pg Hg on each membrane cartridge was calculated:

Equation 3

$$\text{Total pg Hg m}^{-3}\text{ on membrane cartridge} = \frac{((\text{inlet rinse (pg Hg) or outlet rinse (pg Hg)} - (5\%\ \text{HCl control rinse (pg Hg)})) + \text{clean filter holder (pg Hg))}}{\text{volume of air in m}^3}$$

4. Analytical Methods

The total Hg content of all upstream and downstream membranes, except for the upstream nylon membranes, was quantified using EPA method 1631 Revision E with subsequent analysis by cold vapor atomic fluorescence spectrometry using a Tekran 2600-IVS (U.S. EPA, 2002). Upstream nylon membranes were analyzed using the thermal desorption method described in Dunham-Cheatham et al. (2023) to identify and

quantify RM compounds. For more details about the analytical methods, see the Supplemental Information.

5. Ancillary Data

Meteorological measurements were continually recorded in 10 min increments for the duration of each experiment and were downloaded from the Western Regional Climate Center's website. The measurement station (39.53917, -119.8058; 1365 masl; https://wrcc.dri.edu/cgi-bin/rawMAIN2.pl?nvunrc) was located approximately 200 m from the RMAS sampling location. Recorded meteorological parameters included precipitation (mm), wind speed (m s^{-1}), mean air temperature (°C), relative humidity (%), and solar radiation (W m^{-2}). The mean of every ancillary data parameter during each RMAS experiment was calculated and is presented in Table S2.

6. Statistical Analyses

Regression analyses were performed in RStudio to compare RMAS concentration data (version 4.2.1, R Core Team, 2022). Reduced major axis regression, using the lmodel2 package (Legendre, 2018), was used to report slope, coefficient of determination (r^2), and p-values. The y-intercept was set to zero for all modeled regressions, because we can expect the x value (a RM concentration) to be zero when the y value (another RM concentration) is zero because blank membrane Hg was subtracted from all samples. The Grubbs' test was used to assess and remove outlier data (Komsta, 2022). The non-parametric Spearman rank-order correlation test was used when the linear regression model normality assumption was violated, and correlation coefficient r^2 and p-values were reported. T-tests were used to test for statistical similarity between: meteorological measurements; % breakthrough data from the Alternate CEM comparison; and the

sorption rinse data from the Membrane Sorption Test. T-tests were performed in Excel using the t-Test: Two-Sample Assuming Unequal Variances from the DataAnalysis ToolPack. For all statistical tests, $\alpha = 0.05$.

MATLAB vR2022a was used to perform thermal desorption peak deconvolution analyses using the peakfit package. Figures were generated using Microsoft PowerPoint (version 16.0) and Microsoft Excel (version 16.0).

Results and Discussion

1. Flow Rate Variation Experiment

During summer 2021, RM concentrations measured using nylon membranes at 1 versus 2 Lpm were positively correlated (Spearman, $r = 0.92$ and $p < 0.05$), and CEM were 10% less at 2 Lpm (Figure 1). In winter 2021, nylon membrane concentrations at 2 Lpm were 10% higher than at 1 Lpm, and concentrations on the CEM were lower by 50% at 2 Lpm (Figure 2). This experiment was redone in winter 2022, and nylon membrane concentrations at 2 Lpm were 10% less and CEM concentrations were lower by 30% at 2 Lpm (Figure 3).

Huang and Gustin (2015) described a positive interaction associated with the CEM and relative humidity due to the hydrophilic properties of the CEM which increases RM retention with humidity. This may explain why CEM concentrations were not consistent across summer and winter deployments because the CEM retention of RM was influenced by seasonal changes in humidity. The mean relative humidity during summer 2021 ($28 \pm 5\%$) was significantly lower than both winter deployments ($67 \pm 11\%$ and $70 \pm 10\%$) (t-tests, $p < 0.05$), and suggests that CEM retention decreased under higher humidity.

Nylon chemistry was not statistically compared, but peak area values were similar in some, but not all cases at 1 and 2 Lpm (Figures 4, S4 – S8). During summer 2021, oxide compounds composed the largest proportion of retained RM compounds (62 ± 5% (mean ± standard deviation)) until June 29, when the proportion of oxides declined and varied throughout the rest of the deployment (33 ± 13%). Simultaneously, all other RM compound proportions increased, without one species dominating, except slightly for sulfur compounds on August 24 (39 ± 2%) and halides on September 7 (42 ± 15%) (Figure S4 and S5). Between winter 2021 and 2022, RM chemistry was similar; sulfur compounds were high (36 ± 10%) and the mean proportion of organic compounds was 18 ± 7% that was higher than in summer 2021 (8 ± 3%) (Figures 4, S6 - S8).

Oxide compound proportion increased by 17%, from 10 ± 8% to 31 ± 10%, halide and sulfur proportion decreased by 4 and 11%, from 15 ± 8% and 42 ± 8% to 11 ± 3% and 31 ± 10%, and overall, RM concentrations increased from February 1 through February 22, 2022. These chemistry and concentration trends may be associated with the statistically significant increase, from the beginning of the winter 2021 deployment, in solar radiation (98 ± 21 W/m^2 and 150 ± 7 W/m^2) and decrease in relative humidity (75 ± 6% and 55 ± 3%), associated with the transition from winter to spring (t-tests, $p < 0.05$; Figures 4, S6).

2. Alternate Membrane Comparisons

2.1 Alternate CEM Comparison

In fall 2021, Sterlitech PES and CEM RM concentrations were positively correlated (Spearman, $r = 0.87$, $p < 0.05$). During winter 2022, the Sterlitech and Cole-

Parmer PES membranes collected 20 and 10% less RM than the CEM, respectively (Figure 5).

In fall 2021, Sterlitech PES mean % breakthrough (BT) was significantly lower (7 ± 3 pg m^{-3}) than CEM % BT (20 ± 6 pg m^{-3}) (t-test, $p < 0.05$). The same test in winter 2022 showed that Sterlitech and Cole-Parmer PES mean % BT values were significantly greater than in 2021, and were not significantly different from CEM % BT (t-tests, $p > 0.1$) (Figure 6).

2.2 Alternate Nylon Membrane Comparison

In fall 2021, the alternate Sterlitech (0.2 μm) and historical Sartorius (0.2 μm) membrane RM concentrations were positively correlated (Spearman, $r = 0.93$, $p < 0.05$). In summer 2022, the Sterlitech (0.2 μm) alternate nylon membrane retained 10% less RM than the Sartorius (0.2 μm) membrane (Figures 7-8). The experiment was repeated once in summer 2022 (n = 5) with a Sterlitech (0.8 μm) membrane that measured the same amount of RM as the Sartorius (0.2 μm) membrane (Figure 8). In summer 2022, the Whatman (0.2 μm) and Whatman (0.8 μm) membranes retained 30 to 40% and 40% less RM, respectively, than the Sartorius (0.2 μm) membrane (Figures 7-8).

During processing of alternate nylon membrane thermal desorption data, it was observed that using desorption temperatures from the historical desorption range produced desorption profiles that had high model error and low r^2 values. Due to this, the analysis was also performed using desorption temperatures outside of some compound desorption ranges and found lower model error and higher r^2 values. The thermal desorption results reported had the lowest model error and highest r^2 value of the historical and altered models. All desorption temperatures are reported in Table S3.

Alternate nylon membrane thermal desorption profiles were visually different from the Sartorius (0.2 μm) membrane, suggesting different chemistry collection (Figure 9). Because the alternate nylon membranes have not been loaded with known Hg compounds, we cannot predict what the profiles represented.

2.3 Alternate PTFE Membrane Comparison

During this experiment, PBM collected by the Whatman membranes was ~20% less than the Sartorius PTFE (Figure 10). Concentrations of PBM measured by the VWR membrane, used in the Tekran, relative to the Sartorius PTFE were positively correlated (Spearman, $r = 0.79$, $p < 0.05$).

The nylon membranes downstream of the VWR membrane collected no more than 7 pg GOM m^{-3} and retained approximately 90% less GOM than the nylon membranes downstream of the Sartorius PTFE (Figure 11). GOM degradation on quartz fiber membranes has been proposed (Gustin et al., 2013, Supplemental Information p. 5 - 6). Therefore, the VWR membrane here contributed to the reduction of GOM to GEM as it passed through, and little GOM was collected by the downstream nylon membranes. We know that the VWR membrane contributed to RM reduction, because the Sartorius (0.2 μm) nylon membranes do not retain GEM (Livia Lown, personal communication, 2023). Whatman glass microfiber nylon membrane GOM concentrations were 20% less than the downstream Sartorius PTFE membranes, also suggesting the potential for GOM reduction (Figure 11).

Peak area values were similar between the nylon membranes downstream of the Sartorius and Whatman PBM membranes, although not statistically compared (Figures 12, S9). Peak area values associated with the VWR membrane were almost always zero,

and were different from the other two membranes, due to GOM reduction by the VWR membrane (Figures 12, S9).

3. Membrane Cartridge Sorption Experiment

Overall, less than 5% of the RM that was quantified by the CEM was retained on the inside surfaces of the membrane cartridge, and thus was not considered a contributing factor to the RM concentration discrepancies seen between the RMAS and dual-channel systems in Dunham-Cheatham et al. (2023) (Figure 13).

The amount of RM that sorbed to the inlet piece of the membrane cartridge (4 ± 1 pg m^{-3}) with a CEM was greater than the RM sorbed to the outlet (0.2 ± 0.2 pg m^{-3}) (t-test, $p < 0.05$). This difference shows that the CEM retained RM and minimal RM passed through to be able to interact with the outlet piece.

Conclusion

Increasing the RMAS flow rate from 1 to 2 Lpm resulted in reduced RM retention by the CEM and nylon membranes, while it did not change chemistry measured by the nylon membranes. Further testing of operating the RMAS at 1 versus 2 Lpm should be done since the experiments showed good agreement in the winter, but not in the summer.

RM concentrations measured by the alternate PES membranes were lower than the historical CEM membranes. RM concentrations and chemistry collected by alternate nylon membranes could be different than the Sartorius (0.2 μm) membrane, thus alternate nylon membranes need to be calibrated with GOM compounds. Also, future work is in progress to produce a method to directly identify RM chemistry using a GC/MS that will shed light on the differences in nylon RM chemistry shown here. The VWR membrane, utilized in the Tekran 1135 module for PBM concentrations, contributed to the reduction

of sample GOM to GEM during this study. Thus, the Tekran measurements are unreliable. Less RM retention, but similar chemistry was observed between the Whatman and Sartorius PBM membranes during the experiment. However, in a recent laboratory experiment, the Whatman and VWR membranes both sorbed GOM, meaning that these are not suitable surfaces for PBM collection (Jan Gačnik, personal communication, 2023). Of all alternate membranes tested, no membrane measured higher concentrations or identified similar chemistry of RM to the historical membranes; therefore, no alternate membrane tested is recommended for measurements. Due to this, new surfaces must be identified or developed as the historical membranes are associated with influences that impact measurements.

A negligible amount (< 5%) of Hg was found to sorb on the membrane cartridge relative to a CEM during a seven-day RMAS deployment and thus, does not solely contribute to the discrepancies observed between RM measurements made by the RMAS and two DCSs in Dunham-Cheatham et al. (2023). The RMAS loss mechanism may be due to GOM reduction losses from the membranes themselves. A recent study has shown that GOM sorbed to a membrane surface, specifically, the Cole-Parmer PES membrane tested here, was subject to exchange interactions with co-adsorbed GOM and other chemical species. However, these results were obstained using GOM concentrations that were 5-orders of magnitude higher than ambient background concentrations (Mao and Khalizov et al., 2021). More testing is necessary to determine whether RMAS membranes influence RM retention.

Overall, the Hg community needs a calibrated standard measurement technique for atmospheric RM concentrations. Calibration and collection surface work is in

progress and eventually will provide an accurate standard method to measure concentrations and identify chemistry of ambient RM.

Chapter 2 Tables and Figures

Experiment	Dates	Deployments (n)
Flow Rate Variation	05/25/20–1 - 09/07/2021	CEM = 15; Nylon = 14
Flow Rate Variation	12/07/20–1 - 02/22/2022	11
Flow Rate Variation	11/17/20–2 - 12/22/2022	5
Alternate CEM	09/07/20–1 - 11/02/2021	8
Alternate CEM	11/17/20–2 - 12/22/2022	5
Alternate Nylon	09/07/20–1 - 11/02/2021	8
Alternate Nylon	05/10/20–2 - 06/21/2022	6
Alternate Nylon	08/02/20–2 - 09/06/2022	5
Alternate PTFE	09/06/20–2 - 11/17/2022	10
Membrane Cartridge Sorption	06/27/20–2 - 07/26/2022	5

Table 1. Table displaying all Reactive Mercury Active System experiments including when the experiment occurred (MM/DD/YYY) and the number of week-long deployments.

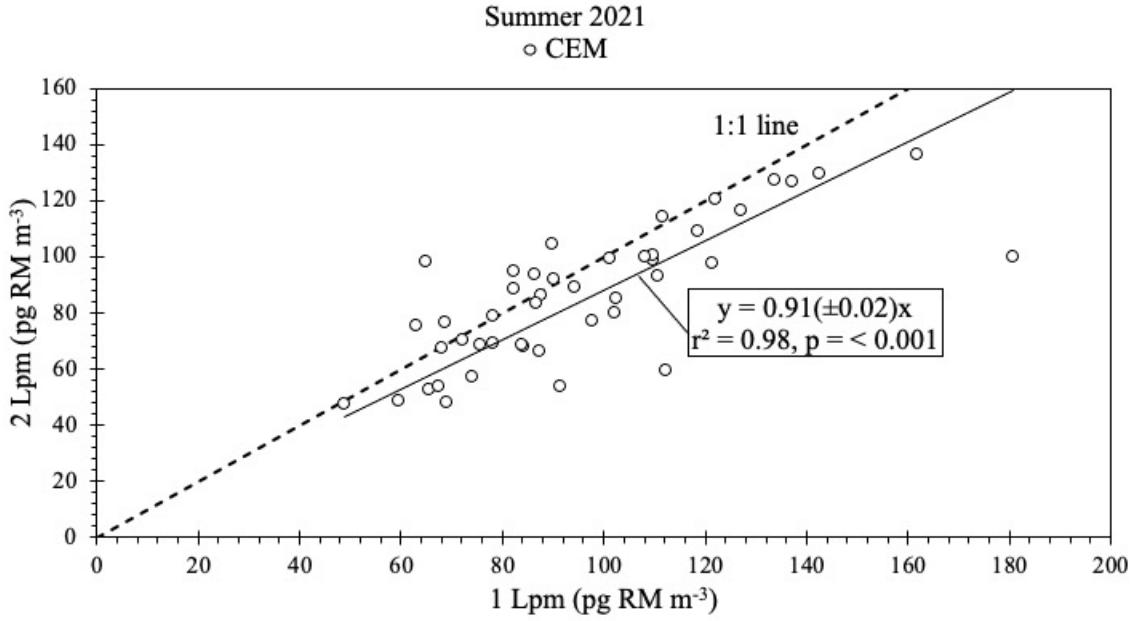

Figure 1. Regression plot of the nylon and CEM reactive mercury concentrations at 1 and 2 Lpm from May 25 to September 7, 2021 (summer 2021); the y-intercept was set to zero. Trendline equations and statistics shown are for reduced major axis regressions.

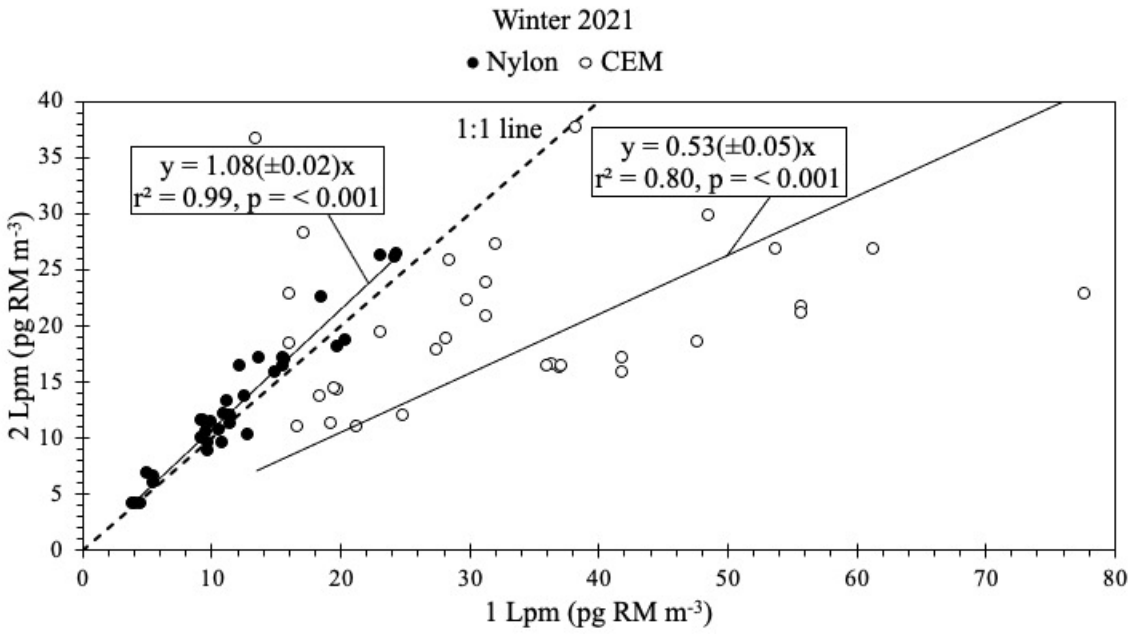

Figure 2. Regression plot of the nylon and CEM reactive mercury concentrations at 1 and 2 Lpm from December 7, 2021 to February 22, 2022 (winter 2021); the y-intercept was set to zero. Trendline equations and statistics shown are for reduced major axis regressions.

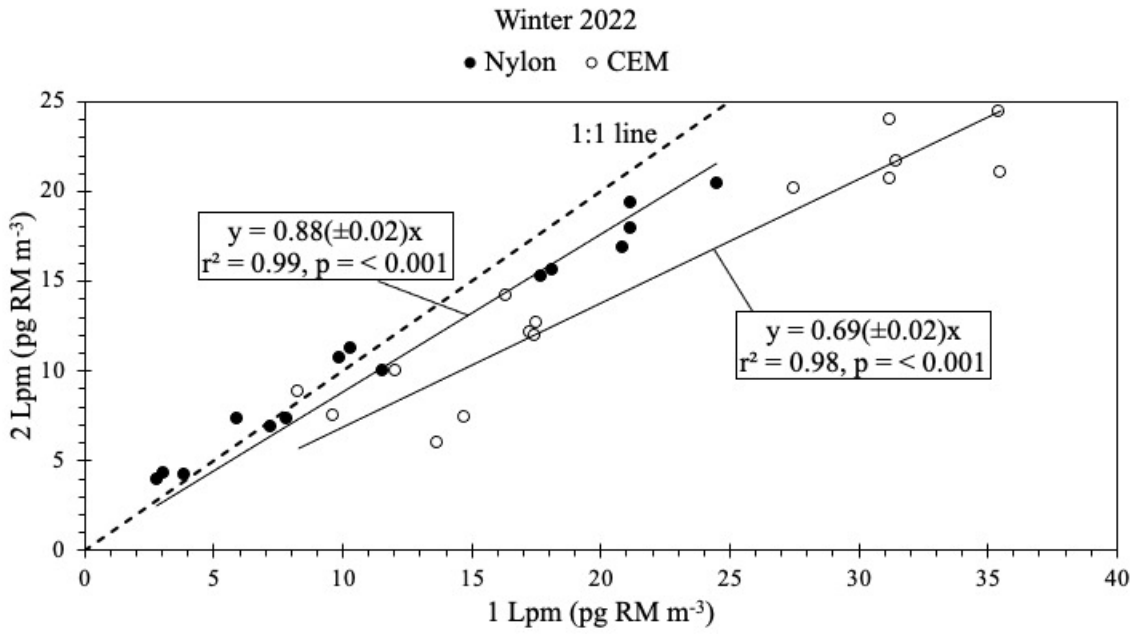

Figure 3. Regression plot of the nylon and CEM reactive mercury concentrations at 1 and 2 Lpm from November 17 to December 22, 2022 (winter 2022); the y-intercept was set to zero. Trendline equations and statistics shown are for reduced major axis regressions.

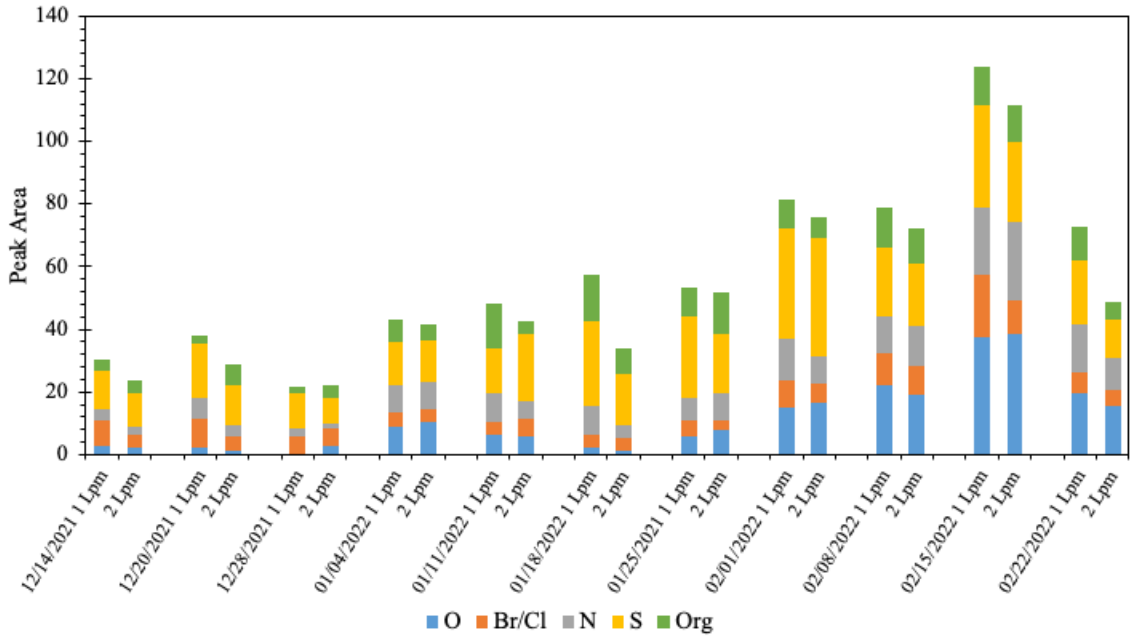

Figure 4. The peak area (pg RM m^{-3}) of the oxidized mercury compounds thermally desorbed from the Sartorius (0.2 µm) nylon membrane by sampling deployment from December 7, 2021 to February 22, 2022 (winter 2021). For each deployment date, the left bar represents the results at 1 Lpm and on the right, 2 Lpm. The dates represent the collection date (MM/DD/YYYY). See the Supplemental Information for the black and white figure (Figure S6).

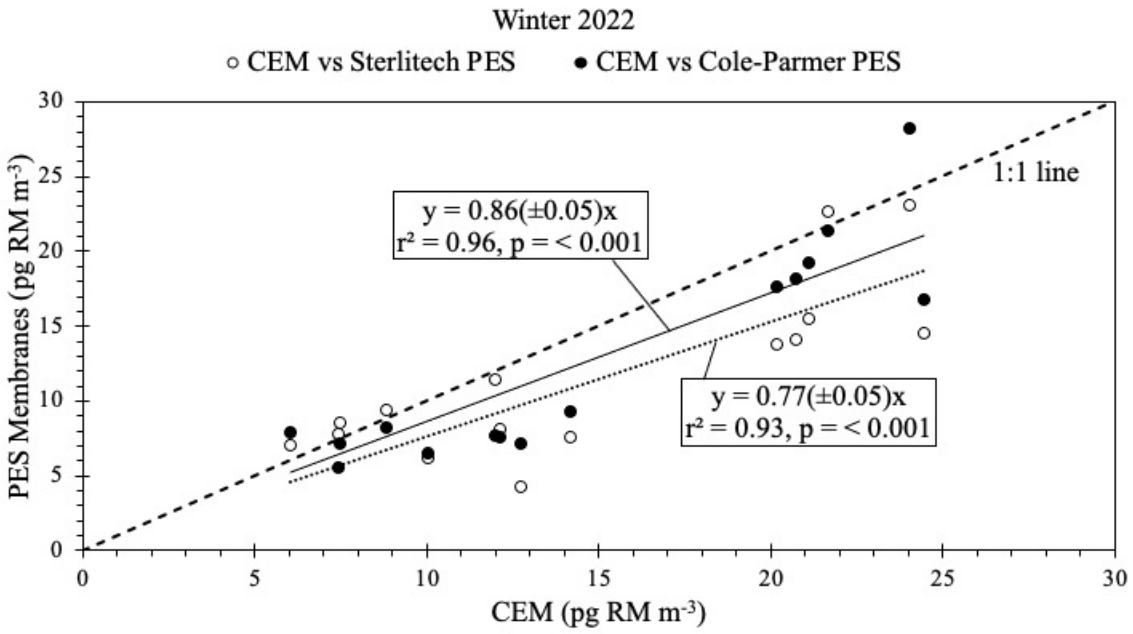

Figure 5. Regression plot of the Pall CEM, and alternate, Sterlitech and Cole-Parmer PES membrane reactive mercury concentrations from November 17 to December 22, 2022 (winter 2022); the y-intercept was set to zero. Trendline equations and statistics shown are for reduced major axis regressions.

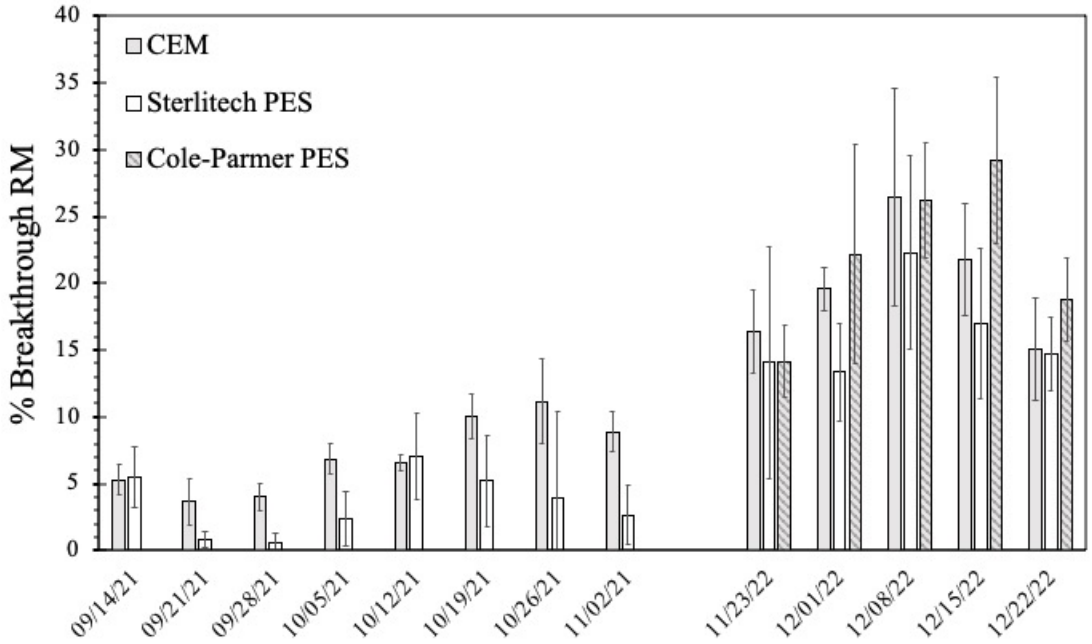

Figure 6. Bar plot of the percent (%) breakthrough of RM concentrations for the CEM and alternate, Sterlitech and Cole Parmer PES membranes by sampling deployment from September 7 to November 2, 2021 and November 23 to December 22, 2022 (non-consecutive dates on x-axis). Error bars represent ± 1 standard deviation (σ). The dates represent the collection date (MM/DD/YYYY).

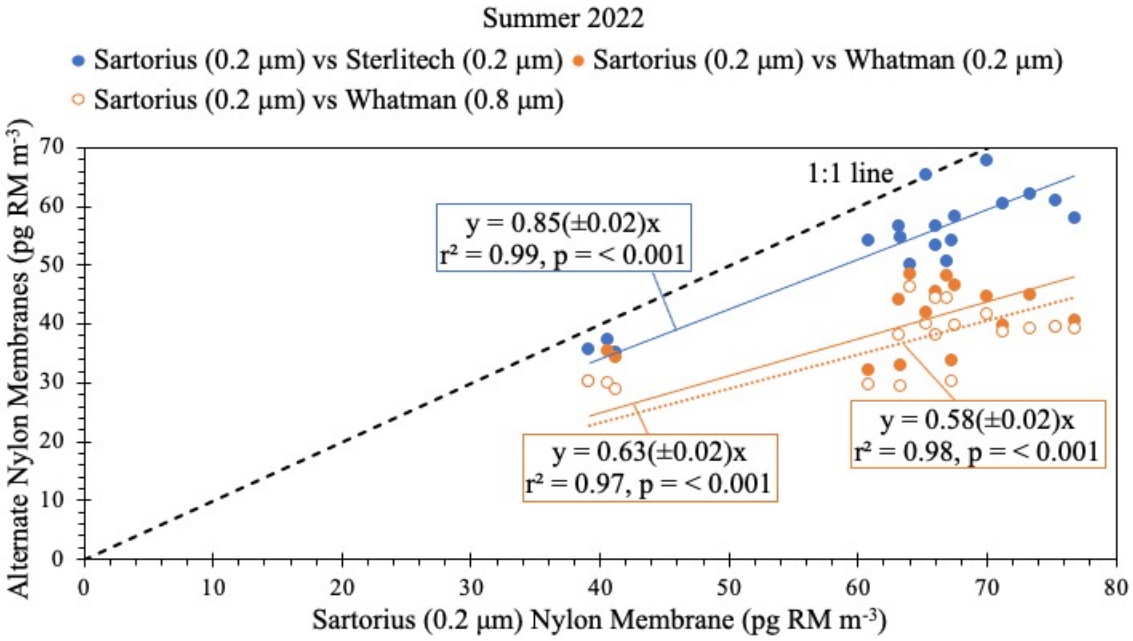

Figure 7. Regression plot of the Sartorius, and alternate Sterlitech (0.2 µm) and Whatman (0.2 and 0.8 µm) nylon membrane RM concentrations from May 10 to June 21, 2022 (summer 2022); the y-intercept was set to zero. Trendline equations and statistics shown are for reduced major axis regressions.

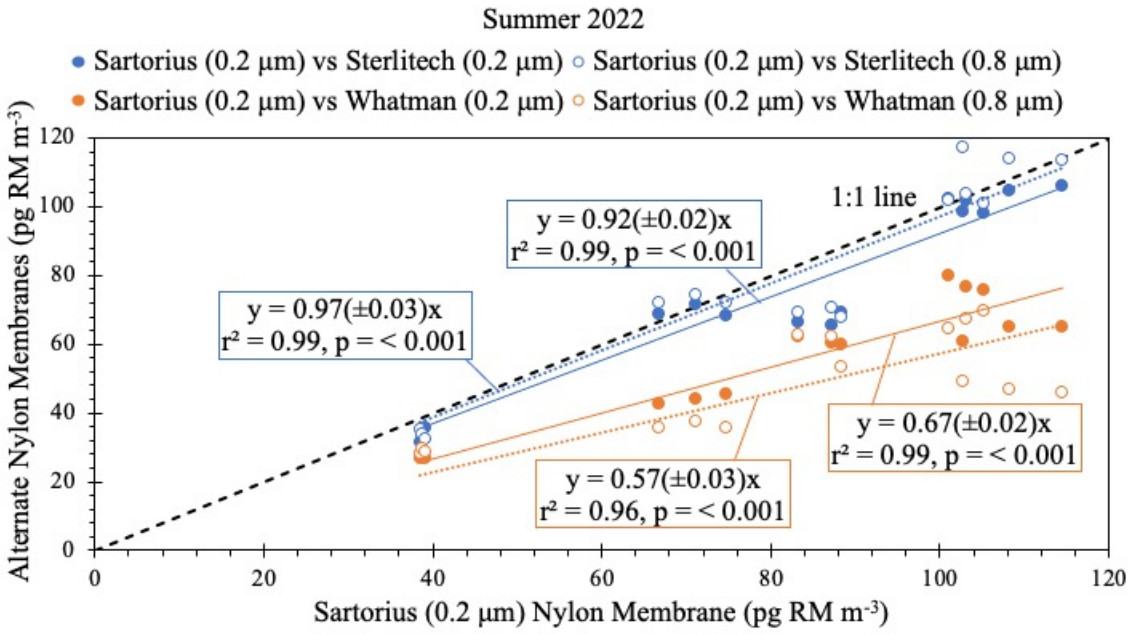

Figure 8. Regression plot of the Sartorius, and alternate Sterlitech (0.2 and 0.8 µm) and Whatman (0.2 and 0.8 µm) nylon membrane RM concentrations from August 2 to September 6, 2022 (summer 2022); the y-intercept was set to zero. Trendline equations and statistics shown are for reduced major axis regressions.

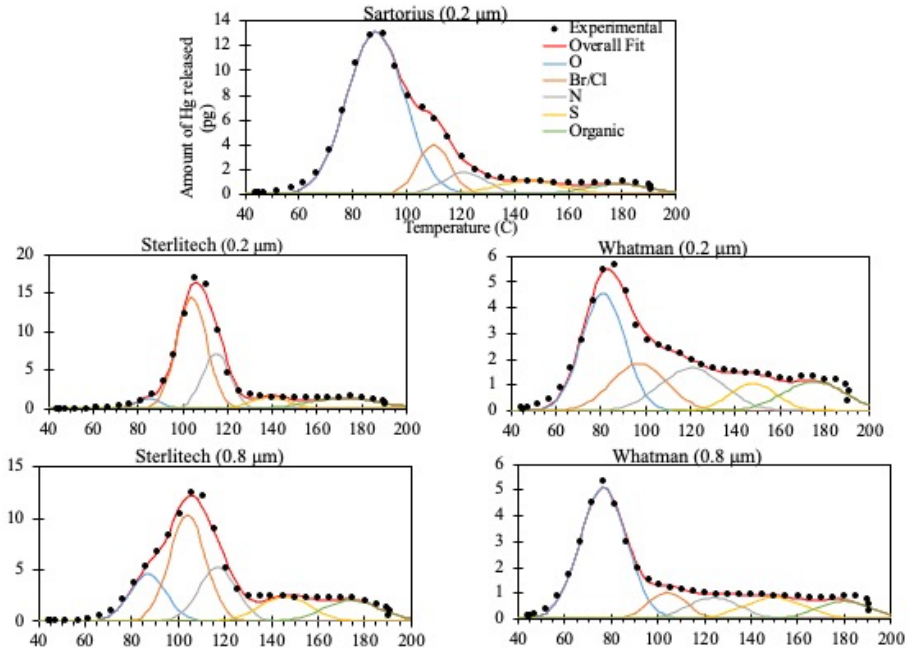

Figure 9. Figure displaying the thermal desorption profiles for each tested nylon membrane from the same deployment: August 23 to August 30, 2022.

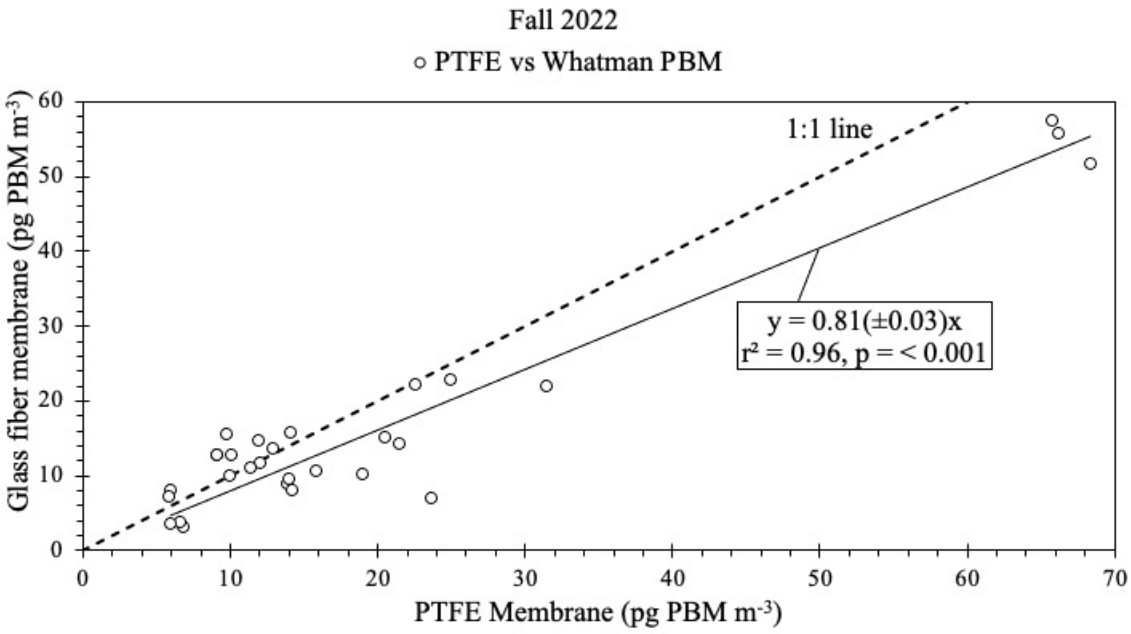

Figure 10. Regression plot of the Sartorius PTFE, and alternate, VWR glass fiber and Whatman glass microfiber membrane PBM concentrations from September 6 to November 17, 2022 (fall 2022); the y-intercept was set to zero. Trendline equations and statistics shown are for reduced major axis regressions.

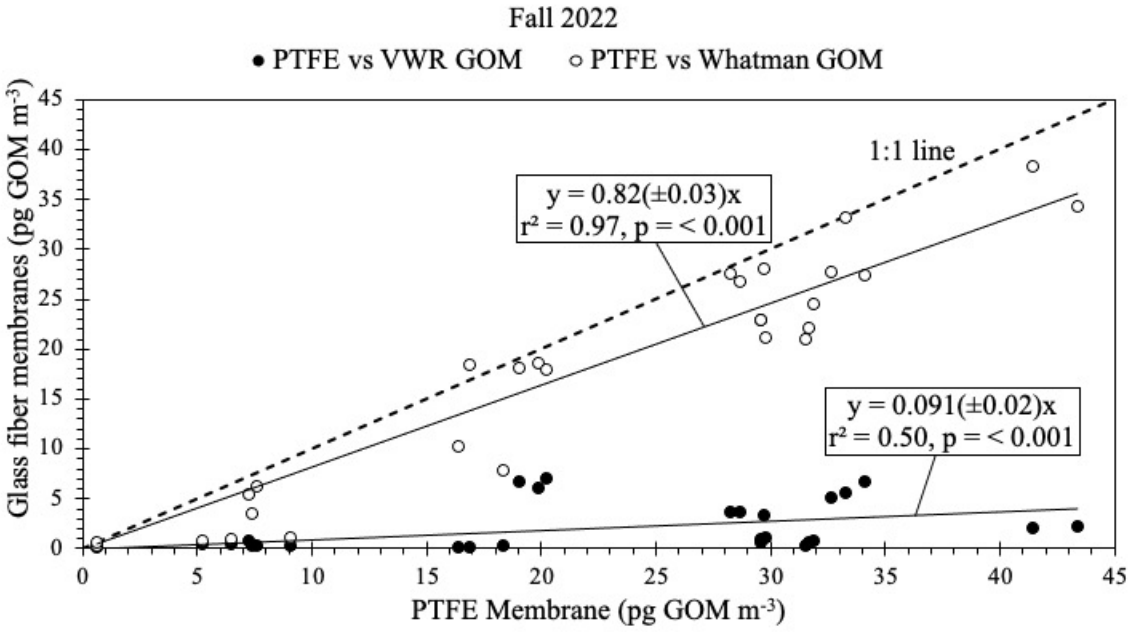

Figure 11. Regression plot of the nylon membrane GOM concentrations downstream of the Sartorius PTFE, and alternate, VWR glass fiber and Whatman glass microfiber membranes from September 6 to November 17, 2022 (fall 2022); the y-intercept was set to zero. Trendline equations and statistics shown are for reduced major axis regressions.

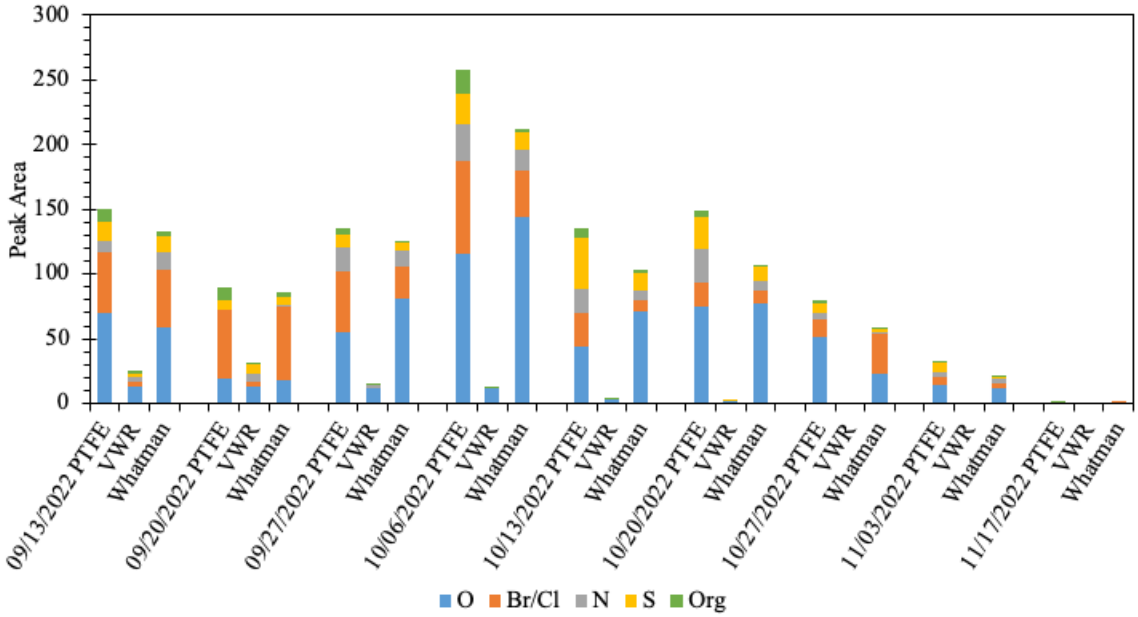

Figure 12. The peak area (pg GOM m^{-3}) of the oxidized mercury compounds thermally desorbed from the nylon membranes downstream of the Sartorius PTFE, and alternate VWR glass fiber and Whatman glass microfiber membranes from September 13 to November 17, 2022. The dates represent the collection date (MM/DD/YYYY). See the Supplemental Information for black and white figure (Figure S9).

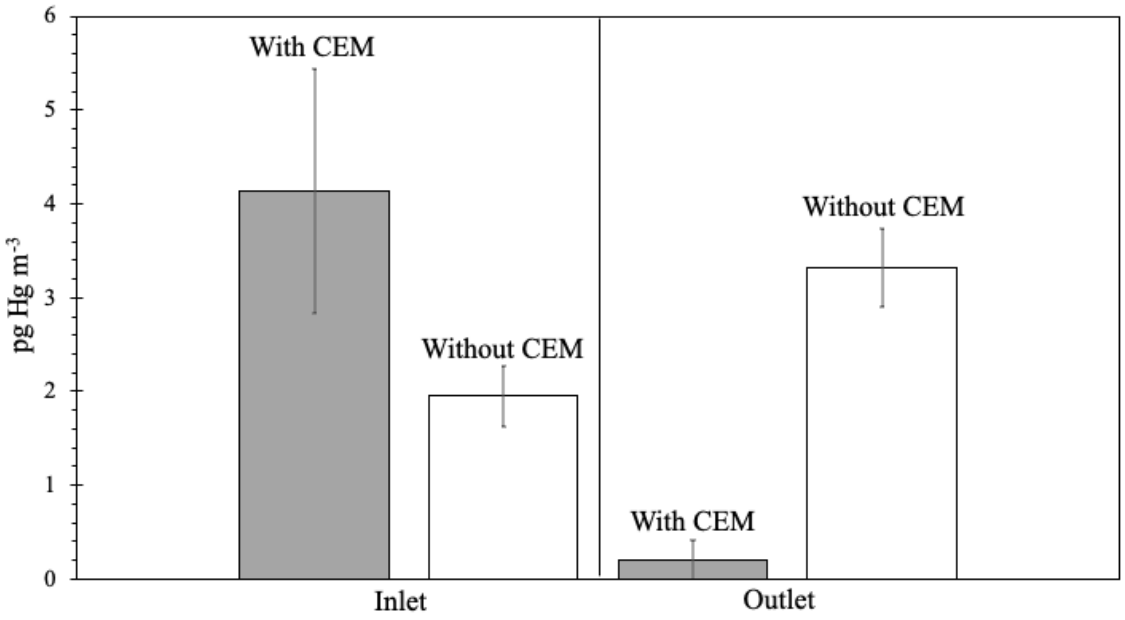

Figure 13. The mean total mercury concentrations (pg m^{-3}) quantified by the acid rinse of the membrane cartridges from June 27 to July 26, 2022. The membrane cartridge piece is defined on the x-axis and whether the cartridge deployed a cation-exchange membrane is defined by the bar color and above each bar. Error bars represent, ± 1 standard deviation (σ).

Chapter 2 References

Araujo, B. F., Osterwalder, S., Szponar, N., Lee, D., Petrova, M. V., Pernov, J. B., Ahmed, S., Heimbürger-Boavida, L.-E., Laffont, L., Teisserenc, R., Tananaev, N., Nordstrom, C., Magand, O., Stupple, G., Skov, H., Steffen, A., Bergquist, B., Pfaffhuber, K. A., Thomas, J. L., … Sonke, J. E. (2022). Mercury isotope evidence for Arctic summertime re-emission of mercury from the cryosphere. Nature Communications, 13(1), 4956. https://doi.org/10.1038/s41467-022-32440-8

Dunham-Cheatham, S. M., Lyman, S., & Gustin, M. S. (2020). Evaluation of sorption surface materials for reactive mercury compounds. Atmospheric Environment, 242, 117836. https://doi.org/10.1016/j.atmosenv.2020.117836

Dunham-Cheatham, S. M., Lyman, S., & Gustin, M. S. (2023). Comparison and calibration of methods for ambient reactive mercury quantification. Science of The Total Environment, 856, 159219. https://doi.org/10.1016/j.scitotenv.2022.159219

Ebinghaus, R., Jennings, S. G., Schroeder, W. H., Berg, T., Donaghy, T., Guentzel, J., Kenny, C., Kock, H. H., Kvietkus, K., Landing, W., Mühleck, T., Munthe, J., Prestbo, E. M., Schneeberger, D., Slemr, F., Sommar, J., Urba, A., Wallschläger, D., & Xiao, Z. (1999). International field intercomparison measurements of atmospheric mercury species at Mace Head, Ireland. Atmospheric Environment, 33(18), 3063–3073. https://doi.org/10.1016/S1352-2310(98)00119-8

United States Environmental Protection Agency (U.S. EPA). (2002). Method 1631, Revision E: Mercury in water by oxidation, purge and trap, and cold vapor atomic fluorescence spectrometry, p. 45. U.S. EPA Washington, DC.

Girden, E. R. (1992). ANOVA: Repeated measures. Sage Publications, Inc.

Gustin, M. S., Amos, H. M., Huang, J., Miller, M. B., & Heidecorn, K. (2015). Measuring and modeling mercury in the atmosphere: A critical review. Atmospheric Chemistry and Physics, 15(10), 5697–5713. https://doi.org/10.5194/acp-15-5697-2015

Gustin, M. S., Dunham-Cheatham, S. M., Huang, J., Lindberg, S., & Lyman, S. N. (2021a). Development of an understanding of reactive mercury in ambient air: A review. Atmosphere, 12(1), 73. https://doi.org/10.3390/atmos12010073

Gustin, M. S., Dunham-Cheatham, S. M., Zhang, L., Lyman, S., Choma, N., & Castro, M. (2021b). Use of membranes and detailed HYSPLIT analyses to understand atmospheric particulate, gaseous oxidized, and reactive mercury chemistry. Environmental Science & Technology, 55(2), 893–901. https://doi.org/10.1021/acs.est.0c07876

Gustin, M. S., Huang, J., Miller, M. B., Peterson, C., Jaffe, D. A., Ambrose, J., Finley, B. D., Lyman, S. N., Call, K., Talbot, R., Feddersen, D., Mao, H., & Lindberg, S. E. (2013). Do we understand what the mercury speciation instruments are actually measuring? Results of RAMIX. Environmental Science & Technology, 47(13), 7295–7306. https://doi.org/10.1021/es3039104

Huang, J., & Gustin, M. S. (2015). Uncertainties of gaseous oxidized mercury measurements using KCl-coated denuders, cation-exchange membranes, and nylon membranes: Humidity influences. Environmental Science & Technology, 49(10), 6102–6108. https://doi.org/10.1021/acs.est.5b00098

Komsta L (2022). _outliers: Tests for outliers. R package version 0.15, https://CRAN.R-project.org/package=outliers.

Landis, M. S., Stevens, R. K., Schaedlich, F., & Prestbo, E. M. (2002). Development and characterization of an annular denuder methodology for the measurement of divalent inorganic reactive gaseous mercury in ambient air. Environmental Science & Technology, 36(13), 3000–3009. https://doi.org/10.1021/es015887t

Legendre, P., 2018. Lmodel2: Model II regression. R package Version 1.7-3. CRAN.R.

Lu, J. Y., & Schroeder, W. H. (1999). Sampling and determination of particulate mercury in ambient air: A review. Water, air, & soil pollution. Water, Air, and Soil Pollution, 112(3/4), 279–295. https://doi.org/10.1023/A:1005057022001

Luippold, A., Gustin, M. S., Dunham-Cheatham, S. M., Castro, M., Luke, W., Lyman, S., & Zhang, L. (2020a). Use of multiple lines of evidence to understand reactive mercury concentrations and chemistry in Hawai'i, Nevada, Maryland, and Utah, USA. Environmental Science & Technology, 54(13), 7922–7931. https://doi.org/10.1021/acs.est.0c02283

Luippold, A., Gustin, M. S., Dunham-Cheatham, S. M., & Zhang, L. (2020b). Improvement of quantification and identification of atmospheric reactive mercury. Atmospheric Environment, 224, 117307. https://doi.org/10.1016/j.atmosenv.2020.117307

Lyman, S. N., Cheng, I., Gratz, L. E., Weiss-Penzias, P., & Zhang, L. (2020). An updated review of atmospheric mercury. Science of The Total Environment, 707, 135575. https://doi.org/10.1016/j.scitotenv.2019.135575

Lyman, S. N., & Gustin, M. S. (2009). Determinants of atmospheric mercury concentrations in Reno, Nevada, USA. Science of The Total Environment, 408(2), 431–438. https://doi.org/10.1016/j.scitotenv.2009.09.045

Mao, N., & Khalizov, A. (2021). Exchange reactions alter molecular speciation of gaseous oxidized mercury. ACS Earth and Space Chemistry, 5(8), 1842–1853. https://doi.org/10.1021/acsearthspacechem.1c00178

Marusczak, N., Sonke, J. E., Fu, X., & Jiskra, M. (2017). Tropospheric GOM at the Pic du Midi Observatory – Correcting bias in denuder based observations. Environmental Science & Technology, 51(2), 863–869. https://doi.org/10.1021/acs.est.6b04999

MATLAB. (2022). version 2022a. Natick, Massachusetts: The MathWorks Inc.

Microsoft Corporation. (2016). Microsoft Excel. Retrieved from https://office.microsoft.com/excel

Microsoft Corporation. (2016). Microsoft PowerPoint. Retrieved from https://www.microsoft.com/en-us/microsoft-365/powerpoint

Munthe, J., Wängberg, I., Pirrone, N., Iverfeldt, Å., Ferrara, R., Ebinghaus, R., Feng, X., Gårdfeldt, K., Keeler, G., Lanzillotta, E., Lindberg, S. E., Lu, J., Mamane, Y., Prestbo, E., Schmolke, S., Schroeder, W. H., Sommar, J., Sprovieri, F., Stevens, R. K., … Urba, A. (2001). Intercomparison of methods for sampling and analysis of atmospheric mercury species. Atmospheric Environment, 35(17), 3007–3017. https://doi.org/10.1016/S1352-2310(01)00104-2

Ogle, D.H., J.C. Doll, P. Wheeler, and A. Dinno. 2022. FSA: Fisheries stock analysis. R package version 0.9.3, https://github.com/fishR-Core-Team/FSA.

Outridge, P. M., Mason, R. P., Wang, F., Guerrero, S., & Heimbürger-Boavida, L. E. (2018). Updated global and oceanic mercury budgets for the United Nations Global Mercury Assessment 2018. Environmental Science & Technology, acs.est.8b01246. https://doi.org/10.1021/acs.est.8b01246

R Core Team (2022). R: A language and environment for statistical computing. R Foundation for Statistical Computing, Vienna, Austria. URL https://www.R-project.org/.

Sheu, G.-R., & Mason, R. P. (2001). An examination of methods for the measurements of reactive gaseous mercury in the atmosphere. Environmental Science & Technology, 35(6), 1209–1216. https://doi.org/10.1021/es001183s

Weiss-Penzias, P., Gustin, M. S., & Lyman, S. N. (2009). Observations of speciated atmospheric mercury at three sites in Nevada: Evidence for a free tropospheric source of reactive gaseous mercury. Journal of Geophysical Research, 114(D14), D14302. https://doi.org/10.1029/2008JD011607

Chapter 2 Supplemental Information

RMAS Principles & Sample Collection

The RMAS consisted of a 25.4 mm-thick bent, aluminum weather shield (Deluxe Welding, Reno, NV), mounted 1 meter above ground level, and housed six sample lines connected to vacuum pumps. KNF diaphragm pumps (UN838KNI) were initially used for the RMAS, but performed poorly, thus, a transition to using Welch piston vacuum pumps (2534B-01) occurred during this study. The pumps were housed inside the UNR greenhouse building to prevent wear on the pumps due to environmental conditions. Three of the six sample lines on each RMAS shield were connected to one vacuum pump via polyethylene Bev-a-line tubing. The six sample lines of the RMAS were connected to a perfluoroalkoxy alkane dual- or three-staged membrane cartridge (Savillex) containing two or three membranes 5 mm apart. Membrane cartridges were alternated by membrane type on the RMAS to prevent loss of all membrane sample replicates (2 of the same and 1 different sample per pump) and to minimize sampling bias based on their location on the RMAS.

Ambient air flow through each sample line was controlled by a critical flow orifice at 1 or 2 Lpm (Teledyne API, 941100 and 941700, respectively). The actual and standard (0 ^{o}C, 1 atm) flow rates were measured using a BGI tetraCal Air Flow Calibrator at the beginning and end of each RMAS deployment that were used to determine the volume of air sampled during the deployment. The change in the flow rate for each membrane sample, from the beginning to the end of each experiment deployment was summarized (mean, median, standard deviation): 1) Flow Rate Variation Experiment – 1 Lpm: 0.026, 0.015, 0.040 and 2 Lpm: 0.044, 0.027, 0.054; 2) Alternate Membrane

Comparisons – Alternate CEM Comparison: 0.027, 0.021, 0.028; Alternate Nylon Membrane Comparison: 0.038, 0.025, 0.065; Alternate PTFE Membrane Comparison: 0.036, 0.031, 0.031; and Membrane Cartridge Sorption Experiment: 0.010, 0.078, 0.078.

To collect the RMAS membranes, first, RMAS pumps were turned off to prevent line contamination. Then, the membrane cartridges were removed from the RMAS and brought to a clean working area where membrane cartridges were disassembled. Each membrane sample was placed into a new sterile 50 mL conical polypropylene tube with a polyethylene cap (SPL Life Sciences, 50050) using PTFE-wrapped (TaegaSeal) forceps that were re-wrapped for every upstream or downstream layer of membrane samples. The samples were grouped together by their upstream or downstream orientation in the membrane cartridge and doubled-bagged in resealable plastic bags. Triplicate blank membranes were taken at the start of the deployment using freshly PTFE-wrapped forceps and placed into polypropylene tubes that were bagged separately. All samples were immediately stored in a -20 ºC freezer until analysis. Membrane samples were analyzed within 1.5 months of collection; Dunham-Cheatham et al. (2020) showed that RM measurements taken by RMAS CEM and nylon membranes were the same for up to 190 days of storage.

Membrane Analyses

Total Mercury Analysis using a Tekran 2600-IVS

The measurement of total Hg using the Tekran 2600-IVS began with a chemical digestion procedure in the membrane collection tube to convert all RM to GEM, following EPA Method 1631 Revision E (U.S. EPA, 2002). The chemical digestion started with preservation of the sample by the addition of 50 mL of 1% hydrochloric acid

(HCl; Fisher Scientific, A466-1; Optima grade), prepared with Type 1 water, followed by the addition of 3 mL of bromine monochloride (BrCl; 1.8% potassium bromide (KBr) and 1.2% potassium bromate ($KBrO_3$) to oxidize all Hg(0) to Hg(II) in solution. The sample solution was left for a minimum of 12 hours (samples were always left overnight) to ensure all membrane RM was oxidized in the solution. After the 12-hour holding, 0.75 mL of an argon-sparged 30% hydroxylamine hydrochloride (ClH_4NO) solution was added to each sample to quench the excess BrCl. Each digestate was weighed into a 40 mL VOA glass vial with septum cap (Industrial Glassware) and 0.25 mL of 20% stannous chloride ($SnCl_2$) in 10% Optima HCl was quickly added to each vial before being capped and placed on the Tekran 2600-IVS; the $SnCl_2$ acted to reduce the aqueous RM into volatile GEM. The Tekran 2600-IVS sparged the GEM in each sample onto gold-coated sand traps, thermally desorbed the Hg from the traps at 550 °C, and quantified the GEM by cold vapor atomic fluorescence spectrometry. An ultraviolet lamp inside of the Tekran 2600-IVS induced Hg fluorescence by the emission of wavelengths of light at 253.7 nm and the fluoresced photons in the sample were measured and amplified using a photomultiplier tube. The amount of GEM in each sample was quantified using the voltage signal generated when the fluoresced photons impacted the Tekran 2600-IVS detector.

To ensure stringent quality control methods (QA/QC) of the Hg analysis, a five-point calibration curve (points at 1, 5, 10, 25, and 100 parts per trillion) was used to calibrate the instrument every 30 samples, and an r^2 value of at least 0.999 was required for every curve to pass QA/QC. Calibration was required due to the inherent variability of the Tekran 2600-IVS lamp intensity and detector sensitivity over time. For every

twelve samples analyzed, either a 5 or 10 ng L^{-1} ongoing precision recovery standard was analyzed to ensure that the instrument was measuring 10% or less deviation from the expected value based on the calibration. Replicate method blanks (n = 8+ per analysis) containing all reagents were analyzed to establish a baseline concentration of Hg that was subtracted from each standard and sample.

To determine the Hg content on the membranes prior to sampling, triplicate membrane blanks were collected at the start of each sampling deployment for each membrane type. The membrane blanks were stored at -20 ºC during the sampling deployment and were analyzed with the corresponding RMAS samples. The mean blank Hg content for each membrane type was: 1) CEM: 0.034 ± 0.029 ng Hg (n = 141); 2) Sterlitech PES: 0.035 ± 0.017 ng Hg (n = 39); 3) Cole-Palmer PES: 0.012 ± 0.0072 ng Hg (n = 15); 4) Sartorius (0.2 μm): 0.011 ± 0.0087 ng Hg (n = 222); 5) Sterlitech (0.2 μm): 0.023 ± 0.012 ng Hg (n = 57); (6) Sterlitech (0.8 μm): 0.020 ± 0.0072 ng Hg (n = 15); 7) Whatman (0.2 μm): 0.013 ± 0.0067 ng Hg (n = 33); 8) Whatman (0.8 μm): 0.012 ± 0.0070 ng Hg (n = 33); 9) PTFE: 0.0044 ± 0.0035 ng Hg (n = 30); 10) VWR glass fiber: 0.039 ± 0.011 ng Hg (n = 30); and 11) Whatman glass microfiber: 0.016 ± 0.022 ng Hg (n = 30).

Thermal Desorption of Upstream Nylon Membranes

The thermal desorption method, as described by Dunham-Cheatham et al. (2023) and Huang et al. (2013), began by placing a nylon membrane into a tube furnace (Lindberg Blue Tube Furnace, TF55035A-1), and the membrane was ramp heated from 50 °C to 200 °C at a rate of 2 °C min^{-1}, with a 5-minute hold period at 200 °C. As the temperature increased, RM species desorbed and entered a Hg-free, zero-air flow at 1

Lpm, controlled by the pump of a Tekran 2537A Mercury Analyzer. Following emission from the membrane, the sample air passed through a 450 °C pyrolyzer to reduce all RM compounds to Hg(0). Following reduction, the sample was pulled into the Tekran 2537A for quantification every 2.5 minutes. Then, peak release temperatures were identified and compared to standard desorption profiles developed from the permeation of gaseous Hg of solid standard Hg(II) compounds onto nylon membranes (e.g., HgO, $HgBr_2$, $HgCl_2$, $HgN_2O_6 \cdot H2O$, and $HgSO_4$, and wet-applied methylmercury (MeHg)). The peak release temperature ranges used for each Hg(II) compound, based on the Hg standards, were: 82.5 – 92.5 °C for [-O]; 95 – 115 °C for [-Br/Cl]; 117.5 – 127.5 °C for [-N]; 130 – 147.5 °C for [-S]; and 150 – 190 °C for MeHg or organic-bound compounds. All tested nylon membrane thermal desorption ranges used during the study are listed in Table SI 3. The peak release temperatures were used to deconvolute pulses of desorbed membrane RM using a computer software (MATLAB R2022a, curve fitting function), assuming the peak shape to be Gaussian. The area of the integral of each desorption peak (i.e., peak area), in °C ng m^{-3}, was obtained and converted to pg RM m^{-3}.

The Tekran 2537A was calibrated every week using the instrument's internal calibration source. The tube furnace temperatures were calibrated approximately every six months and they did not deviate more than 8% over 3 years of calibration. The mean coefficient of determination (r^2) and model error (%) for the Sartorius nylon membrane thermal desorption models was $r^2 = 0.99 \pm 0.004$ and % error = 1.75 ± 0.8 (n = 19).

Regression Analyses in RStudio

Reduced major axis regression and Spearman correlation results were obtained from RStudio using the following code under R version 4.2.1:

```
install.packages('lmodel2') # install package
library(lmodel2) # load package

data <- "testdata.csv"
testdata <- read.csv(data) # upload data

# RMA regression
# Format: lm(tested (response) variable+0 ~ historical (predictor) variable)
mod1 <- lm(y+0 ~ x)
mod1.summary <- summary(mod1)
layout(matrix(1:4,nrow=2,byrow=T))
plot(mod1)
mod1.residuals <- mod1$residuals
hist(mod1.residuals)
70ruskal.test(mod1.residuals)
confint(mod1)

# Spearman correlation
cor.test(x = data, y = data, method = 'Spearman')
```

Chapter 2 Supplemental Information Tables and Figures

Material	Membrane Pore Size/Diameter	Brand	P/N (part number)
Cation-exchange membrane	0.8 micron/cut to 47 mm	Pall	S80570
Polyamid (nylon)	0.2 micron/47 mm	Sartorius	2500747N
PolyTetraFluoroEthylene (PTFE)	0.2 micron/47 mm	Sartorius	1180747N
Polyethersulfone (PES)	0.8 micron/47 mm	Sterlitech	PES0847100
Polyethersulfone (PES)	0.45 micron/90 mm cut to 47 mm	Cole-Palmer	361-3811-CP
Polyamide (nylon)	0.2 micron/47 mm	Sterlitech	NY0247100
Polyamide (nylon)	0.2 micron/47 mm	Whatman	7402-004
Polyamide (nylon)	0.8 micron/47 mm	Whatman	7408-004
Polyamide (nylon)	0.2 micron/47 mm	Sterlitech	NY0247100
Polyamide (nylon)	0.8 micron/47 mm	Sterlitech	NY0847100
Glass fiber	1.2 micron/47 mm	VWR	28333-139
Glass fiber	1.5 micron/47 mm	Whatman	3827-047

Table S1. Table displaying detailed information on all membranes used in this study.

Experiment	Dates	Precipitation (mm)	Wind Speed (m s^{-1})	Temperature (°C)	Max. Gust Speed (m/s)	RH* (%)	Solar radiation (W m^{-2})
Flow Rate Variation	05/25/2021 - 09/07/2021	7.37	1.89 ± 1.60	24.54 ± 7.42	3.91 ± 2.94	27.73 ± 14.56	314.92 ± 368.67
Flow Rate Variation	12/07/2021 - 02/22/2022	77.47	1.68 ± 1.53	2.07 ± 5.53	3.18 ± 2.80	67.21 ± 21.43	117.64 ± 185.35
Flow Rate Variation	11/17/2022 - 12/22/2022	43.69	1.49 ± 1.23	0.66 ± 4.89	2.81 ± 2.33	69.74 ± 19.31	102.65 ± 164.65
Alternate CEM	11/17/2022 - 12/22/2022	43.69	1.49 ± 1.23	0.66 ± 4.89	2.81 ± 2.33	69.74 ± 19.31	102.65 ± 164.65
Alternate CEM	09/07/2021 - 11/02/2021	88.14	1.85 ± 1.50	14.36 ± 8.05	3.61 ± 2.76	45.48 ± 22.71	191.09 ± 273.05
Alternate Nylon	09/07/2021 - 11/02/2021	88.14	1.85 ± 1.50	14.36 ± 8.05	3.61 ± 2.76	45.48 ± 22.71	191.09 ± 273.05
Alternate Nylon	05/10/2022 - 06/21/2022	0.25	2.55 ± 1.80	17.16 ± 7.04	4.99 ± 3.26	34.66 ± 16.02	290.61 ± 333.47
Alternate Nylon	08/02/2022 - 09/06/2022	21.34	1.69 ± 1.23	25.31 ± 6.62	3.40 ± 2.39	35.17 ± 20.93	290.61 ± 352.19
Alternate PTFE	09/06/2022 - 11/17/2022	18.04	1.47 ± 1.28	12.79 ± 9.45	2.95 ± 2.46	47.37 ± 23.23	185.20 ± 262.21
Membrane Cartridge Sorption	06/27/2022 - 07/26/2022	0	2.18 ± 1.75	24.97 ± 6.76	4.52 ± 3.26	27.73 ± 14.32	348.79 ± 379.21

* RH is relative humidity.

Table S2. Averaged meteorologic parameters (± 1σ) by RMAS experiment deployment. The date code used here is: MM/DD/YYYY.

Date	Hg(II)	SAR2	STER2	Date	SAR2	STER2	WHAT2	WHAT8	Date	SAR2	STER2	STER8	WHAT2	WHAT8
09/14/21	Oxygen	89	87	**05/17/22**	84.5	88	78	72.5	**08/09/22**	86.5	85.5	86	90	91
	Halides	109	107.5		106	103.5	105.5	97.5		106	106	107	105	109
	Nitrogen	122.5	123.5		123	125	123.5	120		120	118.5	120	123.5	130
	Sulfur	150	150.5		146	150	150	144		145	142	144	146	154
	Organic	182.5	180.5		180	180	182	174		178.5	175	176	176	179.5
09/21/21	O	85	87.5	**05/24/22**	82	96.5	78	72	**08/16/22**	86	92.5	85.5	83.5	76
	Br/Cl	107.5	106.5		107	127.5	102	98		108	107.5	103	109	110
	N	122.5	123		122	154.5	124	119		122	127.5	117	123.5	131.5
	S	147	150		146.5	171.5	159	148		144	144	146	150	153.5
	Org	184	181.5		180	185	184	180		177	173.5	176	180.5	180
09/28/21	O	85.5	86.5	**05/31/22**	85	100.5	79	72.5	**08/23/22**	89	85.5	86	82.5	79.5
	Br/Cl	106.5	105		105	131	102.5	97.5		107.5	104.5	105	100	104
	N	121.5	119		122	148	121	118		122	117.5	119	126.5	131.5
	S	146	150		146	170	152.5	148		146	143	147.5	149	154.5
	Org	183.5	180		178	185	182.5	181.5		175	174	176	177.5	180
10/05/21	O	82.5	89	**06/07/22**	85	99	80.5	74.5	**08/30/22**	88.5	85	87	81	76.5
	Br/Cl	106.5	106.5		108	127	104.5	99.5		110	104	104	97	104
	N	120	121.5		121.5	142.5	122	113.5		121.5	115	117	120.5	124
	S	143	150		146	165	150	146		145.5	139	146	148	150
	Org	180.5	179.5		180.5	184	181.5	180.5		178.5	172.5	174.5	175.5	180
10/12/21	O	86.5	87	**06/14/22**	86	88	81.5	75.5	**09/06/22**	88.5	86	90	85	78
	Br/Cl	105.5	105		106	103.5	103.5	95		110	104	106.5	109	104
	N	122.5	121.5		123	127	121.5	112		125	115	119	127	124
	S	147	150		147	150	150	144		146.5	141	147	150	150
	Org	185	181.5		182.5	180.5	181.5	180		177.5	172	176	180	181
10/19/21	O	82	91	**06/21/22**	83.5	89	79	74.5						
	Br/Cl	102.5	105.5		107	101	103	98.5						
	N	0	0		122	123	123	113.5						
	S	150	145		147	148	152	147.5						
	Org	184	180		180	181.5	181	180.5						
10/26/21	O	89	87											
	Br/Cl	109	107.5											
	N	122.5	123.5											
	S	150	150.5											
	Org	182.5	180.5											
11/02/21	O	84.5	87.5											
	Br/Cl	107.5	106.5											
	N	124.5	123											
	S	146	150											
	Org	180	181.5											

Table S3. Table listing the desorption temperatures used for each reactive mercury compound by sampling deployment and nylon membrane. The desorption temperatures are listed in order, by compound, from the top: oxygen, halide (bromine and chlorine), nitrogen, sulfur, and organic reactive mercury compounds. The membranes are abbreviated here: SAR2 indicates the Sartorius (0.2 μm); STER2 is Sterlitech (0.2 μm); STER8 is Sterlitech (0.8 μm); WHAT2 is Whatman (0.2 μm) membrane; and WHAT8 is Whatman (0.8 μm) membrane. The dates represent the collection date (MM/DD/YYYY).

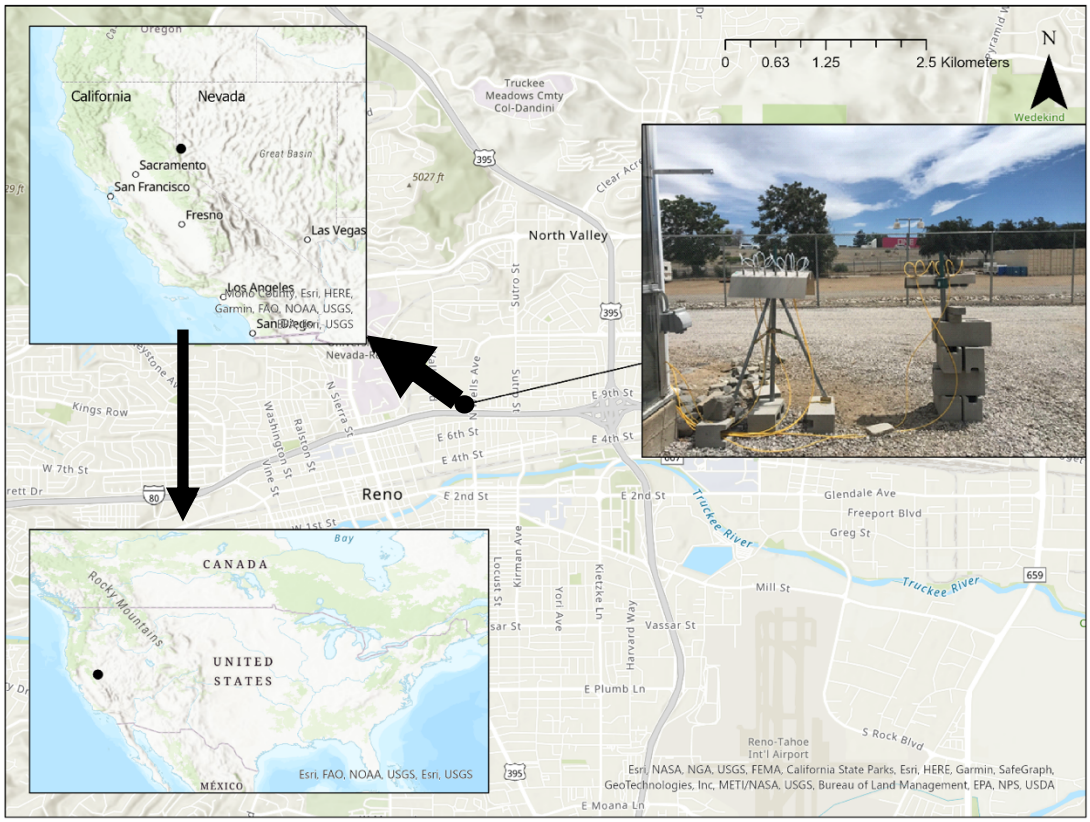

Figure S1. Map displaying the location of the Greenhouse sampling location in Reno, NV, with an image during sampling, note the red tractor-trailer in the background to represent the proximity of the sampling location to I-80.

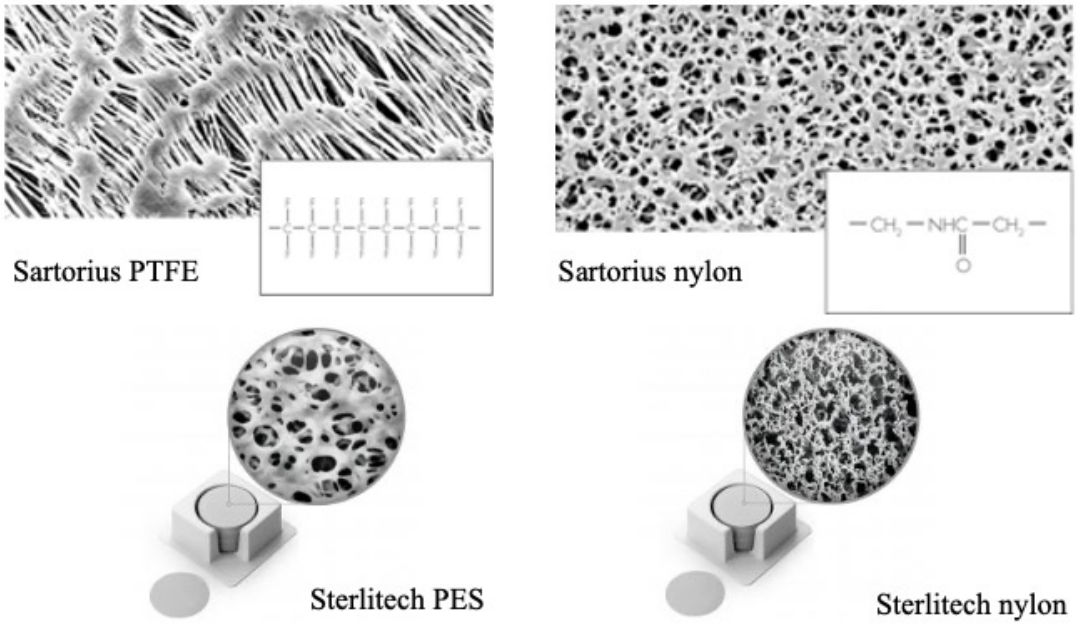

Figure S2. Electron microscope images of the Sartorius PTFE and nylon membranes, and Sterlitech PES and nylon membranes.

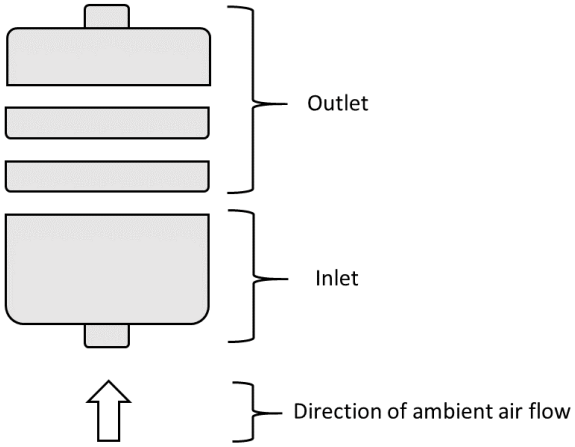

Figure S3. Depiction of the Reactive Mercury Active System membrane cartridge, separated by the inlet and outlet pieces. The inlet piece represented the end of the membrane cartridge exposed to ambient air, before encountering the collection surfaces, and the outlet piece was representative of the stages the membranes rest on and the connection of the cartridge to the larger system.

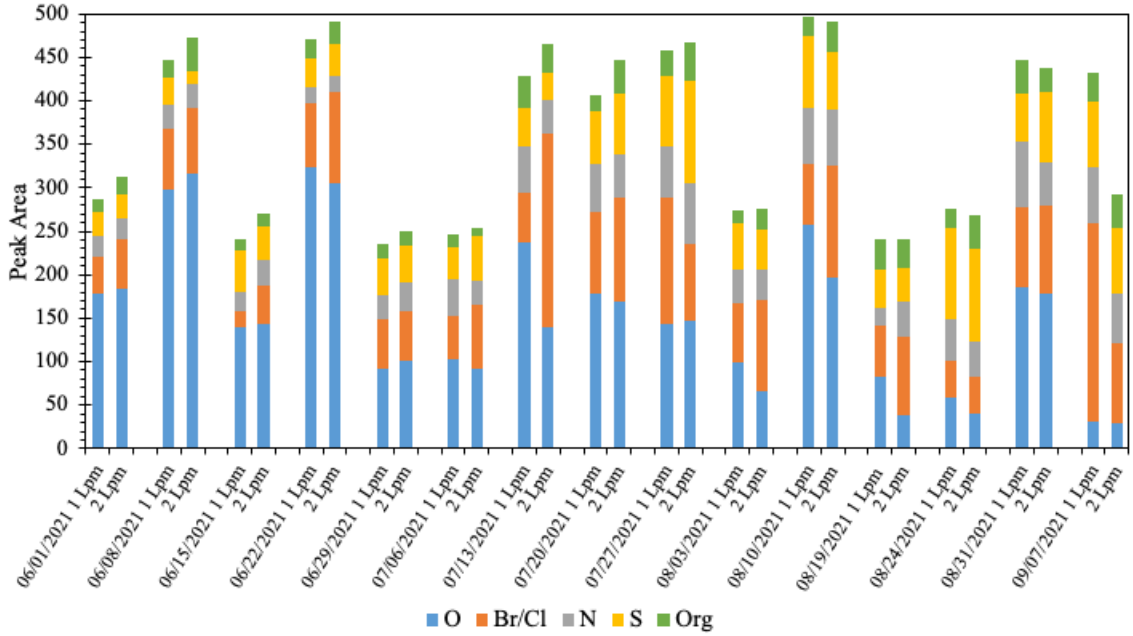

Figure S4. The peak area (pg RM m^{-3}) of the reactive mercury compounds thermally desorbed from the Sartorius (0.2 µm) nylon membrane by sampling deployment from May 25 to September 7, 2021 (summer 2021). For each deployment date, the left bar represents the results at 1 Lpm and on the right, 2 Lpm. The dates represent the collection date (MM/DD/YYYY).

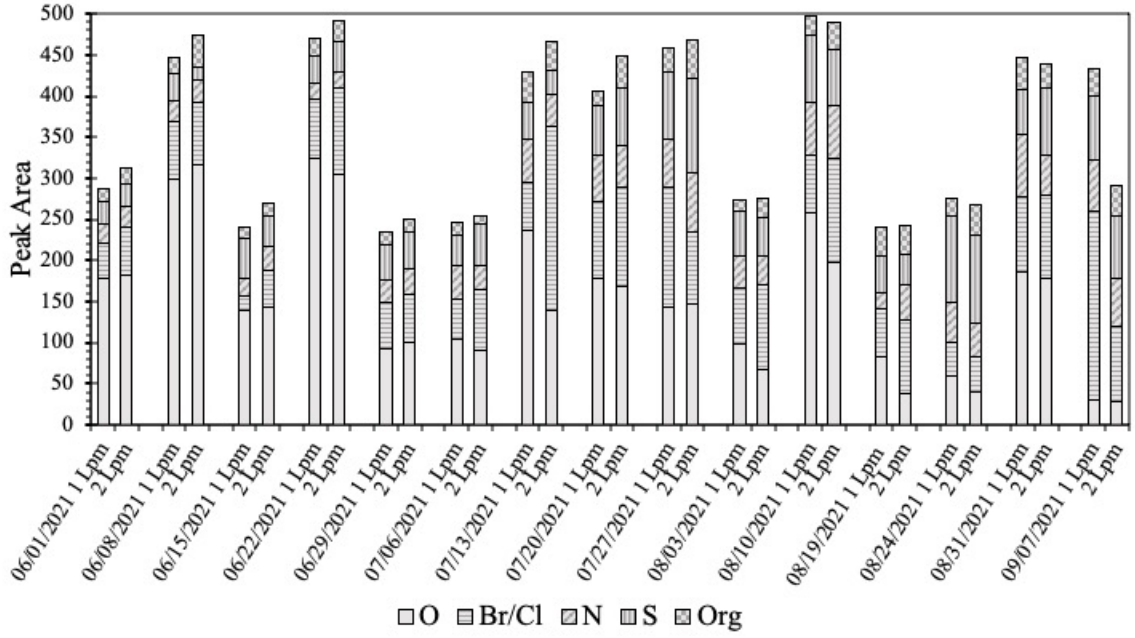

Figure S5. The peak area (pg RM m^{-3}) of the reactive mercury compounds thermally desorbed from the Sartorius (0.2 μm) nylon membrane by sampling deployment from May 25 to September 7, 2021 (summer 2021). For each deployment date, the left bar represents the results at 1 Lpm and on the right, 2 Lpm. The dates represent the collection date (MM/DD/YYYY).

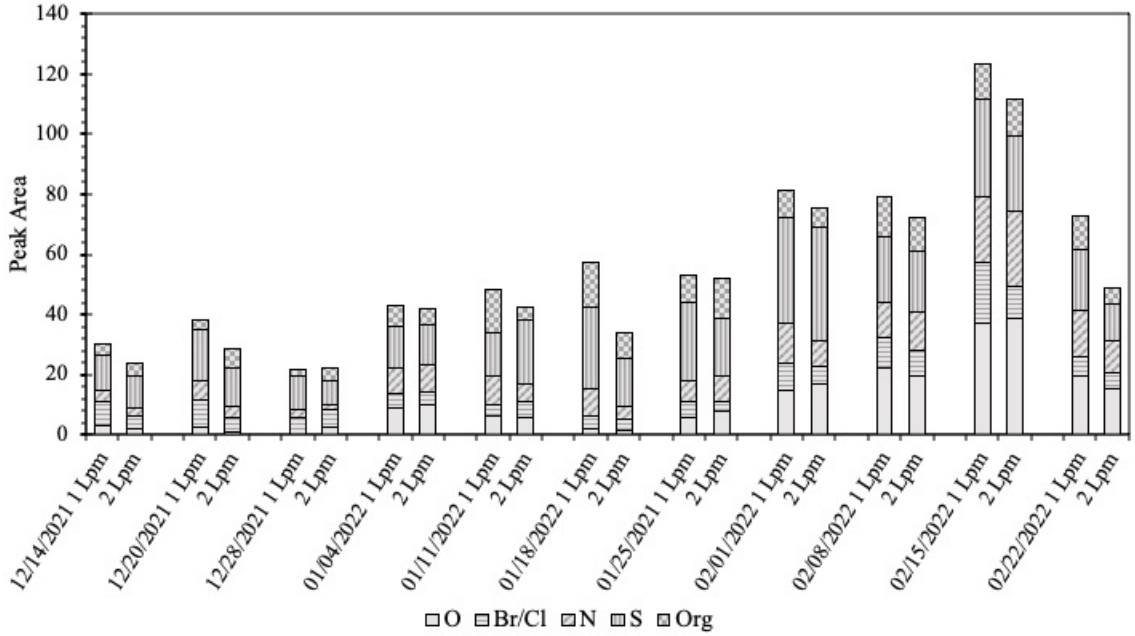

Figure S6. The peak area (pg RM m^{-3}) of the oxidized mercury compounds thermally desorbed from the Sartorius (0.2 μm) nylon membrane by sampling deployment from December 7, 2021, to February 22, 2022 (winter 2021). For each deployment date, the left bar represents the results at 1 Lpm and on the right, 2 Lpm. The dates represent the collection date (MM/DD/YYYY).

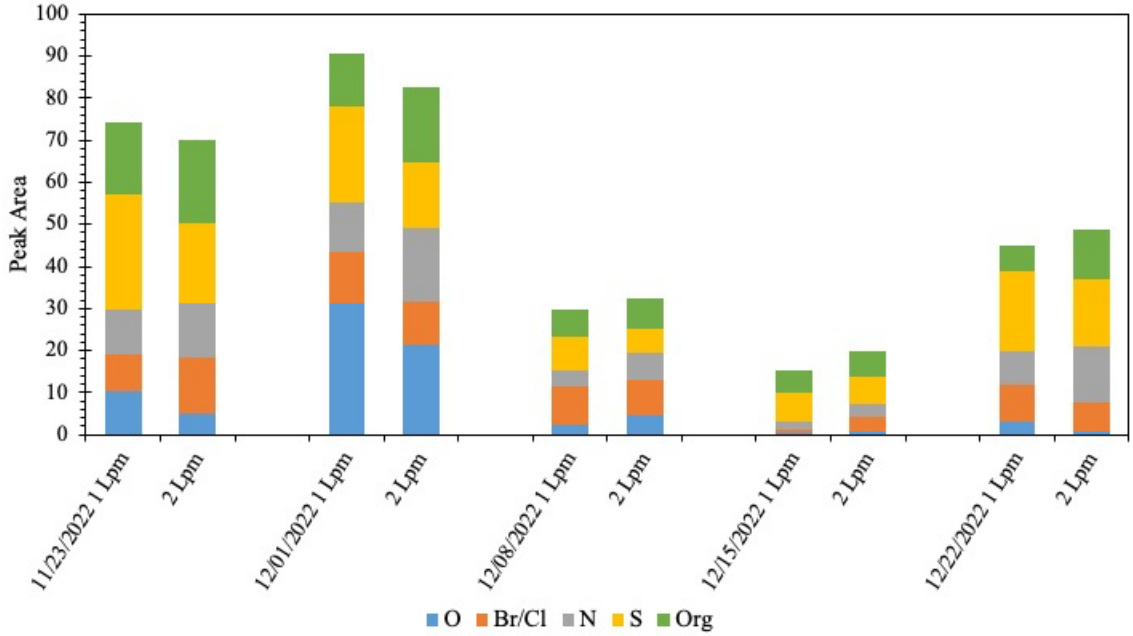

Figure S7. The peak area (pg RM m^{-3}) of reactive mercury compounds thermally desorbed from the Sartorius (0.2 µm) nylon membrane from November 17 to December 22, 2022 (winter 2022). For each deployment date, the left bar represents the results at 1 Lpm and on the right, 2 Lpm. The dates represent the collection date (MM/DD/YYYY).

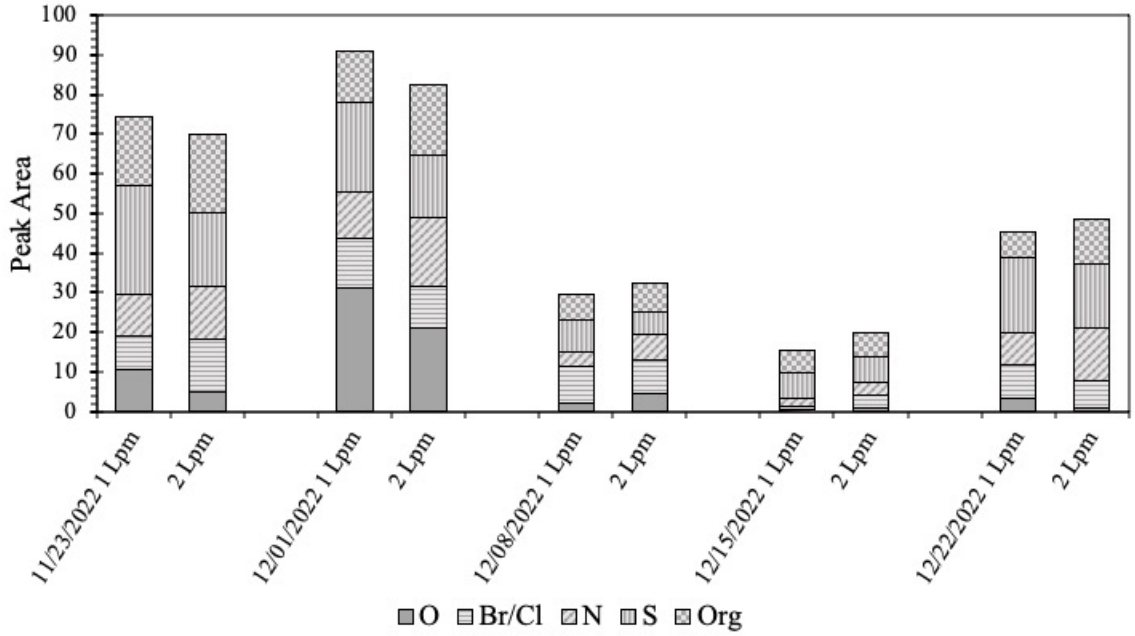

Figure S8. The peak area (pg RM m^{-3}) of reactive mercury compounds thermally desorbed from the Sartorius (0.2 μm) nylon membrane from November 17 to December 22, 2022 (winter 2022). For each deployment date, the left bar represents the results at 1 Lpm and on the right, 2 Lpm. The dates represent the collection date (MM/DD/YYYY).

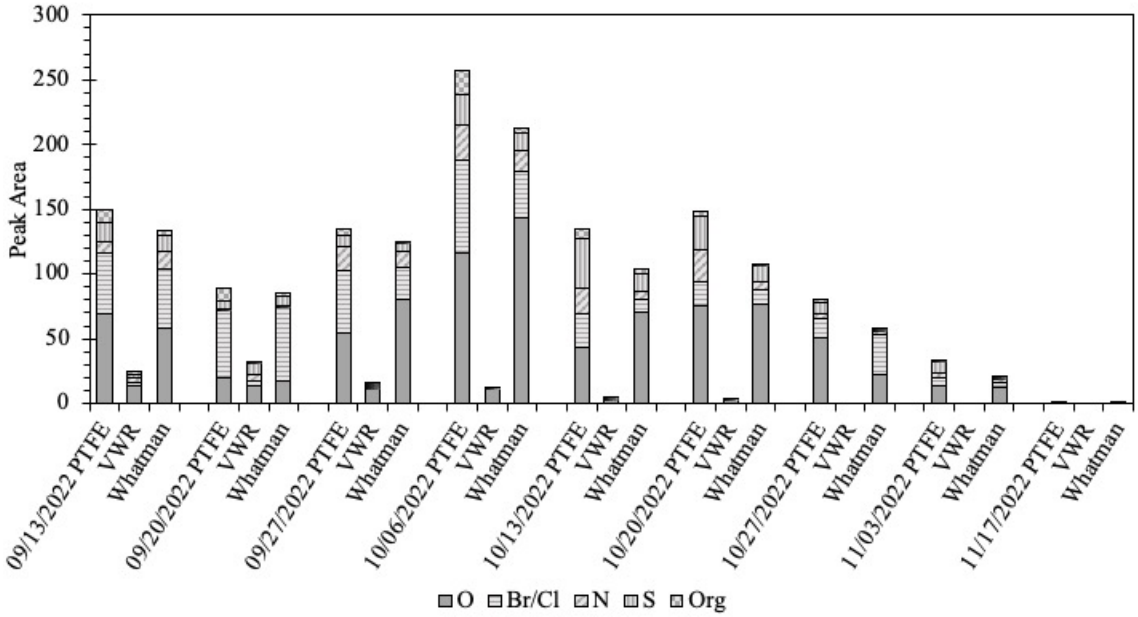

Figure S9. The peak area (pg GOM m^{-3}) of the oxidized mercury compounds thermally desorbed from the Sartorius PTFE, and alternate VWR and Whatman downstream nylon membranes from September 13 to November 17, 2022 (fall 2022). The dates represent the collection date (MM/DD/YYYY).

Chapter 2 Supplemental Information References

Dunham-Cheatham, S. M., Lyman, S., & Gustin, M. S. (2023). Comparison and calibration of methods for ambient reactive mercury quantification. Science of The Total Environment, 856, 159219. https://doi.org/10.1016/j.scitotenv.2022.159219

Dunham-Cheatham, S. M., Lyman, S., & Gustin, M. S. (2020). Evaluation of sorption surface materials for reactive mercury compounds. Atmospheric Environment, 242, 117836. https://doi.org/10.1016/j.atmosenv.2020.117836

United States Environmental Protection Agency (U.S. EPA). (2002). Method 1631, Revision E: Mercury in water by oxidation, purge and trap, and cold vapor atomic fluorescence spectrometry, p. 45. U.S. EPA Washington, DC.

Huang, J., Miller, M. B., Weiss-Penzias, P., & Gustin, M. S. (2013). Comparison of gaseous oxidized Hg measured by KCl-coated denuders, and nylon and cation exchange membranes. Environmental Science & Technology, 47(13), 7307–7316. https://doi.org/10.1021/es4012349

MATLAB. (2022). version 7.10.0 (R2022a). Natick, Massachusetts: The MathWorks Inc.

R Core Team (2022). R: A language and environment for statistical computing. R Foundation for Statistical Computing, Vienna, Austria. URL https://www.R-project.org/

Chapter 3: Contributions to Atmospheric Reactive Mercury Research Studies

This chapter sequentially presents the contributions that I made to two manuscripts that are in preparation for submission to peer-reviewed journals:

1. Observations of the chemistry and concentrations of reactive Hg at locations with different ambient air chemistry. Mae Sexauer Gustin, Natalie R. Allen, Sarrah M. Dunham-Cheatham, Nicole Choma, Seth Lyman, William Johnson, Sam Lopez, Armistead Russell, Eric Mei, Olivier Magand, Aurelien Dommergue
2. Determining sources of reactive mercury compounds in Reno, Nevada, USA. Mae Sexauer Gustin, Sarrah M. Dunham-Cheatham, Nicole Choma, Kevin Shoemaker, Natalie R. Allen

The first manuscript presents information that will help to better understand the behavior and sources of reactive mercury (RM) using the University of Nevada, Reno – Reactive Mercury Active System (RMAS) that was deployed at sampling locations with different ambient air chemistry from 2021-2023. Sampling locations included: 1) Amsterdam Island, Indian Ocean; 2) Atlanta, GA; 3) Guadalupe Mountains, TX; and 4) Great Salt Lake, UT. A description of all sampling sites is included in Chapter 1. All RMAS samples were deployed with the help from site operators and co-authors. Overall, my responsibilities for this manuscript were to coordinate sampling logistics with site operators, receive and analyze site samples, process mercury (Hg) sample data, compile site data, and provide overall project data management.

Communication with site operators was partially my responsibility and included: notification to operators that sample collection was incorrectly performed; coordination of shipments containing refill supplies to sampling sites and RMAS samples back to

UNR for analysis; operator notification of the switch to a different site operator (five times); and the coordination of ending sampling altogether. It was important to maintain friendly and frequent communication with site collaborators to ensure samples were collected accurately and received on time.

Approximately every month, samples were shipped from sites to UNR. When site samples arrived, I took inventory of the samples ensuring that the number of samples and that the labeling scheme was accurate. Then, I would perform a visual check of all samples to ensure that upstream membranes contained visible atmospheric debris and that the downstream membrane(s) was less dirty; a frequent occurrence was that membrane cartridges were installed upside down so, the downstream membrane became the upstream membrane. It was necessary to characterize all sample discrepancies prior to analysis, because the membranes were analyzed by two different methods. For each sampling site, a detailed inventory spreadsheet was maintained and included: the RMAS configuration(s) deployed; sampling start and end times; external factors that may have impacted samples; membrane sample RM concentrations; and other sample information (i.e., membrane lot numbers, etc.) (Figure 1). Overall, managing RMAS samples from sampling sites required attention to detail and a complete understanding of the RMAS sampling procedure to notice discrepancies and ensure minimal sample losses.

Once RMAS samples were received and recorded, I was responsible for planning and performing analyses of the samples. The procedure to analyze samples was described in detail in Chapter 2. Briefly, sample analysis involved a chemical digestion and subsequent detection of Hg by cold vapor atomic fluorescence spectrometry (CVAFS) using a Tekran 2600-IVS (Tekran 2600) for all cation exchange membranes (CEM),

polytetrafluoroethylene (PTFE), and downstream nylon membranes (U.S. EPA, 2002). Upstream nylon membranes were analyzed by thermal desorption (Dunham-Cheatham et al., 2023). All sites sampled for about twenty weeks and deployed both a RMAS and RMAS+P, a configuration of the RMAS designed to separately measure particulate-bound mercury (PBM) and gaseous oxidized mercury (GOM), except for the Amsterdam Island and Guadalupe Mountains sites that only deployed a RMAS. In total, I analyzed approximately sixty weeks of site samples that consisted of twenty or forty samples per week. Amsterdam Island samples were analyzed by Dr. Sarrah Dunham-Cheatham. Sample analysis was required about one to two times per week, year-round, to keep up with the influx of samples from all sampling sites. The amount of site samples became overwhelming in spring 2022, and Jordin Jacobs M.S. was hired to assist with sample analysis. I trained and supervised Jordin's work, which helped to manage the sample inventory.

The Tekran 2600 measured membrane sample concentrations of total Hg using CVAFS by inducing the fluorescence of Hg present in the sample via an ultraviolet (UV) light. This works because Hg possesses the physical property to become excited with exposure to UV light at a wavelength of 253.7 nm. Following excitement, fluorescence occurred and was the Hg molecule emitting photons of light as it returned to the ground state. The emitted photons were amplified by a photomultiplier tube (PMT) and passed to the detector, where the resulting voltage was measured and used to calculate the amount of total Hg in the sample. However, this method to detect total Hg was not an absolute quantification method in that, individual Hg atoms were not being counted. The measurement of Hg given by the Tekran 2600 was calculated from the voltage signal

generated when the fluoresced Hg photons in the sample impacted the PMT. The voltage signal was partially dependent on the intensity of the UV lamp source, meaning a higher intensity would increase fluorescence. The voltage signal was also dependent on the sensitivity of the PMT; a lower intensity would decrease the voltage signal. Because the intensity of the UV lamp and the sensitivity of the PMT would vary with time, the instrument was calibrated before and during each sample analysis. The calibration for the Tekran 2600 included preparing several multiple-point standard curves, prepared from a Hg certified reference material (Ricca 1000 parts per trillion Hg standard; PHG1KN100) at concentrations of 1, 5, 10, 25, and 100 pg L^{-1} (ppt). Each individual standard provided a reference point that characterized a quantity of Hg to a specific PMT voltage signal. A linear calibration curve, with a coefficient of determination (r^2) value of at least 0.999 was necessary to achieve for each curve during sample analysis. The Tekran 2600 analysis also required stringent protocols that included running a 5 or 10 ppt standard for at least every ten samples, with the standard concentration measuring 10% or less deviation from the expected value determined by the calibration. These calibration standards were made to check the 5 and 10 ppt Hg points of the calibration curve, because this was the range of the curve that most RMAS sample concentrations were detected. Other sample analysis checks included preparing duplicate samples and checking the order in which samples were analyzed.

Once samples were analyzed, I was responsible for processing all Hg data. The Hg data were processed using a spreadsheet to convert the Tekran 2600 outputs to concentrations of Hg in pg m^3 of air (Figure 2). To convert the Tekran 2600 outputs, or the PMT voltages determined by the sample fluorescence peak, to concentrations, the

background Hg was first subtracted from the Tekran 2600 outputs. The background Hg consisted of a control containing all analysis reagents (reagent blank or calibration blank). Then, the slope of the calibration curve was multiplied by the blank-corrected value to get the total concentration of Hg in the sample in ng L^{-1}. The sample acid dilution was accounted for by dividing the ng L^{-1} sample concentration by the dilution factor, which was the volume of digestate (0.02475 L) divided by the total volume of the sample tube (0.025 L). Then, the volume of the added reagents (i.e., hydrochloric acid (0.05 L); bromine monochloride (0.003 L); stannous chloride (0.00025 L); and hydroxylamine hydrochloride (0.00075 L); total = 0.05375 L) was multiplied by the concentration in ng L^{-1} to cancel out the volume term (L) and left the total mass of Hg in ng. From here, the value was converted to a Hg concentration in an atmospheric volume (m^3) by dividing by the volume of air that passed through the RMAS during the sampling deployment. Following conversion of membrane sample outputs to concentrations in pg m^{-3}, the data were compiled into a spreadsheet for each sampling site. These summary spreadsheets were prepared to designate one spot for containment of all information necessary to include in the manuscript. Apart from RMAS membrane concentrations, these summary spreadsheets included nylon membrane chemistry data and all ancillary data (mean meteorological and air chemistry parameters) (Figure 3).

For this manuscript, I was also responsible for compiling all ancillary data for the Guadalupe Mountains and Great Salt Lake sampling sites. The ancillary data for the Atlanta and Amsterdam Island sites was prepared by Eric Mei and Olivier Magand, respectively. Ancillary data comprised meteorological and air chemistry parameters listed in Table 1 (i.e., criteria air pollutants).

Mostly, the ancillary data were downloaded as a text or CSV file using the internet or using an integrated development environment (i.e., Thonny (Annamaa, 2015)) to extract the data from the internet. Ancillary data downloads were uploaded into a spreadsheet, where I calculated the mean and standard deviation of each ancillary data parameter during each RMAS sampling deployment (Figure 4).

For the Guadalupe Mountains site, the ancillary data monitors were sparse. Therefore, it was necessary to identify alternate ancillary data sources in the area and compare the same parameter measurements at one source, located near the RMAS, to other sources further away. For example, ozone measurements were regressed, using Microsoft Excel, from two different monitors to determine whether the measurements were similar and if so, it was accurate to interpret ancillary data from a broader area surrounding the Guadalupe Mountains site (Figure 5). The opposite occurred at the Great Salt Lake site, where ancillary data sources were abundant near the location of the RMAS but parameter availability varied by source. Similar for the Guadalupe Mountains site, the same ancillary parameters were regressed between different Great Salt Lake site ancillary data sources to determine whether ancillary data from the area could be interchanged.

For the second manuscript, the concentrations and chemistry of RM in Reno, NV were measured using the RMAS and RMAS+P at a low and high elevation sampling site to assess the behavior and sources of RM in Reno. The low elevation site was located at the UNR Greenhouse Complex (39.5373967, -119.8048547, 1367 masl) and the high elevation site was located at Peavine Peak (39.589389, -119.928797, 2513 masl), approximately 12 km from the Greenhouse. This study was unique because it looked at the differences between RM behavior and sources based on elevation. Also, the two

sampling sites were a part of a previous sampling campaign, thus the comparison between present (2022) and past data (2019 and 2020) was also performed. Overall, my responsibilities for this manuscript were to collect and analyze site samples, process, and compile the Hg sample and site ancillary data, and to provide overall project data management.

In addition to analysis and management of RMAS sample data, I was responsible for weekly RMAS sample collections. Weekly site sample collections occurred at the Greenhouse and Peavine sampling sites from September 22 to November 3, 2022. These weekly sampling trips occurred on the same day as the Greenhouse samplings. Typically, Dr. Sarrah Dunham-Cheatham or a helper and I would drive to the peak of Peavine, collect the samples, and drive back down; then, the Greenhouse site sample collection would occur. The entire sampling day lasting from 8 am to 2 pm. Figure 6 represents what a sample collection looked like.

Sample analysis for this manuscript was performed using the Tekran 2600 and thermal desorption as previously discussed for the first manuscript. Weekly RMAS sample analyses using the Tekran 2600 were routinely performed for the duration of site sampling. In addition, the thermal desorption method for the upstream nylon membranes allowed for the analysis of about four samples a day, and therefore required constant analysis to ensure the inventory of samples did not become too large. Following sample analysis, all Hg data were converted to concentrations of RM in pg m^{-3}, and ultimately, concentration data were compiled into one summary spreadsheet for the Greenhouse and Peavine sampling sites.

Also, for this manuscript, I deconvoluted the thermal desorption peaks of the upstream nylon membrane samples to determine RM chemistry (Figure 7). The deconvolution analysis is detailed in Chapter 2 of this thesis (Supplemental Information). Briefly, I used MATLAB (vR2022a) to deconvolute and separate the individual thermal desorption peaks of each RM compound present on a nylon membrane. The goal of the deconvolution was to manipulate the Hg desorption temperature values until the highest r^2 and lowest model percent error were achieved. This data ended up in the final summary spreadsheet.

Lastly, for this manuscript I was responsible for compiling all ancillary data (Figure 8). Installed at Peavine was a datalogger (Campell Scientific, CRX1000 coupled with a HMP45C probe) that measured relative humidity and temperature at the site, and a particulate matter sensor (Purple Air, PA-II) which used a laser particle counter to give some air chemistry data. The deployed instrument data at Peavine was extracted, and the mean and standard deviation for each parameter during the RMAS sampling deployments was calculated. Meteorological and air chemistry data for the Greenhouse sampling site were composed of the same parameters as described for the sampling sites in the first manuscript. Greenhouse ancillary data was downloaded from the internet, and the mean and standard deviation by sampling deployment was calculated for each parameter. Because ancillary data were sparse at Peavine, they were regressed against the same Greenhouse data to determine whether the Greenhouse sampling site ancillary data could be applied to Peavine, this was not the case.

Overall, my contributions to the two manuscripts provided foundational data from which the manuscripts were developed. My contributions required attention to detail to

ensure samples were not contaminated and were analyzed correctly. Because Hg is sensitive to external influences, it can be difficult to carry out successful sampling. Also, effective time management was crucial for the success of the manuscripts. Due to the care and rigor in which I performed duties, the RMAS data will be utilized to benefit the overall understanding of atmospheric reactive mercury.

Chapter 3 Tables and Figures

Meteorological Parameters	Air Chemistry Parameters
Precipitation (mm)	Carbon monoxide (ppm)
Wind direction (degree)	Sulfur dioxide (ppb)
Air temperature (C)	Nitrogen dioxide (ppb)
Relative humidity (%)	Ozone (ppb)
Wind speed (m s^{-1})	Particulate matter < 10 µm and < 2.5 µm (µg m^{-3})
Solar radiation (W m^{-2})	

Table 1. Ancillary data parameters summarized for the Guadalupe Mountains and Great Salt Lake sampling sites.

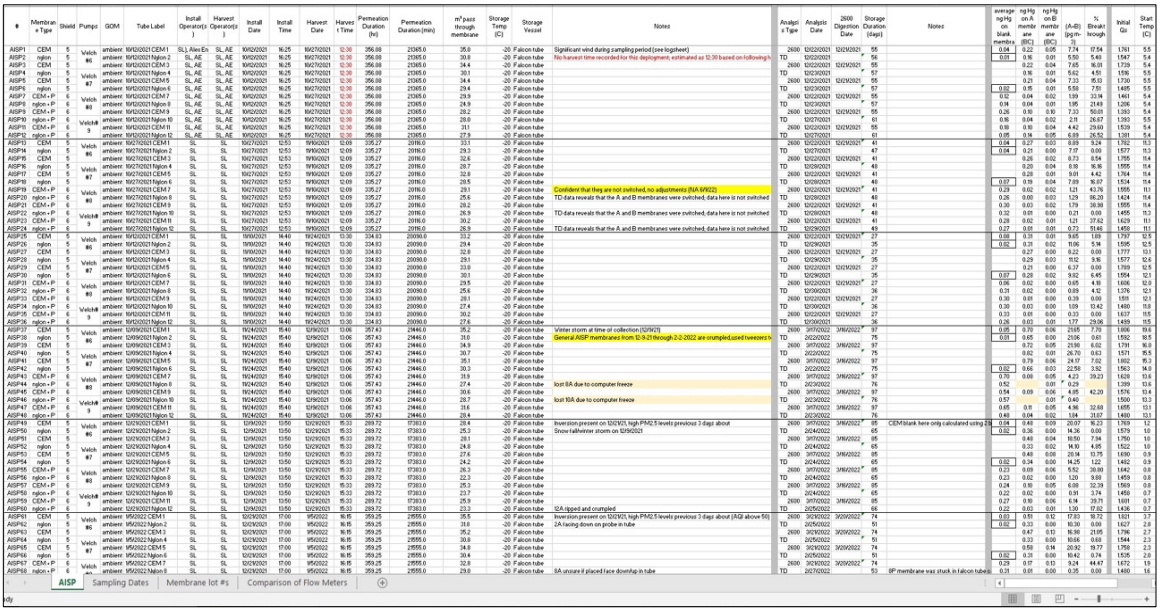

Figure 1. Image of a portion of the inventory spreadsheet used for the Great Salt Lake, UT site. Each membrane sample was a row in the spreadsheet and each column defined information for that individual sample. Column information included: the sample identity; deployment and collection dates and times; sample concentrations; flow rate data; etc.

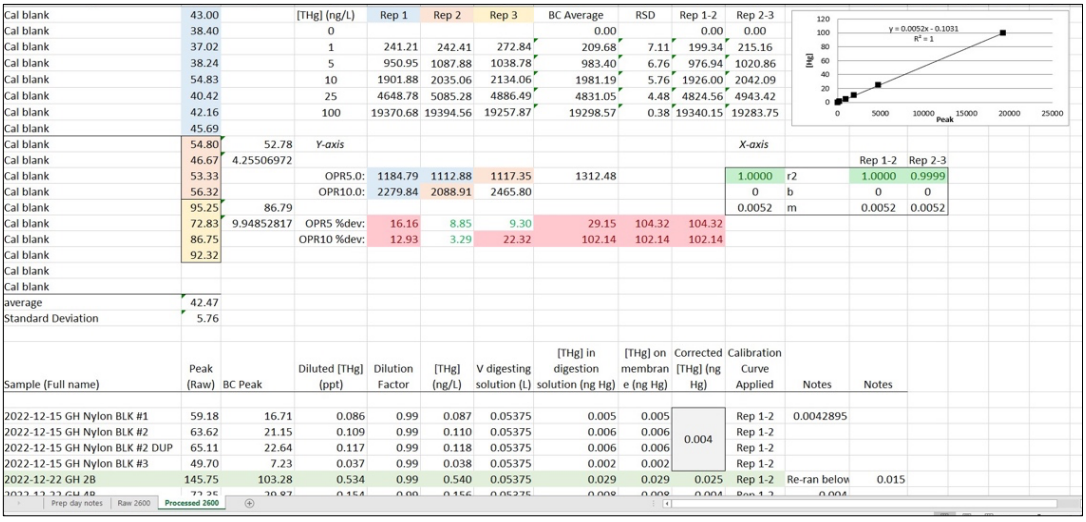

Cal blank	43.00		[THg] (ng/L)	Rep 1	Rep 2	Rep 3	BC Average	RSD	Rep 1-2	Rep 2-3			
Cal blank	38.40		0				0.00		0.00	0.00			
Cal blank	37.02		1	241.21	242.41	272.84	209.68	7.11	199.34	215.16			
Cal blank	38.24		5	950.95	1087.88	1038.78	983.40	6.76	976.94	1020.86			
Cal blank	54.83		10	1901.88	2035.06	2134.06	1981.19	5.76	1926.00	2042.09			
Cal blank	40.42		25	4648.78	5085.28	4886.49	4831.05	4.48	4824.56	4943.42			
Cal blank	42.16		100	19370.68	19394.56	19257.87	19298.57	0.38	19340.15	19283.75			
Cal blank	45.69												
Cal blank	54.80	52.78	*Y-axis*							*X-axis*			
Cal blank	46.67	4.25506972										Rep 1-2	Rep 2-3
Cal blank	53.33		OPR5.0:	1184.79	1112.88	1117.35	1312.48			1.0000	r2	1.0000	0.9999
Cal blank	56.32		OPR10.0:	2279.84	2088.91	2465.80				0	b	0	0
Cal blank	95.25	86.79								0.0052	m	0.0052	0.0052
Cal blank	72.83	9.94852817	OPR5 %dev:	16.16	8.85	9.30	29.15	104.32	104.32				
Cal blank	86.75		OPR10 %dev:	12.93	3.29	22.32	102.14	102.14	102.14				
Cal blank	92.32												
Cal blank													
Cal blank													
average	42.47												
Standard Deviation	5.76												

Sample (Full name)	Peak (Raw)	BC Peak	Diluted [THg] (ppt)	Dilution Factor	[THg] (ng/L)	V digesting solution (L)	[THg] in digestion solution (ng Hg)	[THg] on membran e (ng Hg)	Corrected [THg] (ng Hg)	Calibration Curve Applied	Notes	Notes
2022-12-15 GH Nylon BLK #1	59.18	16.71	0.086	0.99	0.087	0.05375	0.005	0.005	0.004	Rep 1-2	0.0042895	
2022-12-15 GH Nylon BLK #2	63.62	21.15	0.109	0.99	0.110	0.05375	0.006	0.006		Rep 1-2		
2022-12-15 GH Nylon BLK #2 DUP	65.11	22.64	0.117	0.99	0.118	0.05375	0.006	0.006		Rep 1-2		
2022-12-15 GH Nylon BLK #3	49.70	7.23	0.037	0.99	0.038	0.05375	0.002	0.002		Rep 1-2		
2022-12-22 GH 2B	145.75	103.28	0.534	0.99	0.540	0.05375	0.029	0.029	0.025	Rep 1-2	Re-ran below	0.015
2022-12-22 GH 4B	72.25	29.87	0.154	0.99	0.156	0.05375	0.008	0.008	0.004	Rep 1-2	0.004	

Prep day notes | Raw 2600 | Processed 2600

Figure 2. An example of the Excel spreadsheet used to store Tekran 2600 analysis data and used to convert Tekran outputs to concentrations in pg m^{-3}. At the bottom of the spreadsheet, three tabs contained: sample preparation notes; Tekran data outputs; and processed data. Visualized here is the processed data tab which included the calibration blank samples, all standards, and the calculations to convert Tekran outputs to concentrations in pg m^{-3}.

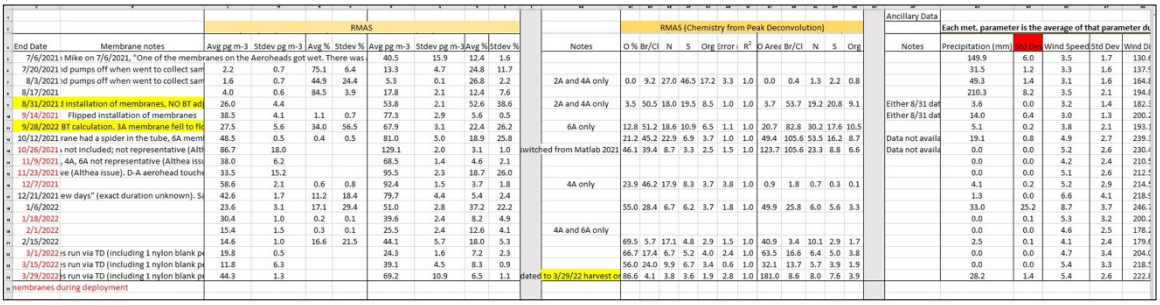

		RMAS								RMAS (Chemistry from Peak Deconvolution)													Ancillary Data					
																								Each met. parameter is the average of that parameter du				
End Date	Membrane notes	Avg pg m-3	Stdev pg m-3	Avg %	Stdev %	Avg pg m-3	Stdev pg m-3	Avg %	Stdev %	Notes	O %	Br/Cl	N	S	Org Error	R^2	O Area	Br/Cl	N	S	Org	Notes	Precipitation (mm)	Std Dev	Wind Speed	Std Dev	Wind Di
7/6/2021	Mike on 7/6/2021, "One of the membranes on the Aeroheads got wet. There was					40.5	15.9	12.4	1.6														149.9	6.0	3.5	1.7	130.6
7/20/2021	d pumps off when went to collect sam	2.2	0.7	75.1	6.4	13.3	4.7	24.8	11.7														31.5	1.2	3.3	1.6	137.5
8/3/2021	d pumps off when went to collect sam	1.6	0.7	44.9	24.4	5.3	0.1	26.8	2.2	2A and 4A only	0.0	9.2	27.0	46.5	17.2	3.3	1.0	0.0	0.4	1.3	2.2	0.8	49.3	1.4	3.1	1.6	164.8
8/17/2021		4.0	0.6	84.5	3.9	17.8	2.1	12.4	7.6														210.3	8.2	3.5	2.1	194.8
8/31/2021	I installation of membranes, NO BT adj	26.0	4.4			53.8	2.1	52.6	38.6	2A and 4A only	3.5	50.5	18.0	19.5	8.5	1.0	1.0	3.7	53.7	19.2	20.8	9.1	Either 8/31 dat	3.6	0.0	3.2	1.4	182.3
9/14/2021	Flipped installation of membranes	38.5	4.1	1.1	0.7	77.3	2.9	5.6	0.5														Either 8/31 dat	14.0	0.4	3.0	1.3	200.2
9/28/2022	BT calculation. 3A membrane fell to flo	27.5	5.6	34.0	56.5	67.9	3.1	22.4	26.2	6A only	12.8	51.2	18.6	10.9	6.5	1.1	1.0	20.7	82.8	30.2	17.6	10.5		5.1	0.2	3.8	2.1	193.1
10/12/2021	rane had a spider in the tube, 6A mem	48.5	0.5	0.4	0.5	81.0	5.0	18.9	25.8		21.2	45.2	22.9	6.9	3.7	1.0	1.0	49.4	105.6	53.5	16.2	8.7	Data not availa	19.1	0.8	4.9	2.7	239.3
10/26/2021	not included; not representative (Alth	86.7	18.0			129.1	2.0	3.1	1.0	witched from Matlab 2021	46.1	39.4	8.7	3.3	2.5	1.5	1.0	123.7	105.6	23.3	8.8	6.6	Data not availa	0.0	0.0	5.2	2.6	230.4
11/9/2021	, 4A, 6A not representative (Althea iss	38.0	6.2			68.5	1.4	4.6	2.1															0.0	0.0	4.2	2.4	210.5
11/23/2021	ve (Althea issue). D-A aerohead touche	33.5	15.2			95.5	2.3	18.7	26.0															0.0	0.0	5.1	2.6	212.5
12/7/2021		58.6	2.1	0.6	0.8	92.4	1.5	3.7	1.8	4A only	23.9	46.2	17.9	8.3	3.7	3.8	1.0	0.9	1.8	0.7	0.3	0.1		4.1	0.2	5.2	2.9	214.5
12/21/2021	ew days" (exact duration unknown). Sa	42.6	1.7	11.2	18.4	79.7	4.4	5.4	2.4															1.3	0.0	6.6	4.1	218.5
1/6/2022		23.6	3.1	17.1	29.4	51.0	2.8	37.2	22.2		55.0	28.4	6.7	6.2	3.7	1.8	1.0	49.9	25.8	6.0	5.6	3.3		33.0	25.2	8.7	3.7	246.7
1/18/2022		30.4	1.0	0.2	0.1	39.6	2.4	8.2	4.9															0.0	0.1	5.3	3.2	200.2
2/1/2022		15.4	1.5	0.3	0.1	25.5	2.4	12.6	4.1	4A and 6A only														0.0	0.0	4.6	2.5	178.2
2/15/2022		14.6	1.0	16.6	21.5	44.1	5.7	18.0	5.3		69.5	5.7	17.1	4.8	2.9	1.5	1.0	40.9	3.4	10.1	2.9	1.7		2.5	0.1	4.1	2.4	179.6
3/1/2022	s run via TD (including 1 nylon blank p	19.8	0.5			24.3	1.6	7.2	2.3		66.7	17.4	6.7	5.2	4.0	2.4	1.0	63.5	16.6	6.4	5.0	3.8		0.0	0.0	4.7	3.4	204.0
3/15/2022	s run via TD (including 1 nylon blank p	11.8	6.3			39.1	4.5	8.3	0.9		56.0	24.0	9.9	6.7	3.4	0.6	1.0	32.1	13.7	5.7	3.9	1.9		0.0	0.0	5.4	3.3	218.5
3/29/2022	s run via TD (including 1 nylon blank p	44.3	1.3			69.2	10.9	6.5	1.1	dated to 3/29/22 harvest o	86.6	4.1	3.8	3.6	1.9	2.8	1.0	181.0	8.6	8.0	7.6	3.9		28.2	1.4	5.4	2.6	222.5
nembranes during deployment																											

Figure 3. Image of a portion of the summary spreadsheet prepared for the Guadalupe Mountains, TX site. Data were compartmentalized using vertical gray columns, here separating: membrane concentrations; membrane chemistry; and meteorological data (left to right).

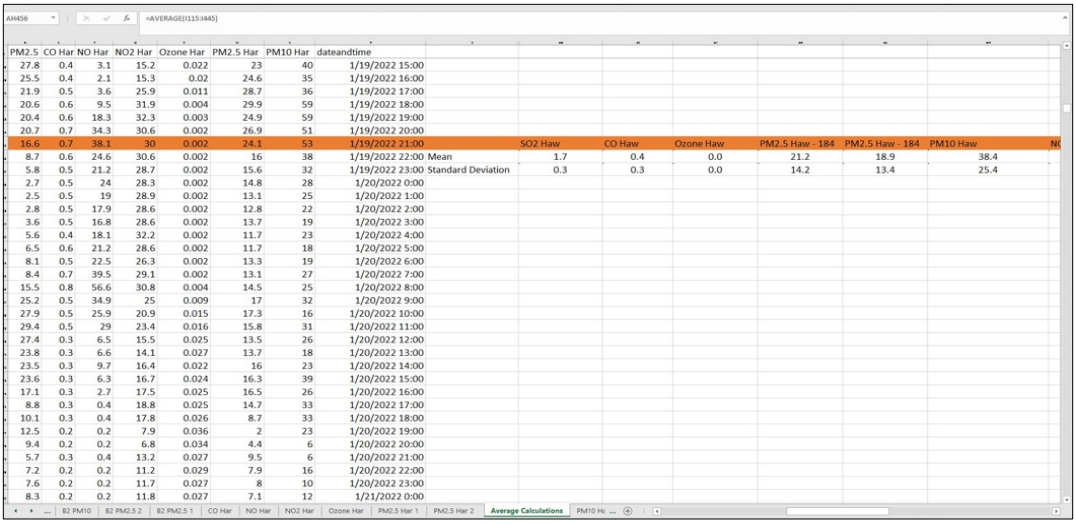

PM2.5	CO Har	NO Har	NO2 Har	Ozone Har	PM2.5 Har	PM10 Har	dateandtime							
27.8	0.4	3.1	15.2	0.022	23	40	1/19/2022 15:00							
25.5	0.4	2.1	15.3	0.02	24.6	35	1/19/2022 16:00							
21.9	0.5	3.6	25.9	0.011	28.7	36	1/19/2022 17:00							
20.6	0.6	9.5	31.9	0.004	29.9	59	1/19/2022 18:00							
20.4	0.6	18.3	32.3	0.003	24.9	59	1/19/2022 19:00							
20.7	0.7	34.3	30.6	0.002	26.9	51	1/19/2022 20:00							
16.6	0.7	38.1	30	0.002	24.1	53	1/19/2022 21:00	SO2 Haw	CO Haw	Ozone Haw	PM2.5 Haw - 184	PM2.5 Haw - 184	PM10 Haw	N
8.7	0.6	24.6	30.6	0.002	16	38	1/19/2022 22:00	Mean	1.7	0.4	0.0	21.2	18.9	38.4
5.8	0.5	21.2	28.7	0.002	15.6	32	1/19/2022 23:00	Standard Deviation	0.3	0.3	0.0	14.2	13.4	25.4
2.7	0.5	24	28.3	0.002	14.8	28	1/20/2022 0:00							
2.5	0.5	19	28.9	0.002	13.1	25	1/20/2022 1:00							
2.8	0.5	17.9	28.6	0.002	12.8	22	1/20/2022 2:00							
3.6	0.5	16.8	28.6	0.002	13.7	19	1/20/2022 3:00							
5.6	0.4	18.1	32.2	0.002	11.7	23	1/20/2022 4:00							
6.5	0.6	21.2	28.6	0.002	11.7	18	1/20/2022 5:00							
8.1	0.5	22.5	26.3	0.002	13.3	19	1/20/2022 6:00							
8.4	0.7	39.5	29.1	0.002	13.1	27	1/20/2022 7:00							
15.5	0.8	56.6	30.8	0.004	14.5	25	1/20/2022 8:00							
25.2	0.5	34.9	25	0.009	17	32	1/20/2022 9:00							
27.9	0.5	25.9	20.9	0.015	17.3	16	1/20/2022 10:00							
29.4	0.5	29	23.4	0.016	15.8	31	1/20/2022 11:00							
27.4	0.3	6.5	15.5	0.025	13.5	26	1/20/2022 12:00							
23.8	0.3	6.6	14.1	0.027	13.7	18	1/20/2022 13:00							
23.5	0.3	9.7	16.4	0.022	16	23	1/20/2022 14:00							
23.6	0.3	6.3	16.7	0.024	16.3	39	1/20/2022 15:00							
17.1	0.3	2.7	17.5	0.025	16.5	26	1/20/2022 16:00							
8.8	0.3	0.4	18.8	0.025	14.7	33	1/20/2022 17:00							
10.1	0.3	0.4	17.8	0.026	8.7	33	1/20/2022 18:00							
12.5	0.2	0.2	7.9	0.036	2	23	1/20/2022 19:00							
9.4	0.2	0.2	6.8	0.034	4.4	6	1/20/2022 20:00							
5.7	0.3	0.4	13.2	0.027	9.5	6	1/20/2022 21:00							
7.2	0.2	0.2	11.2	0.029	7.9	16	1/20/2022 22:00							
7.6	0.2	0.2	11.7	0.027	8	10	1/20/2022 23:00							
8.3	0.2	0.2	11.8	0.027	7.1	12	1/21/2022 0:00							

Figure 4. Example of how the mean and standard deviation were calculated in a spreadsheet for each ancillary data parameter. Separate spreadsheets were used for each sampling site. One tab in the spreadsheet would contain sorted parameter data and was where mean calculations were performed.

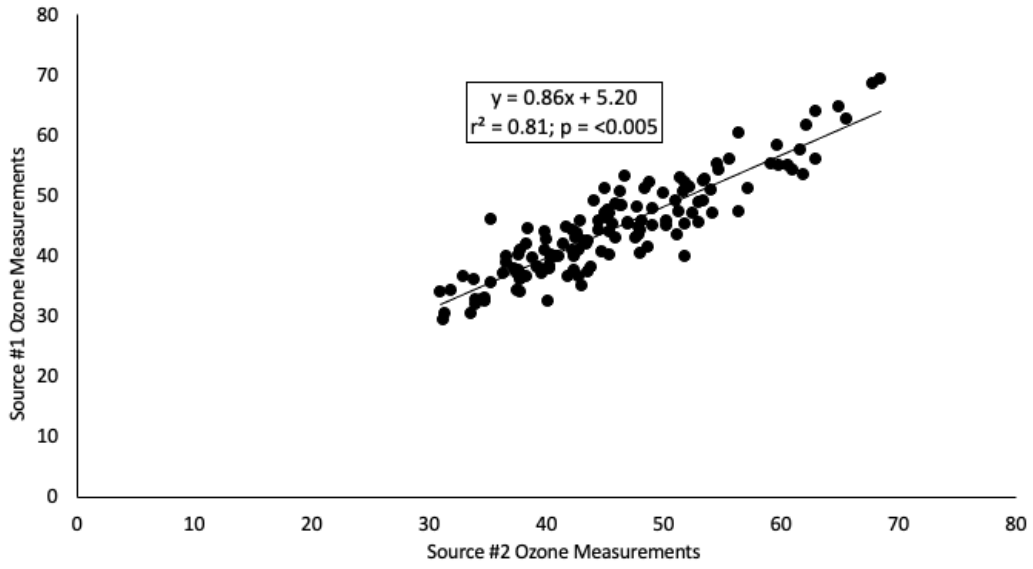

Figure 5. A regression plot of ozone measurements over a period in 2022 measured by two different sources near the Guadalupe Mountains, TX site. In this case, ozone measurements were deemed interchangeable because of the significant slope value close to unity.

Figure 6. A general RMAS sample collection. On the left, the RMAS flow rate was being checked (at Peavine) before membrane cartridges were removed from the RMAS shield and brought inside for membrane collection. On the right was the collection process for membranes from the cartridges (at the Greenhouse). The green wrench shown was used to loosen each membrane cartridge and tweezers were used to place each membrane sample into its own conical tube, shown behind the membrane cartridges.

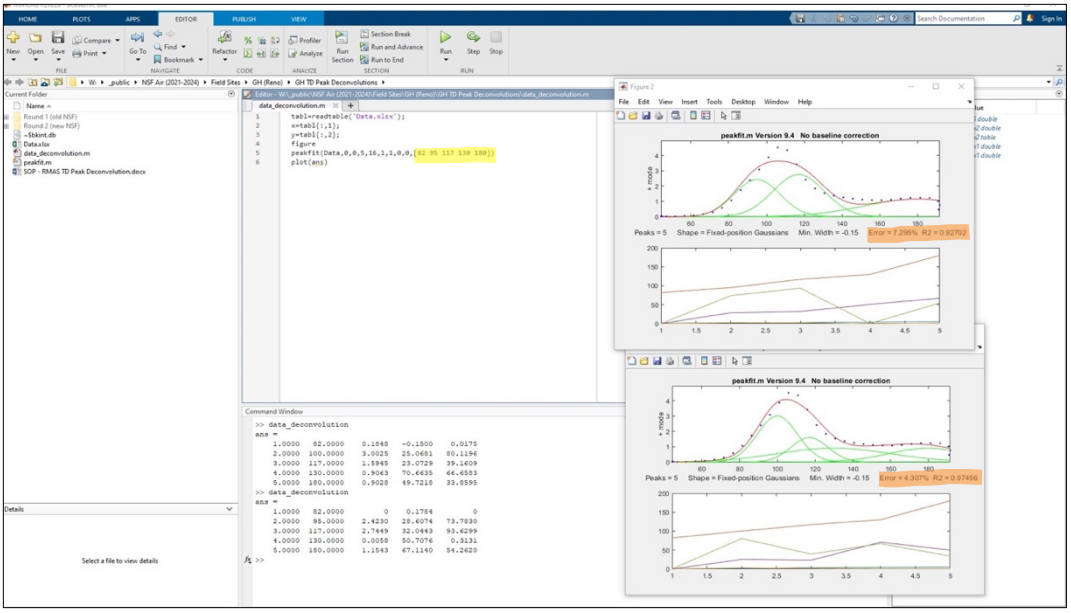

Figure 7. The deconvolution procedure in MATLAB (R2022a). The center of the image shows the code for the deconvolution method in which I changed the desorption values (highlighted in yellow) to obtain different model outputs. Then, model outputs, shown on the right, were compared until the lowest model error and highest r^2 value were achieved (highlighted in orange).

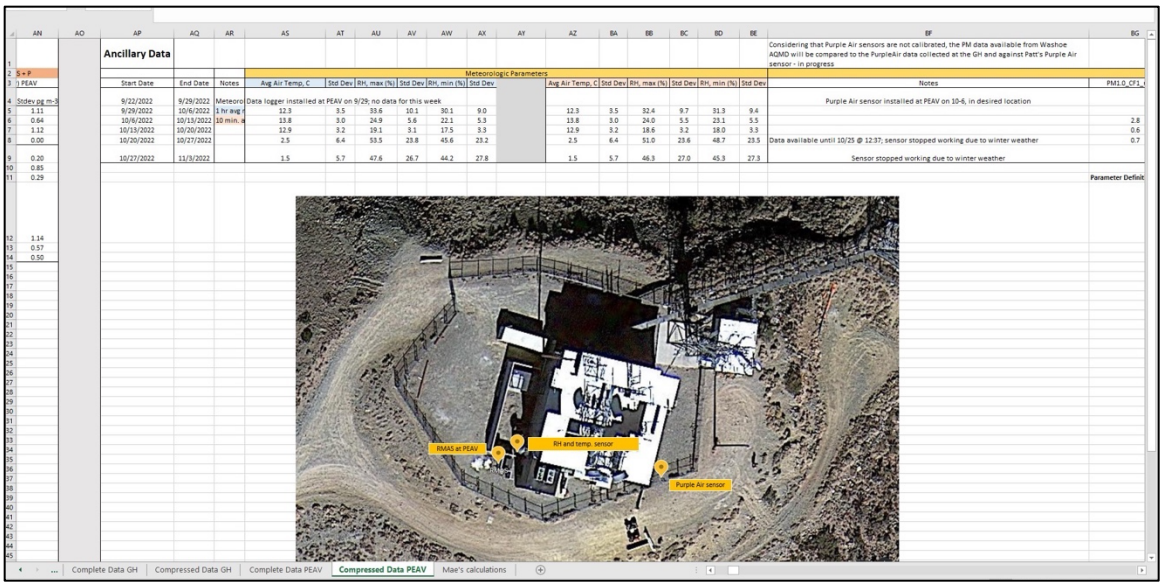

Figure 8. The Greenhouse and Peavine sampling site summary spreadsheet used for the second manuscript. Specifically, this capture of the spreadsheet displays the Peavine compiled ancillary data, and a picture mapping ancillary data instruments in proximity to the Reactive Mercury Active System at Peavine.

Chapter 3 References

Annamaa, A. (2015). Introducing Thonny, a Python IDE for learning programming. Proceedings of the 15th Koli Calling Conference on Computing Education Research, 117–121. https://doi.org/10.1145/2828959.2828969

Environmental Protection Agency (EPA) (2002). Method 1631, revision E: Mercury in water by oxidation, purge and trap, and cold vapor atomic fluorescence spectrometry.

Dunham-Cheatham, S. M., Lyman, S., & Gustin, M. S. (2023). Comparison and calibration of methods for ambient reactive mercury quantification. Science of The Total Environment, 856, 159219. https://doi.org/10.1016/j.scitotenv.2022.159219

MATLAB. (2022). version 2022a. Natick, Massachusetts: The MathWorks Inc.

Microsoft Corporation. (2016). Microsoft Excel. Retrieved from https://office.microsoft.com/excel

Chapter 4: Conclusions and Recommendations for Future Work

For this thesis, experiments were performed with the goal of improving the University of Nevada, Reno – Reactive Mercury Active System (RMAS) ability to measure atmospheric reactive mercury (RM) accurately, and these were discussed in Chapter 2. Chapter 2 consists of a manuscript that will be submitted to a peer-reviewed journal, with additional contributions coming from others in the Gustin lab. Chapter 3 of this thesis presented the contributions that I made to two manuscripts discussing the sources and RMAS measurements of RM at various sampling locations. Both manuscripts in Chapter 3 are in preparation. Altogether, this thesis provided necessary knowledge to improve atmospheric RM measurements and data that will aid in developing a better understanding of the atmospheric behavior of mercury (Hg). Applications of this work include the potential for the standardization of RMAS measurements. Additionally, RMAS data may be used for policy and mercury modeling (e.g., Minamata Convention)

Hg in the air is challenging to measure because concentrations are in the parts per trillion, meaning that great steps need to be taken to avoid contamination. The RMAS was developed with the recognition that measurements associated with the gold standard Tekran instrument are biased low and suffer from artifacts. However, the RMAS also has limitations including a long sampling time, membrane limitations, and previous measurements of atmospheric RM taken by a co-located dual-channel system (DCS) were 50% higher than the RMAS (Dunham-Cheatham et al., 2023). The experiments discussed in Chapter 2 focused on testing: whether increasing the RMAS flow rate to

improve sampling resolution impacted measurements of concentrations and chemistry; whether similar commercially available membranes would work as alternative collection surfaces; and potential causes for measurement discrepancies observed between the RMAS and dual-channel systems.

RMAS experiments showed that increasing the flow rate decreased RM retention on CEM and nylon membranes, which was more profound during the winter. Increasing the flow rate did not impact the chemistry measured by nylon membranes. Further testing is required before the RMAS flow rate can be confidently increased. The greatest limitation to accurate RM measurements is the lack of demonstrated field calibration(s). The calibration of RM measurements is one of the main research foci of the Gustin Lab Group at the University of Nevada, Reno. The Gustin Lab Group, in collaboration with Dr. Seth Lyman at Utah State University, have been performing calibrations of RMAS membranes utilizing a custom-built calibrator supplied by Dr. Lyman. Preliminary results show membranes lose RM during ambient sampling. Future work using the calibrator should include calibration of RM measurements at varying flow rates, in the laboratory and field.

Out of eight membranes tested, all alternate membranes collected less RM than the historical RMAS membranes and all nylon membranes tested collected Hg compounds differently. Therefore, the same or a similar composition of commercial membrane material cannot be expected to measure or identify RM compounds the same. Despite being the best performing during the membrane intercomparisons, historical RMAS membranes exhibit sampling artifacts and may be inaccessible to collaborators due to their cost, long time to manufacture, and/or collaborator location. The exploration

and identification of new collection materials for RM measurements of concentrations and chemistry must occur, and is another research focus of the Gustin Lab.

Lastly, Chapter 2 addressed RMAS measurement discrepancies relative to the dual-channel system, which cannot be explained due to the sorption of RM to the RMAS membrane cartridge. Further research is necessary to determine how RM is being lost during RMAS sampling. Potential RM loss mechanisms may include the long sampling time of the RMAS and/or RM transformations occurring on membranes. The calibration of RMAS measurements will give a clear answer to whether the RMAS measures concentrations of atmospheric RM accurately.

In Chapter 3 of this thesis, the contributions I made to a global, multi-year RMAS sampling campaign that resulted in two manuscripts are presented. For both manuscripts, I was the primary data manager. I collected, analyzed, and compiled the majority of RMAS and ancillary data for six sampling sites. The data that I provided for the manuscripts will be used to better understand the behavior and sources of atmospheric RM because the sites provided measurements of RM under various sampling conditions and between two elevations. In addition, by demonstrating the applicability of the RMAS instrument at multiple sampling locations, the two manuscripts serve as demonstrations to the Hg community that the RMAS can easily be deployed, and act as a potential standard instrument for RM measurements.

Although the work of this thesis will improve current RM measurements and increase the understanding of the behavior and sources of RM in the environment, obtaining accurate RM measurements is a work in progress. Future work of the Hg research community should focus on the calibration of atmospheric RM measurements,

the direct identification of atmospheric RM compounds, and providing researchers and monitoring networks with a viable technique for accurate measurements of RM concentrations and chemistry. It will be the work and collaboration of many Hg professionals to achieve these goals.

Chapter 4 References

Dunham-Cheatham, S. M., Lyman, S., & Gustin, M. S. (2023). Comparison and calibration of methods for ambient reactive mercury quantification. Science of The Total Environment, 856, 159219. https://doi.org/10.1016/j.scitotenv.2022.159219